8-2008

Effects of High Temperature Cyclic Aging on a Fully-Formulated Lean NO_x Trap Catalyst

Nathan Andrew Ottinger
University of Tennessee, Knoxville

To the Graduate Council:

I am submitting herewith a thesis written by Nathan Andrew Ottinger entitled "Effects of High Temperature Cyclic Aging on a Fully-Formulated Lean NO_X Trap Catalyst." I have examined the final electronic copy of this thesis for form and content and recommend that it be accepted in partial fulfillment of the requirements for the degree of Master of Science, with a major in Mechanical Engineering.

Ke Nguyen, Major Professor

We have read this thesis and recommend its acceptance:

Bruce G. Bunting, Todd J. Toops, J. Roger Parsons

Accepted for the Council:
Carolyn R. Hodges

Vice Provost and Dean of the Graduate School

(Original signatures are on file with official student records.)

To the Graduate Council:

I am submitting herewith a thesis written by Nathan Andrew Ottinger entitled "Effects of High Temperature Cyclic Aging on a Fully-Formulated Lean NO_x Trap Catalyst." I have examined the final electronic copy of this thesis for form and content and recommend that it be accepted in partial fulfillment of the requirements for the degree of Master of Science, with a major in Mechanical Engineering.

Ke Nguyen, Major Professor

We have read this thesis
and recommend its acceptance:

Bruce G. Bunting

Todd J. Toops

J. Roger Parsons

Accepted for the Council:

Carolyn R. Hodges,
Vice Provost and Dean of the Graduate School

(Original signatures are on file with official student records.)

EFFECTS OF HIGH TEMPERATURE CYCLIC AGING ON A FULLY-FORMULATED LEAN NO_X TRAP CATALYST

A

Thesis

Presented for the

Master of Science Degree

The University of Tennessee, Knoxville

Nathan Andrew Ottinger

August 2008

ACKNOWLEDGEMENTS

I would like to thank my advisor, Dr. Ke Nguyen, and also my co-advisors, Dr. Bruce Bunting and Dr. Todd Toops, for their technical guidance, support, and encouragement throughout the course of this project. I would also like to thank my graduate committee member Dr. J. Roger Parsons for his valued feedback. Furthermore, Andrew Payzant, Jane Howe, and Roberta Meisner of the Oak Ridge National Laboratory and Allan Patchen and Dr. John Dunlap of the University of Tennessee have given me a lot of invaluable advice and I would like to express my gratitude for their assistance. And, for their friendship and support I would like to thank my colleagues Adam Foster, Adam Youngquist, Vitaly Prikhodko, and Scott Eaton.

Finally I would like to thank Delphi/Umicore for supplying the catalysts analyzed in this project and the Department of Energy Vehicle Technologies Fuel Technology Program for funding.

ABSTRACT

The thermal deactivation mechanisms of a lean NO_x trap (LNT) are analyzed in this study. Accelerated lean/rich aging experiments are performed with a bench-flow reactor, and high temperature exotherms are achieved with pulses of reductants. Reduction in steady state NO_x conversion as a result of aging is evaluated at a range of temperatures using the same bench-flow reactor. The results of these evaluations are used to show that NO_x conversion in this study is a function of evaluating temperature, aging temperature, and number of aging cycles.

Surface characterization studies are used to determine changes in washcoat morphology. Electron probe microanalysis line scans and elemental maps show that migration or agglomeration of washcoat components (excluding PGM) does not occur. Substantial PGM growth as a result of aging is seen using scanning transmission electron microscopy/scanning electron microscopy/energy dispersive spectroscopy (STEM/SEM/EDS) and powder X-ray diffraction (P-XRD), but this growth, at least initially, has little effect on NO_x conversion. P-XRD is also used to study phase transitions of Ba and Al_2O_3. All $BaCO_3$ peaks quickly disappear after aging, and there is no subsequent growth of any $BaAl_2O_4$ peaks. The disappearance of crystalline $BaCO_3$ does not appear to have a large effect on NO_x storage or conversion. The Al_2O_3 peaks are stable, but large surface area reductions are measured with Brunauer, Emmett, and Teller (BET) surface area measurements. Both reductions in surface area and PGM particle size growth are shown to correlate well with reductions in NO_x conversion.

TABLE OF CONTENTS

LIST OF TABLES

LIST OF FIGURES

Chapter 1

INTRODUCTION

The purpose of this section is to provide an overview of the current state of diesel technology and to introduce the present study. The importance of diesel engines and the role they play in the American economy is first presented in Section 1.1. Diesel emissions and their impact on the environment are then discussed in Section 1.2. Current emissions regulations and the effect of these regulations on diesel engines is covered in Section 1.3, and the objectives of the current study are presented in Section 1.4.

1.1 – Importance of Diesel Engines

Diesel engines are the workhorses of the American economy. They are attractive for their energy efficiency, durability, reliability, and low fuel flammability. A study conducted by the Charles River Associates, a global consulting firm that offers economic, financial, and business management expertise, estimates that diesel engines typically use 25 to 35 percent less fuel in performing a given task than spark ignition (SI) engines [1], and recent introductions of computer monitored common rail direct fuel injection and new combustion chamber designs are pushing the limits of diesel engines even further. Upcoming advances in diesels have the potential to increase their efficiency to about 55 percent [2].

Many of America's industries are desperate for higher efficiency diesel engines as oil prices continue to climb above the $140/barrel mark, and as the average price of diesel

continues to far outstrip that of gasoline. The majority of these industries are heavy transportation industries in which high torque at low rpm's—another one of diesel's strong points—is desired, such as in containerships and locomotives. Figure 1.1.1 clearly illustrates America's reliance on diesel engines [1]. The table lists the amount of gasoline, diesel fuel, LPG, jet fuel, natural gas, and electricity used in selected sectors. The final column of the table then indicates diesel's share of each sector. One hundred percent of intercity buses, freight (Class 1) trains, and water freight carriers use diesel engines. Also, diesel fuel supplies power for 83% of the construction sector, 66% of the agricultural industry, and 22% of the mining industry. Obviously, diesel engines are a crucial part of America's economy.

1.2 – Diesel Emissions

Though efficient and durable, diesel engines are not problem-free. Combustion of diesel, through many multi-step reactions, results in the formation of the following pollutants: hydrocarbons (HC), carbon monoxide (CO), carbon dioxide (CO_2), nitrogen oxides (NO_x), particulate matter (PM), and sulfur dioxide (SO_2), which are described in detail in the following paragraphs.

Carbon monoxide is a product of incomplete combustion, with automobile exhaust contributing approximately 56% of all CO emissions nationwide, of which 4.5% was contributed by diesel powered automobiles in 2000. CO at low concentrations can affect people with heart disease by causing chest pain, and at higher concentrations, CO

TRANSPORTATION EXCLUDING GOVERNMENT (trillion Btu)

	Gasoline [a]	Diesel fuel [b]	LPG	Jet fuel	Natural gas	Electricity	Diesel Share
HIGHWAY TRANSPORTATION	**15228**	**3950**	**28**	**0**	**4**	**1**	**21%**
Automobiles	8617	126			0		1%
Motorcycles	25	0					0%
Buses	32	147	1		3	1	80%
Transit	5	78	1		3	1	89%
Intercity[c]		24					100%
School[c]	27	45					62%
Trucks	6554	3677	27		1		36%
Light trucks[d]	5949	226	13		1		4%
Other trucks	605	3451	14		0		85%
NON-HIGHWAY TRANSPORTATION	**335**	**1527**	**0**	**2290**	**775**	**273**	**29%**
Air	35			2290			0%
General aviation	35			86			0%
Domestic air carriers				1857			0%
International air carriers[e]				346			0%
Water	300	1009					77%
Freight		1009					100%
Recreational	300						0%
Pipeline					775	212	0%
Rail		518				61	89%
Freight (Class I)		500					100%
Passenger		18				61	23%
Transit						43	0%
Commuter		9				15	37%
Intercity[c]		9				3	74%
TOTAL	**15563**	**5477**	**28**	**2290**	**779**	**274**	**22%**

FEDERAL GOVERNMENT LAND NONCOMBAT VEHICLES (million gallon-equivalent)

	Gasoline [a]	Diesel fuel [b]	LPG	Natural gas	Electricity	Meth/Eth	Diesel Share
Civilian Agencies	129	12	0	1	0	0	8%
Military Agencies	51	27	0	1	0	0	34%
US Postal Service	100	27	0	3	0	0	21%
Total	**280**	**65**	**0**	**4**	**0**	**0**	**19%**

ENERGY USED IN SELECTED SECTORS (trillion Btu)

	Gasoline [a]	Diesel fuel [b]	LPG	Natural gas	Electricity	Coal	Diesel Share
Construction	38	179	n.a.	n.a.	n.a.	n.a.	83%
Agriculture	173	485	78	n.a.	n.a.	n.a.	66%
Mining	34	196	0	340	263	41	22%
Production of oil and gas	*26*	*68*	*0*	*239*	*117*	*0*	*15%*
Coal mining	*4*	*55*	*0*	*0*	*39*	*0*	*56%*
Mining of metallic ores	*2*	*47*	*0*	*38*	*68*	*0*	*30%*
Other mining	*2*	*26*	*0*	*62*	*37*	*41*	*15%*

Sources: *Transportation excluding government* -- Transportation Energy Data Book, Edition 19, Table 2.3.
Federal government land noncombat vehicles -- Federal Fleet Report, 1997, Table 6.
Construction -- Transportation Energy Data Book, Edition 19; data are for 1985.
Agriculture -- USDA AREI/Production Inputs, Energy, 1994, fuels purchased for on-farm use; converted to BTUs by CRA, data are for 1994
Mining -- 1997 Economic Census, converted to btus by CRA; excludes coal, crude petroleum and natural gas produced and used in the same plant as fuel

Notes: n.a. = not available
[a] Includes ethanol and methanol blends
[b] Includes residual fuel oil; for federal fleet, also includes biodiesel
[c] Estimated from travel data
[d] Two axle, four wheel trucks
[e] One-half of fuel used by domestic carriers in international operations

Figure 1.1.1 – Diesel's share of America's energy consumption broken down by sector [1]

can lead to vision problems as well as reduced ability to work or learn. CO also contributes to the formation of smog [3].

Carbon dioxide is a product of the combustion reaction between hydrocarbons and air. In 2004 approximately 20% of the CO_2 released from mobile sources came from diesel engines, whereas approximately 66% came from SI engines. CO_2 is considered a greenhouse gas and is thought to be the largest contributor to global warming. The Intergovernmental Panel on Climate Change *Fourth Assessment Report* states that the global surface temperature has risen 0.56 to 0.92^{o}C over the past 100 years and that sea levels have risen an average of 3.1 mm/yr since 1993 as a result of global warming [4]. Figures 1.2.1 and 1.2.2 illustrate this rise in surface temperature and sea level as well as indicate the possible role of CO_2 in global warming.

Nitrogen oxides are formed when nitrogen is oxidized at high temperature, as in the combustion chamber. Sources of NO_x include motor vehicles, thermal power plants, and other sources that burn fuel, with 49% of NO_x coming from motor vehicles. Nitrous oxide, N_2O, a member of the NO_x family, accumulates in the atmosphere and contributes to global warming. NO_x release also leads to acid rain and increased nitrogen loading in water bodies which upsets the chemical balance of nutrients necessary for aquatic life. Furthermore, NO_x contributes to the formation of ground-level ozone (O_3) which can cause adverse effects in children, elderly people, and people with respiratory problems such as lung disease and asthma by damaging lung tissue and reducing lung function [5].

Sulfur dioxide, SO_2, forms when sulfur in diesel fuel is oxidized during high temperature combustion. SO_2, like NO_x, leads to the formation of acid rain which acidifies aqueous bodies, making them unsuitable for aquatic life. SO_2 also reacts with

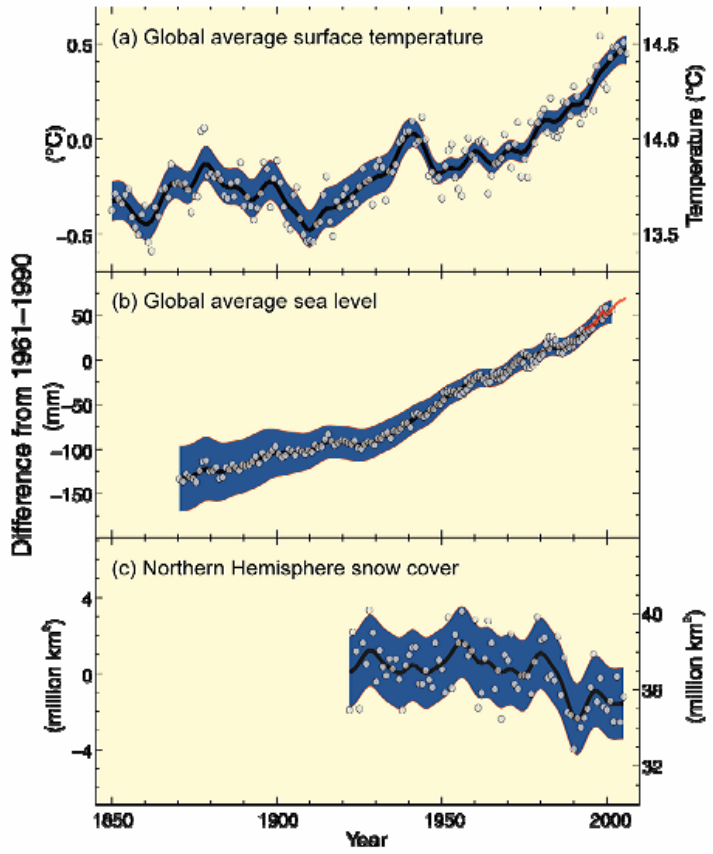

Figure 1.2.1 – Global average increase in surface temperature and sea level [4]

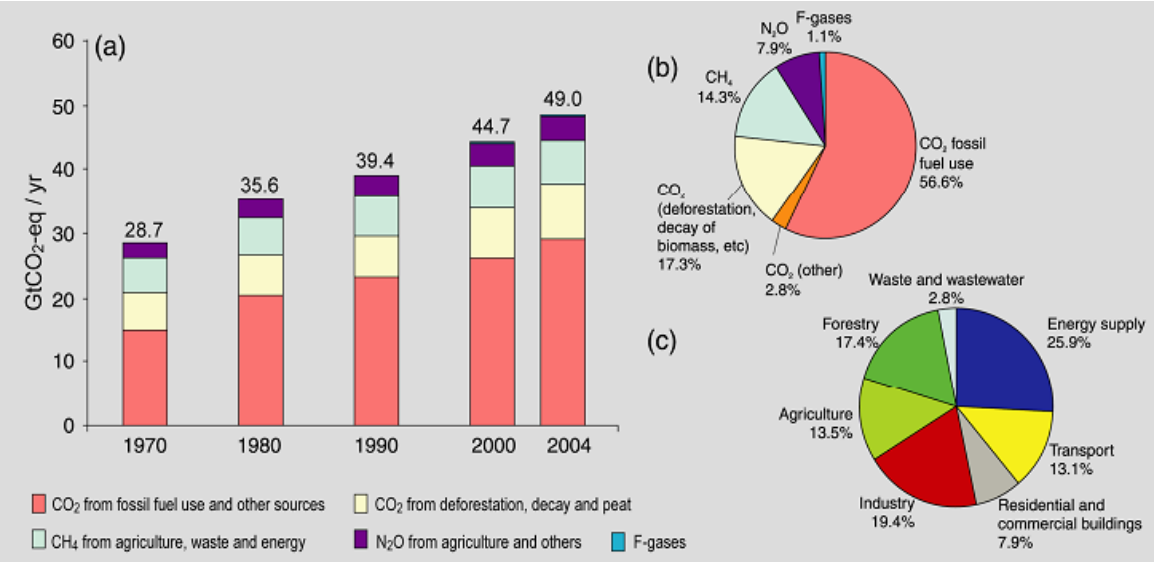

Figure 1.2.2 – Sources and relative amounts of common greenhouse gases. CO_2 produced as a result of fossil fuel use accounts for >50% of greenhouse gas [4]

other chemicals in the air and forms sulfate particles which can gather in the lungs and increase a person's susceptibility to respiratory diseases. SO_2 particles are also responsible for reduced visibility in many parts of the U.S. [6].

Particulate matter (PM) is released as a result of diesel combustion and is composed mainly of carbon and absorbed hydrocarbons. Long term exposure to PM has been associated with the development of chronic bronchitis, while short term exposure to PM has been shown to aggravate lung disease and increase susceptibility to respiratory infections. Inhalation of "fine particles" less than 2.5 μm in diameter, $PM_{2.5}$, can lead to decreased lung function, while inhaling "coarse particles" with diameters between 2.5 and 10 μm, PM_{10}, aggravates respiratory conditions such as asthma. PM is also the major cause of reduced visibility in many parts of the country. [2, 7].

1.3 – Emissions regulations and their Effect on Diesel

As a result of the 1970 Clean Air Act, which set maximum allowable levels of HC, NO_x, SO_x, PM, and CO emissions, automobile manufacturers began installing catalytic converters in cars [5-8]. In the 1980's three-way catalysts (TWC), which simultaneously reduce NO_x, HC, and CO through the following global reactions given in Equations 1.1 to 1.3, were introduced in order to comply with even stricter regulations.

$$2NO_x \rightarrow xO_2 + N_2 \qquad (1.1)$$

$$2CO + O_2 \rightarrow 2CO_2 \qquad (1.2)$$

$$2C_xH_y + (2x+y/2)O_2 \rightarrow 2xCO_2 + yH_2O \qquad (1.3)$$

TWCs are designed for engines operating at a stoichiometric fuel/air ratio, and are not effective in lean-burn engines such as diesel engines because the high concentration

of O_2 in lean exhaust gases shifts the equilibrium position of Equation 1.1 to the left, inhibiting the reduction of NO_x. Lean NO_x Traps (LNTs) are one possible solution to this problem. Because of their ability to operate over a large range of exhaust temperatures and their relatively high NO_x conversion potential (>90%), LNTs have been receiving a lot of attention as a possible aftertreatment solution for lean-burn gasoline and diesel engines. Typically, LNT catalysts are formulated with a NO_x storage component and one or more of the platinum group metals dispersed over a high surface-area γ-Al_2O_3 (alumina) washcoat. The NO_x storage components are usually alkali metal oxides or alkaline earth metal oxides such as barium and/or potassium oxides.

The operation of a LNT is cyclic, consisting of a long lean phase followed by a short rich phase. During the lean phase, NO in the exhaust gas stream is oxidized to NO_2 on platinum group metal (PGM) sites such as Pt, Pd, or Rh and temporarily stored on barium oxide sites in the form of barium nitrites ($Ba(NO_2)_2$) or nitrates ($Ba(NO_3)_2$) [9]. In this manner, the NO_x gradually occupies the available storage sites, and the LNT has to be periodically regenerated by subjecting it to brief, fuel-rich phases. The frequency of these rich phases depends on the size of the LNT, the LNT formulation, the concentration of the NO_x in the exhaust stream, and the exhaust temperature just to name a few. During the rich phase the nitrites and/or nitrates are decomposed, and the stored NO_x is released in the form of NO_2 and reduced to N_2 by CO, H_2 and HC over the PGM sites [9]. The NO_x adsorption in the lean phase and the NO_x desorption and reduction in the rich phase are schematically depicted in Figure 1.3.1.

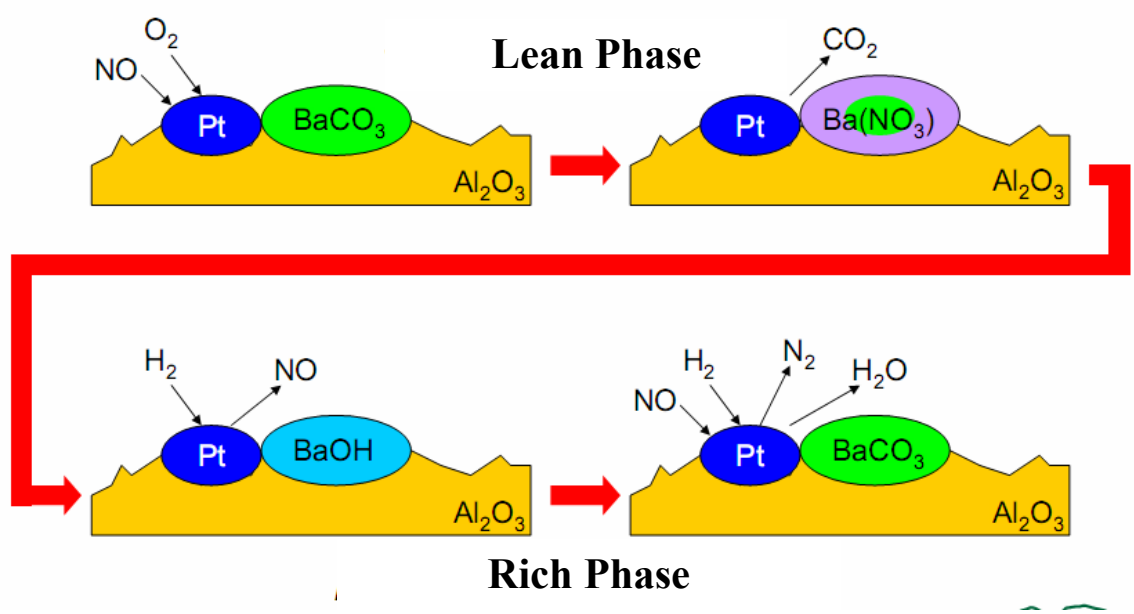

Figure 1.3.1 – Typical lean/rich operation of a LNT catalyst [10]

1.4 – Objectives of the Present Study

The present study is part of a continuing effort by the University of Tennessee, Knoxville and the Fuels Engines and Emissions Research Center (FEERC) to characterize the thermal deactivation of lean NO_x traps (LNTs) by performing engine and accelerated bench-flow aging experiments. Previous engine and bench-flow work performed on model Pt+Rh/Ba/γ-Al_2O_3 and model "Ba+K" LNTs, respectively, has identified PGM sintering, $BaAl_2O_4$ formation, the migration of potassium, the agglomeration of Ba, and surface area loss as thermal deactivation mechanisms (The results of these studies will be expounded upon in Chapter 2).

In the present study accelerated bench-flow aging experiments similar to those previously performed on the model "Ba+K" LNT are used to determine the effect of

thermal aging on the NO_x conversion and surface morphology of a fully-formulated LNT. Unlike in the previous accelerated aging study, the LNT used in this study does not contain K, and is furthermore loaded with a number of performance enhancing additives (See Section 3.2.1 for full formulation). Aging and evaluation experiments similar to those previously done are performed in a bench-flow reactor (BFR) using lean/rich cycling of simulated diesel exhaust gases. Target aging temperatures of 700, 800, 900, and 1000^oC are achieved during rich cycles by addition of H_2, CO and O_2 resulting in an 85s exotherm. LNTs are aged using long cycles, consisting of a 130s lean phase and a 50s rich phase, at temperatures of 700 and 800^oC for 5, 25, 50, 100, 150, 200 cycles; at 900^oC for 5, 25, 50, 100, 150, 200, and 300 cycles; and at 1000^oC for 5, 25, 50, 100, 150, 200, and 350 cycles. After each aging experiment, the effect of aging on the LNTs NO_x conversion is evaluated using short cycles, consisting of a 60 s lean phase and 5 s rich phase, at temperatures of 200, 300, and 400^oC. All NO_x conversion evaluations are carried out in the presence of 300 ppm NO, 5% H_2O, 5% CO_2, and a N_2 balance at a gas hourly space velocity (GHSV) of 30,000 h^{-1}.

Surface characterization studies are performed on fresh and aged LNTs in order to elucidate the deactivation mechanisms specific to this fully-formulated LNT. Scanning transmission electron microscopy/scanning electron microscopy/energy dispersive spectroscopy (STEM/SEM/EDS), powder X-ray diffraction (XRD), electron probe microanalysis (EPMA), and Brunauer, Emmett, and Teller (BET) surface area analysis are all used in the present study. Powder XRD is used to determine average Pt particle size growth and to ascertain the formation of new compounds and phase transitions, while TEM is also used to obtain individual Pt particle sizes and particle size

distributions, from which average Pt particle size are be calculated and compared with that obtained from XRD. Particle migration and agglomeration are analyzed with EPMA and surface area measurements of fresh and aged LNTs are carried out with BET.

Chapter 2

LITERATURE REVIEW

The literature review provides background information on the operation and deactivation mechanisms of lean NO_x traps (LNTs). An overview of LNT operation is first presented in Section 2.1, and the operating principles of LNTs are examined more closely in Sections 2.2, 2.3, and 2.4. Section 2.5 explores the thermal deactivation mechanisms of LNTs.

2.1 –Theory of LNT Operation

Lean NO_x Trap (LNT) operation is cyclic, consisting of a series of lean and rich cycles. NO, after being oxidized to NO_2 by platinum group metals (PGM), is stored on the NO_x storage media during the lean phase. As the NO_x trapping capacity of the catalyst is approached, increasingly larger amounts of NO_x begin to slip through the catalyst. At this point, a brief rich phase is initiated during which adsorbed NO_x is released from the catalyst and subsequently reduced to N_2 by reductants such as hydrocarbons (HC), H_2, and CO. The rich phase is followed by another lean phase and the lean/rich sequence continues. The four processes just briefly described—NO oxidation, NO_x storage, NO_x release, and NO_x reduction—are the overall steps of LNT operation and are described in further detail in the next four sections. Figure 2.1.1 shows a complete LNT cycle with a long, lean NO oxidation/NO_x trapping phase followed by a brief, rich NO_x

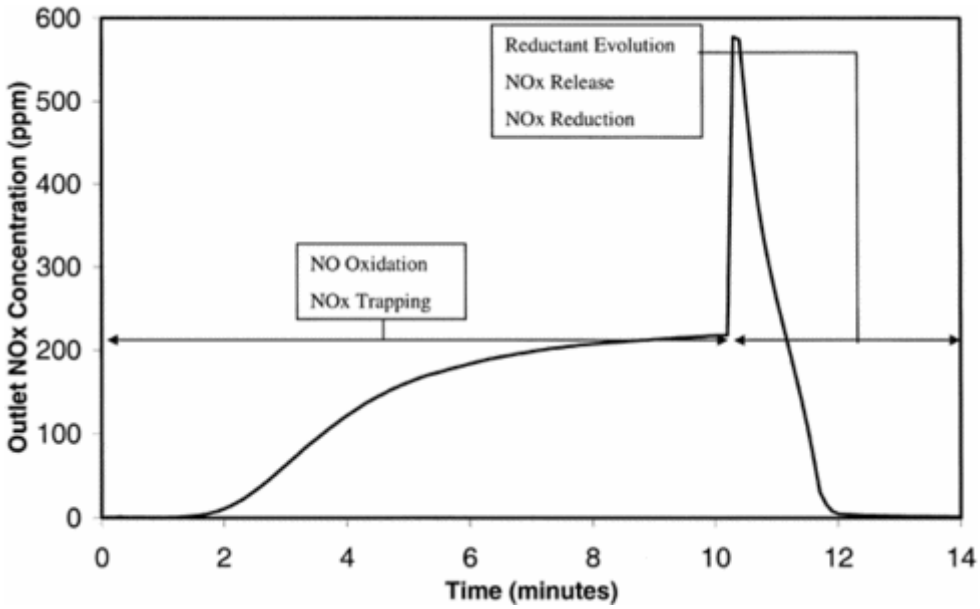

Figure 2.1.1 –LNT operating cycle [9]

release/reduction phase. The experiment was performed using a Pt/Ba/γ-Al_2O_3 LNT catalyst similar to the one used in this study [9].

2.2 – NO Oxidation

It is generally agreed upon that NO_2 is the precursor to NO_x storage on LNTs [9, 11-13]. However, since the majority of NO_x in engine exhaust is in the form of NO, the first step in the storage process must be the oxidation of NO to NO_2. Platinum (Pt) has been shown to be the most effective catalyst in the oxidation of NO when compared to other precious metals such as rhodium (Rh) and palladium (Pd). On the other hand, Rh and Pd are more active in the reduction of NO_x to N_2 [15]. This is likely the reason that all three PGM materials—Pt, Pd, and Rh—were included in the formulation of this LNT.

As reported by Olsson et al. and as seen in Figure 2.2.1, the oxidation of NO is thermodynamically limited at temperatures above 450^{o}C and is kinetically limited at temperatures below 250^{o}C [9, 16, 17, 18]. In the present study, NO oxidation will likely be less effective when evaluating at 200 and 400^{o}C than when evaluating at 300^{o}C for these reasons. High platinum loading has been shown to increase the low temperature ability of the catalyst and the use of alkali metals (Li, Na, K, Rb, and Cs) with stable NO_3^- phases, instead of alkaline earth metals (Be, Mg, Ca, Sr, and Ra), has been shown to improve the high temperature range. Also, as seen in the figure, NO conversion to NO_2 is dependent on the gas hourly space velocity (GHSV) of the flow, which is defined as the number of volumes of gas at standard temperature and pressure (STP) that flow per hour (See Section 3.4.2 for GHSV calculation). At higher space velocities the conversion is lower. This is because the residence time, the time that an element of gas is in contact with the catalyst, decreases as space velocity increases. The shorter the residence time the smaller the probability that any given NO molecule will come into contact with Pt.

Olsson et al., in formulating a kinetic model, proposed that NO oxidation occurs via two routes [16]. The first route, Equation 2.1, a Langmuir-Hinshelwood (LH) mechanism, has adsorbed O·Pt and NO·Pt reacting on the surface to form NO_2·Pt. The second route, Equation 2.2, an Eley-Rideal (ER) mechanism, has gaseous NO_2 directly reacting with O·Pt to form NO_2·Pt.

$$NO{\cdot}Pt + O{\cdot}Pt \leftrightarrow NO_2{\cdot}Pt + Pt \qquad (2.1)$$

$$NO_2(g) + O{\cdot}Pt \leftrightarrow NO_2{\cdot}Pt \qquad (2.2)$$

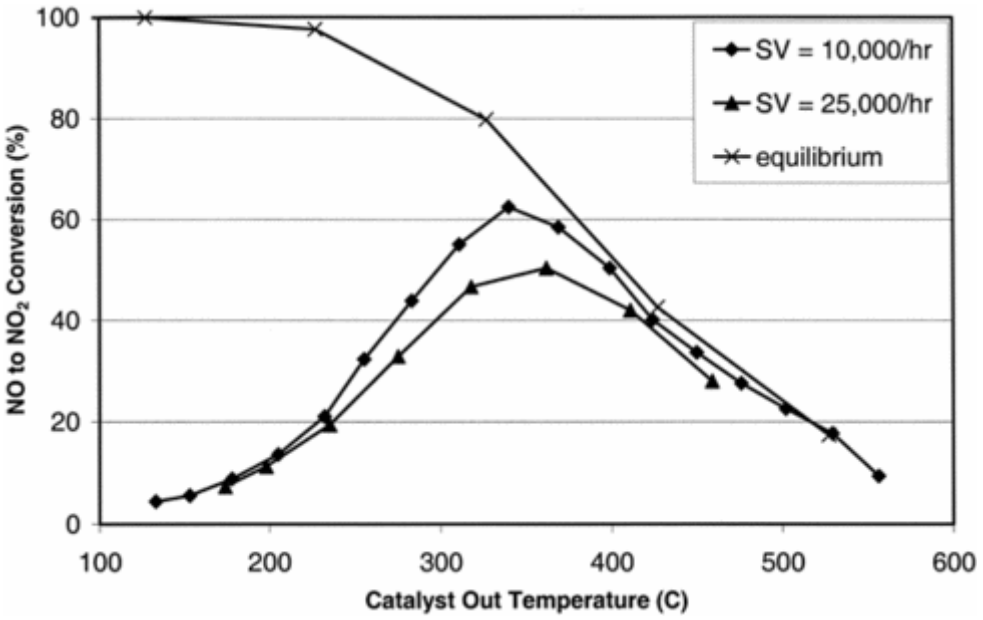

Figure 2.2.1 – NO to NO_2 conversion as a function of gas hourly space velocity and temperature on Pt/Al_2O_3 catalyst (8% O_2, 250ppm NO, and a balance of N_2) [9]

2.3 – Storage of NO_x

Once the NO has been oxidized, the next step in the reduction process is the storage of NO_x on an alkali or alkaline earth metal. Barium (Ba) and potassium (K) are commonly used, and Ba is exclusively used in the present study. The selection of a NO_x storage media must be based on the operating conditions expected. There is no single reaction that can be adequately used to describe the storage of NO_x species, and thus a number of reaction pathways have been proposed for Ba containing LNTs [9, 18, 19, 20, 21]:

- Formation of nitrite from BaO, NO and oxygen atom, and subsequent oxidation to the nitrate

$$BaO + 2NO + O^* \rightarrow Ba(NO_2)_2 \quad (2.3)$$

$$Ba(NO_2)_2 + 2O^* \rightarrow Ba(NO_3)_2 \quad (2.4)$$

- Formation of nitrate from BaO, NO_2 and oxygen atom

$$BaO + 2NO_2 + O^* \rightarrow Ba(NO_3)_2 \quad (2.5)$$

- Formation of nitrate from BaO, NO and multiple oxygen atoms

$$BaO + 2NO + 3O^* \rightarrow Ba(NO_3)_2 \quad (2.6)$$

- Intermediate barium peroxide reacts with NO_2 to form the nitrate

$$BaO_2 + 2NO_2 \rightarrow Ba(NO_3)_2 \quad (2.7)$$

- An N_2O_4 dimer forms and reacts with BaO and NO_2 to form a mixture of nitrites and nitrates. Nitrites are subsequently oxidized by oxygen to form nitrates as in Equation 2.3

$$2NO_2 \rightarrow N_2O_4 \quad (2.8)$$

$$2BaO + N_2O_4 + 2NO_2 \rightarrow Ba(NO_3)_2 + Ba(NO_3)_2 \quad (2.9)$$

- Reaction of NO_2 and BaO to form a mixture of nitrites and nitrates

$$2BaO + 4NO_2 \rightarrow Ba(NO_2)_2 + Ba(NO_3)_2 \quad (2.10)$$

Reactions 2.3 to 2.10 are either reversible or equilibrium reactions. The equilibrium is shifted toward NO_x sorption as more NO_2 is supplied. Reactions 2.3 to 2.6 require a source of oxygen, O*, which is used to form the barium nitrite or barium nitrate compound. The three sources of O^* are surface or lattice oxygen, O_2 dissociated on the precious metal, and NO_2 molecules [9].

The efficiency of these reactions depends on the barium loading. Castoldi et al. have shown that the storage capacity and the percentage of active Ba sites increase as the Ba loading increases up to 16 wt.% [22]. In Figure 2.3.1(D) the NO outlet concentration shows no NO_x slip for 350s for a catalyst with 16 wt.% Ba. On the other hand, NO_x slip is

observed as soon as the sample with no Ba is exposed to the simulated exhaust gases as can be seen in Figure 2.3.1(A) [22]. This indicates that Ba significantly increases the NO_x storage ability of the catalyst. In the LNT used in this study the washcoat is loaded with approximately 4-7 wt.% Ba, so it's NO_x storage capacity should be much greater than that of the sample with no Ba. Furthermore, Piacentini et al. have proposed that different Ba loadings actually lead to distinct barium phases, with different NO_x storage abilities. They studied Pt-Ba/ceria, Pt-Ba/zirconia, and Pt-Ba/γ-Al_2O_3 systems and found that a low-temperature, XRD amorphous $BaCO_3$ phase existed exclusively on samples with less than 4.5 wt.% Ba, whereas a high-temperature, less reactive, crystalline phase increased in quantity with higher loadings [23, 24].

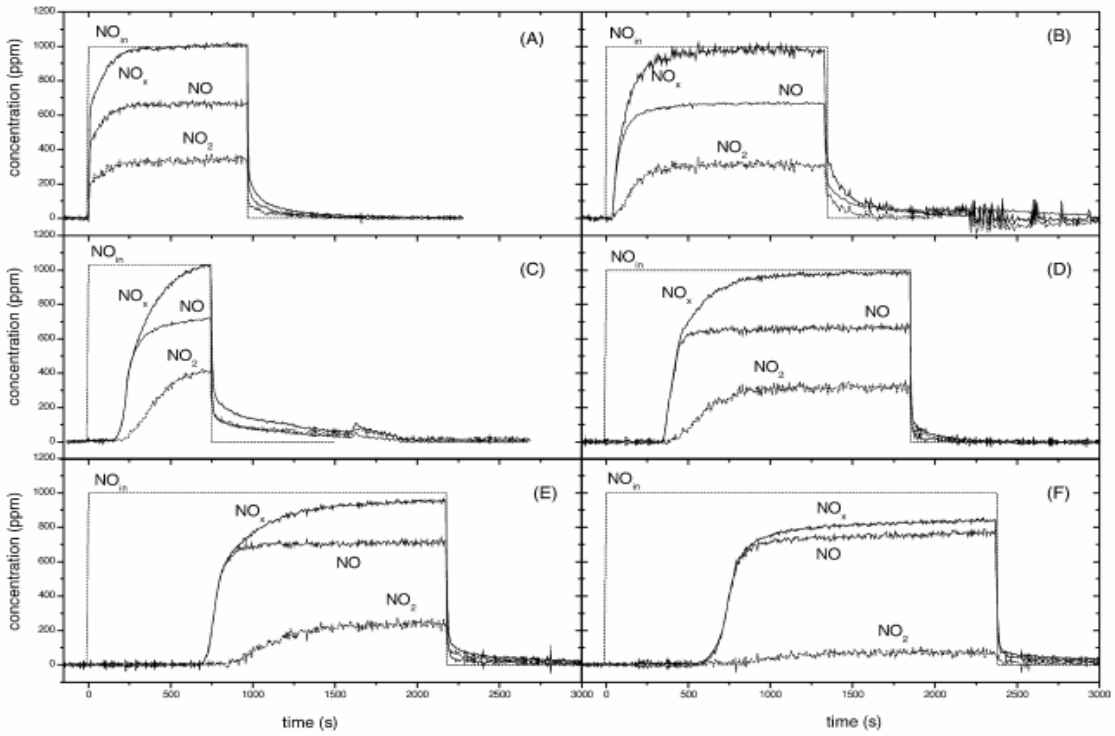

Figure 2.3.1 – NO and NO_2 outlet concentration upon NO addition on a Pt/Ba/γ-Al_2O_3 catalysts at 350^{o}C: (A) 0% Ba; (B) 5% Ba; (C) 10% Ba; (D) 16% Ba; (E) 23% Ba and (F) 30% Ba [22]

Though not explicitly stated in equations 2.3.1 to 2.3.8, the NO_2 present is a result of the NO to NO_2 oxidation reaction that occurs over the precious metal component. Forzatti et al. have explained the trapping process with two basic routes: the "nitrate route" and the "nitrite route" [25]. The "nitrate route" requires oxidation of NO to NO_2 over Pt followed by disproportionation of NO_2 on Ba sites to form nitrates. In the "nitrite route" NO is oxidized to NO_2 over Pt and stored as nitrites on neighboring Ba sites. The nitrites are then oxidized to nitrates. The nitrite route could potentially dominate with high Ba loading.

The NO_x storage mechanisms of the catalyst are also affected by the gas constituents present. If no CO_2 or H_2O are present in the exhaust stream, then all of the Ba will be in the form of BaO, the best NO_x storage medium according to Nova et al [26, 27]. However, if, as is the case with diesel engine exhaust and the simulated diesel exhaust gases used in this study, CO_2 and H_2O are present in the exhaust stream, then barium hydroxide, $Ba(OH)_2$, and barium carbonate, $BaCO_3$, also coexist with BaO on the surface of the catalyst with NO_x storage occurring first on BaO, then on $Ba(OH)_2$, and finally on $BaCO_3$ [27]. The evolution of CO_2 can be seen in Figure 2.3.2 as NO_x reacts with $BaCO_3$ and CO_2 is released [27]. There is a short time lag between the introduction of NO and the release of CO_2 because NO_x first reacts with BaO sites.

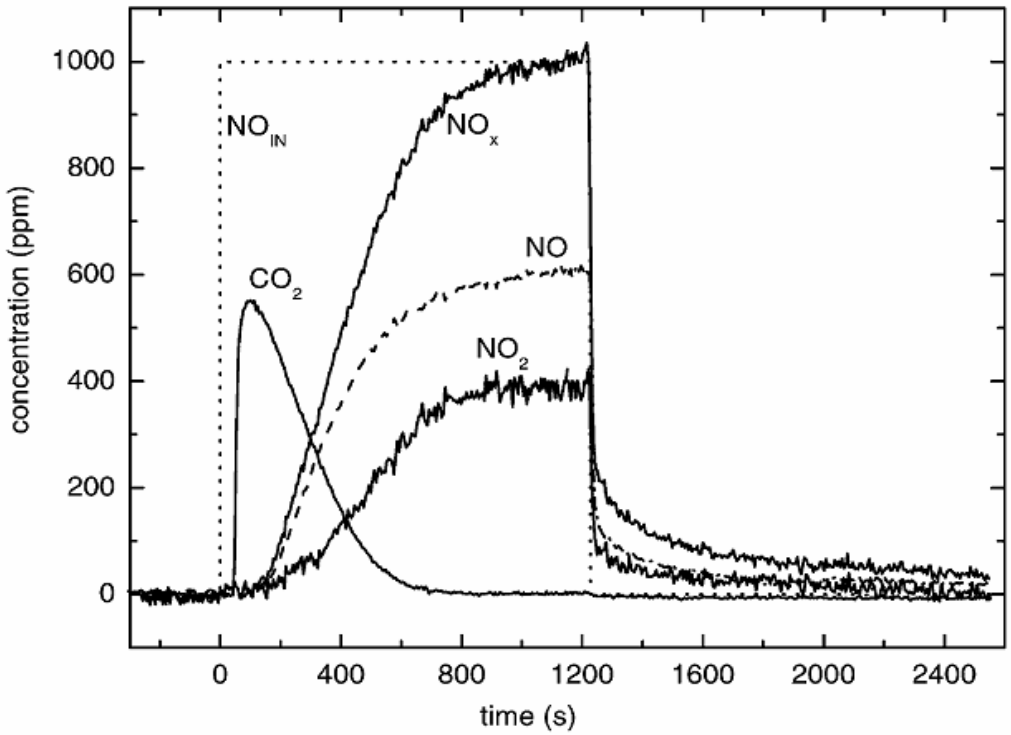

Figure 2.3.2 – Results of NO step addition (in He + 3% O_2) over Pt/Ba/Al_2O_3 at 320°C. NO, NO_2, NO_x, and CO_2 outlet concentrations [27]

Recently, researchers have also analyzed the effect that Ba, the conventional NO_x storage media, has on low temperature NO_x storage capacity and NO_x conversion. Xu et al. compared the NO_x conversion of a Pt/Rh/Ba/Al_2O_3 LNT to that of a Pt/Rh/Al_2O_3 LNT while switching between a 24 s lean phase and a 6 s rich phase. They found that at temperatures below 200°C the LNT with only Al_2O_3 as the NO_x storage media achieved higher NO_x conversions, and they attributed this to the lower surface nitrate stability and higher release rate of nitrates stored on γ-Al_2O_3 in comparison to Ba [28]. However, at or above 200°C, the same temperatures used in the present study, the NO_x conversions of the two LNTs were similar.

2.4 – Regeneration of LNTs during the Rich Event

LNT operation requires the periodic release and reduction of the trapped NO_x. By adding a mixture of reductants to the exhaust stream a net reducing environment is achieved. A variety of reductants can be used with H_2, CO and HC being three of the most common. The goal of the regeneration step, regardless of the reductants used, is the creation of a net reducing environment in which the stored NO_x can readily be released and converted to N_2. This means that enough reductant must be injected to remove all the gas phase O_2 as well as all the O_2 stored on the surface of the catalyst [9]. The higher the oxygen storage capacity (OSC) of the catalyst, the greater the quantity of reductant needed to react with all the stored O_2 and also reduce the stored NO_x. The OSC of LNTs is determined by the loading of oxygen storage components; two of the most commonly used in LNTs being cerium and cerium-zirconium oxides [29, 30]. This is not to say that the function of oxygen storage components is limited to O_2 adsorption/desorption. The introduction to LNTs of cerium and cerium-zirconium oxides has also been shown to promote NO_x conversion in the temperature range of 200 to 400^{o}C and to stabilize LNT components (See Section 2.5 for more about the stabilization effects) [31, 32]. If an insufficient quantity of reductants is supplied, incomplete surface regeneration will result in an accumulation of nitrites and nitrates on the surface of the catalyst. Consequently, in the next cycle, fewer storage sites will be available and the trapping capacity of the catalyst will continue to decrease until the amount of NO_x being stored and released are approximately the same.

2.4.1 – NO_x Release

Epling et al. have proposed two primary mechanisms for the release of NO_x: thermal and equilibrium release [9]. Thermal release of NO_x can occur as a result of exothermic reactions between reductants and O_2, either in the gas phase or on the catalyst surface. Stored nitrates become less stable at high temperatures and decompose as a result. This mechanism results in a significant release of NO_x if the temperature exotherm is large or if a large amount of NO_x is stored on the catalyst. The second mechanism, equilibrium release, is controlled by the partial pressure of O_2. As O_2 is consumed by the reductants, the concentration of O_2 decreases and the stored nitrates may be reduced to nitrites, which are significantly less stable and more likely to be released.

The concentration of the chemical species in the exhaust gases also affects the extent of the NO_x release. Amberntsson et al. have demonstrated that CO_2 enhances NO_x release and that O_2 has a suppressive effect on the CO_2 enhanced release [33]. They concluded that increasing the amount of CO_2 decreases the stability of the stored nitrates and O_2 negatively affected the release of NO since once released, NO cannot be oxidized to NO_2 without the presence of O_2, and thus, cannot be re-adsorbed further downstream. However, it's not actually the release but the reduction of NO_x that is affected by O_2, an obvious conclusion, since the reason for a rich phase is the creation of a net reducing environment. Similarly, the addition of H_2O to a rich flow containing H_2 and CO_2 has been shown to reduce the NO_x release [34]. Figure 2.4.1 corroborates this conclusion [9].

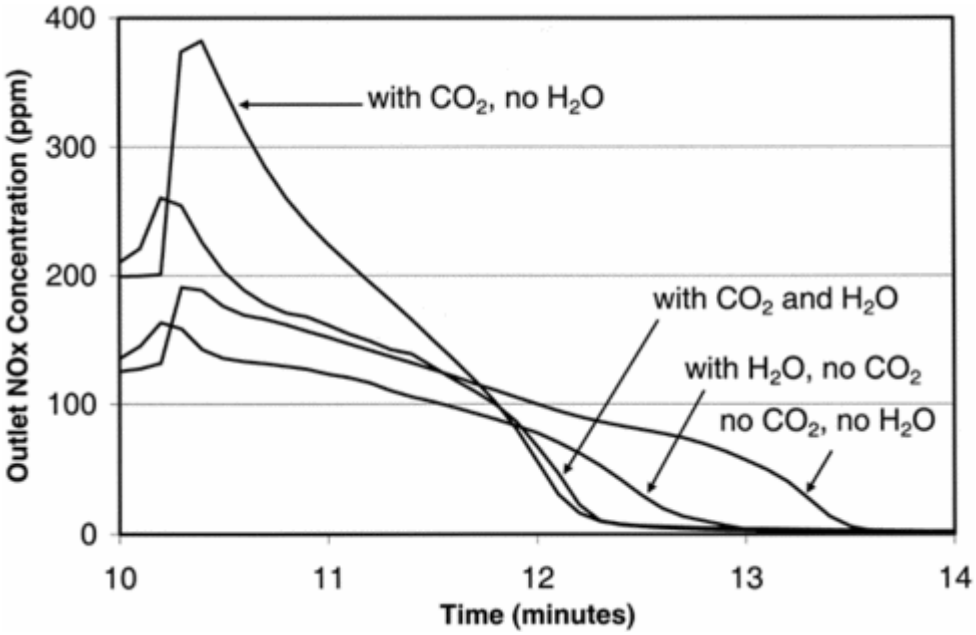

Figure 2.4.1 – NO_x release from a pre-nitrated $Pt/Ba/Al_2O_3$ sample at 375°C and a GHSV of 25,000 h^{-1}. Regeneration gases contained 1500 ppm H_2, 0 or 8% CO_2, and 0 or 8% H_2O in a N_2 balance [9]

2.4.2 – NO_x Reduction

Once the NO_x has been released, it must be quickly reduced in order to minimize NO_x breakthrough during the rich phase. The precious metal component is the active reducing agent with the alkali or alkaline-earth metals acting as promoters. Na and Ba have been shown to weaken the N-O bond, which, by making dissociation of NO_x easier, leads to more facile reduction. They have also been shown to increase the selectivity of the NO_x reduction reaction to N_2.

The specific reductants used determine the effectiveness of the release/reduction step. Poulston et al. reported that H_2 is the most effective reductant, especially at lower temperatures and at all temperatures after aging [35]. Figure 2.4.1 clearly shows that nitrates are more quickly desorbed and that more of the desorbed nitrates are fully

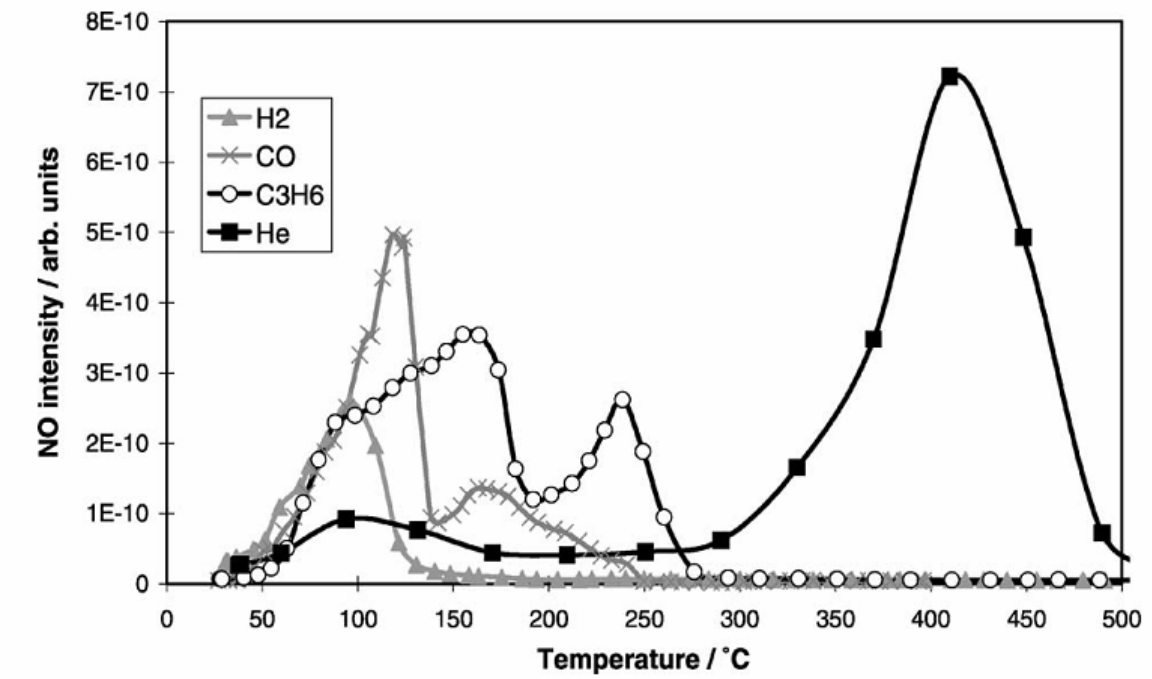

Figure 2.4.2 – Temperature programmed desorption of a Pt/Ba-based LNT catalyst in flows of 10% of the stated gases in N_2 or He except for He which is He only [35]

reduced to N_2 with a gas flow consisting of 10% H_2 than with a gas flow consisting of either 10% CO or 10% C_3H_6. James et al. claimed that using H_2 as a reductant enables the decomposition of $Ba(NO_3)_2$ as well as the reduction of the released NO_x [36]. CO was also reported to decompose $Ba(NO_3)_2$ but was not as effective at reducing the released NO_x. Figure 2.4.3 shows a pulsed flow experiment performed at 300^{o}C in which CO is added after a brief NO_x storage period. In similar experiments with H_2, N_2 was produced as a result of the H_2 addition, indicating that H_2 is more effective at reducing NO_x than CO. The authors assumed that CO poisoned the Pt sites, which catalyze NO reduction to N_2.

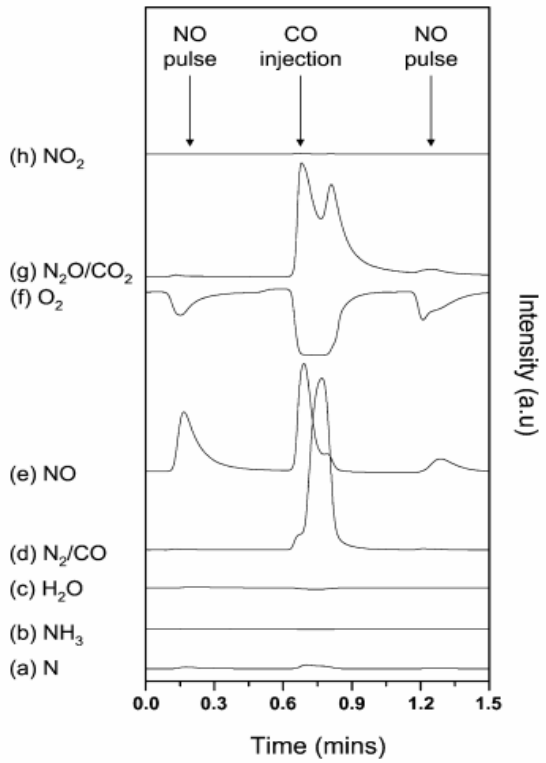

Figure 2.4.3 – Pulsed flow NSR experiment over a $Pt/Ba/Al_2O_3$ catalyst at 300°C. NO is pulsed every 60 s into a flow of 10% O_2 in He at 25 cm^3/min. Two cm^3 of CO was injected in between NO pulses [36]

Nova et al. have studied the effect of catalyst formulation on the reduction of NO_x over a Ba/Al_2O_3 catalyst, a $Pt/Ba/Al_2O_3$ ternary catalyst, and a physical mixture consisting of Pt/Al_2O_3 and Ba/Al_2O_3 [37]. They found that Pt significantly promotes the decomposition of nitrates when they compared the ternary formulation to the Ba/Al_2O_3. Also, when the ternary catalyst and the physical mixture were compared they found that Pt only affects nitrate stability if it is on the same support particle as Ba. The authors also investigated the effect of a reducing environment on the stability of adsorbed nitrates on the catalysts after saturating each of the three catalysts with NO_x at 350°C. In the case of the ternary $Pt/Ba/Al_2O_3$ catalyst, the stored nitrates were reduced at temperatures as low

as 140°C. However, reduction of nitrates did not occur until close to the adsorption temperature of 350°C with the other two catalyst formulations.

2.5 – Effect of Temperature and Deactivation Mechanisms

The effect that high temperature aging has on the NO_x storage and reduction mechanisms will now be considered. Extremely high temperatures, such as those experienced during desulfation treatments, can lead to sintering and partial deactivation of active components, phase change and surface area reduction of high surface area support material, and changes in the physicochemical properties, agglomeration, or migration of the storage media.

2.5.1 – Pt Group Metal (PGM) Sintering

Sintering of the precious metal component in LNTs as a result of high temperature aging is a serious problem [38- 43]. Kim et al. have studied the effect of high temperature aging on a simple model $Pt/Ba/Al_2O_3$ LNT [43]. The average Pt particle size was approximately 2.5 nm before aging. However, as seen in Figure 2.5.1, after aging at 900°C for 17 hours the Pt particles had an average size of 34 nm. The effect that aging and Pt particle size growth has on NO_x conversion is seen in Figure 2.5.2. Clearly, the fresh sample stores much more NO_x and has a longer breakthrough time than either of the samples aged in an H_2 or an O_2 environment [43]. On the other hand, Nguyen et al. saw almost no reduction in steady state NO_x conversion after average Pt particle size growth

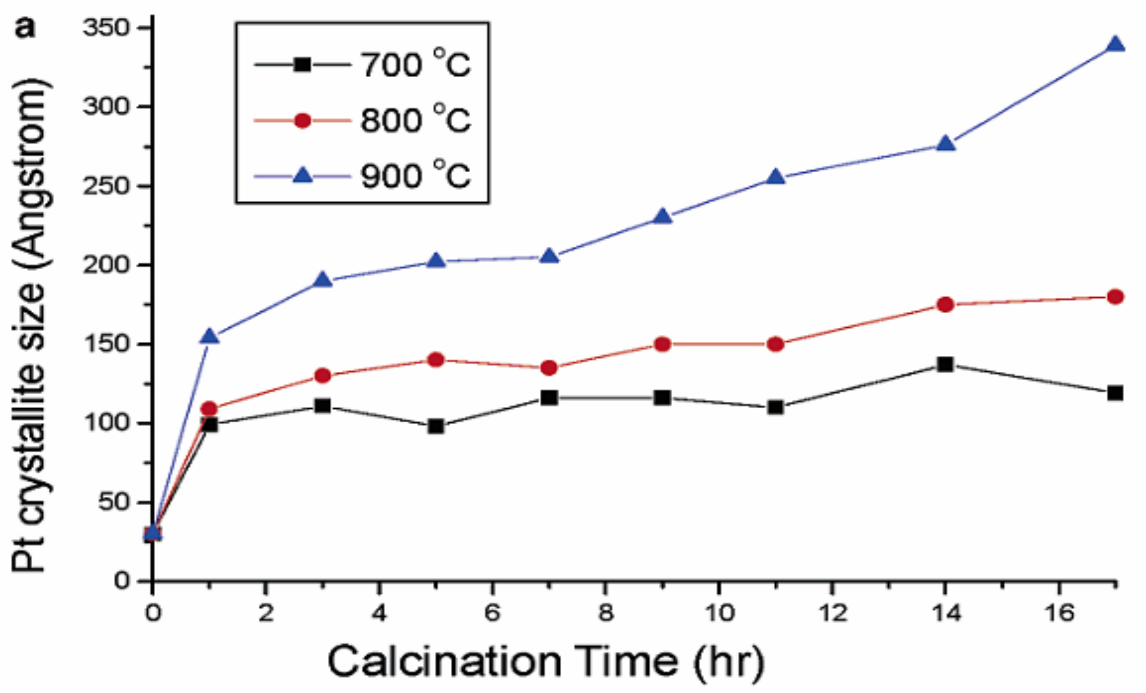

Figure 2.5.1 – Effect of aging temperature and aging time on Pt crystallite size [43]

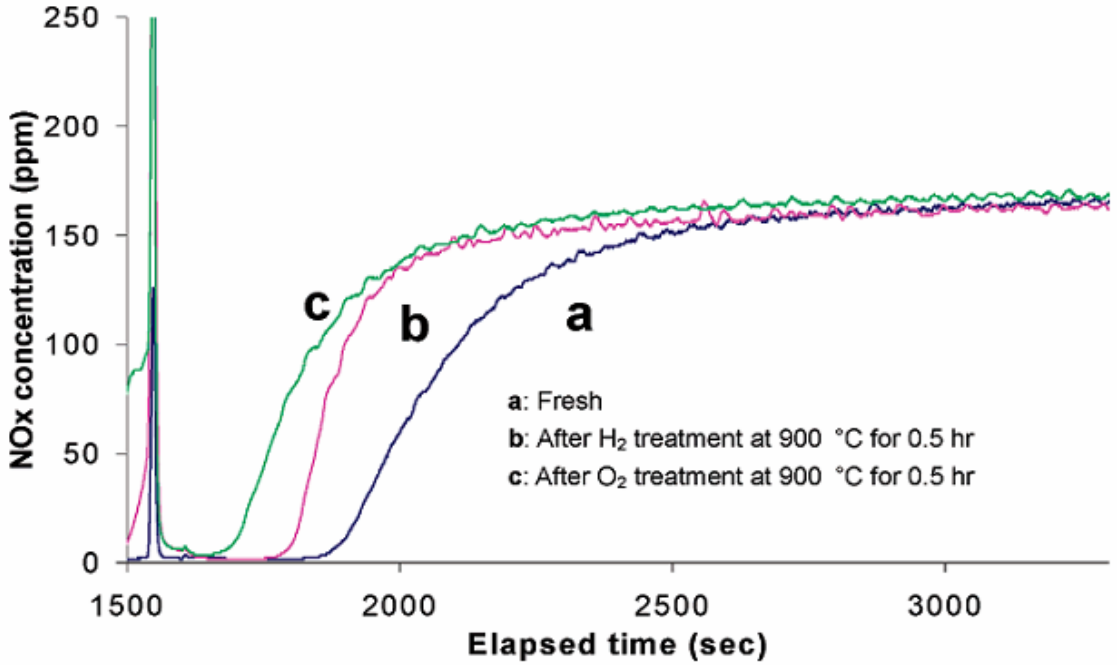

Figure 2.5.2 – NO_x uptake profiles for fresh LNT (a) and LNTs treated with either 10% H_2/He (b) or 10% O_2/He (c) [43]

to 8 and 10 nm as a result of cyclic aging at nominal aging temperatures of 700 and 800^{o}C, respectively, on model "Ba+K" LNTs [40]. Reduction in NO_x conversion followed aging at 900 and 1000^{o}C, but the effect of average Pt particle size growth could not be resolved because of simultaneous surface area reduction. Furthermore, Olsson et al. have given evidence that Pt particle growth can actually improve the oxidation and reduction activity of Pt. As seen in Figure 2.5.3, the reduction of NO_2 to NO over a $Pt/Ba/Al_2O_3$ catalyst was slightly more effective when the LNT was pretreated at 650^{o}C than it was when the LNT was pretreated at 450^{o}C. A similar increase in efficiency for the oxidation of NO to NO_2 was seen at higher pretreatment temperatures. The authors speculated that smaller Pt particles more easily form activity-limiting oxides than larger particles [44].

Nagai et al. have determined that Pt particles supported on only Al_2O_3 sinter more significantly than Pt particles supported on Ce-Zr-Y mixed oxides [45]. A sample with ~1 nm Pt particles impregnated on a Al_2O_3 support was analyzed after aging in air at 800^{o}C for 5 hours, and the Pt particles had grown up to a size of 20 nm. However, when Pt was supported on a ceria-based mixed oxide (Ce-Zr-Y mixed oxide), no particle growth was observed after the same aging treatment. It appears that the Pt-O-Ce bond acts as an "anchor" and hinders the sintering of Pt. As previously mentioned, this is one reason for the introduction of oxygen storage components. The effect of Ce and Zr on the Al_2O_3 support will be addressed in the next section.

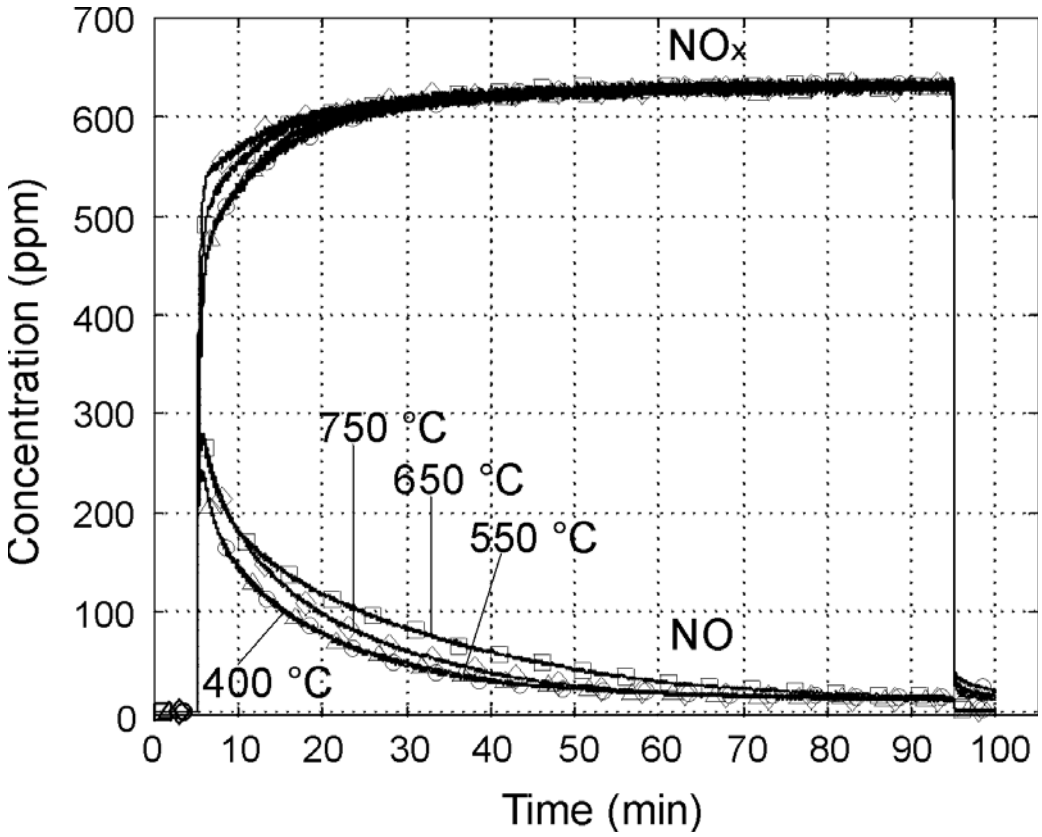

Figure 2.5.3 – NO and NO_x outlet concentrations while exposing a $Pt/Ba/Al_2O_3$ catalyst to 620 ppm NO_2 in Ar at 350°C. Pretreatment temperatures are indicated in the figure [44]

2.5.2 – Phase Transformation of γ-Al_2O_3

The high surface-area γ-Al_2O_3 support is critical for effective NO_x reduction. The large surface area (~200 m^2/g) provides a plethora of sites for active catalyst components such at PGM, Ba, Ce, and Zr to disperse without agglomerating. However, high temperature aging can significantly decrease the surface area of the Al_2O_3 support. As seen in Figure 2.5.4, the surface area of Al_2O_3 decreases from 200 m^2/g at 600°C to less that 5 m^2/g at 1400°C [47]. This decrease in surface area is due to the phase transition from γ-Al_2O_3 to α-Al_2O_3. Figure 2.5.5 shows the phase transitions of Al_2O_3 and the temperatures at which they occur. Arai et al. reported that addition of either BaO, La_2O_3, SiO_2, Li_2O or K_2O can increase the phase transition temperature of Al_2O_3 [47].

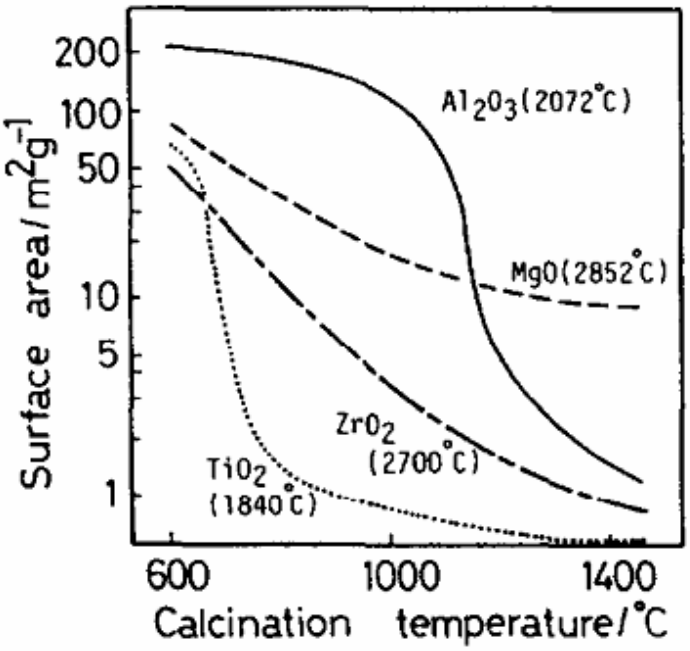

Figure 2.5.4 – Temperature dependence of the surface area of oxide supports. Melting points are shown in parentheses [47]

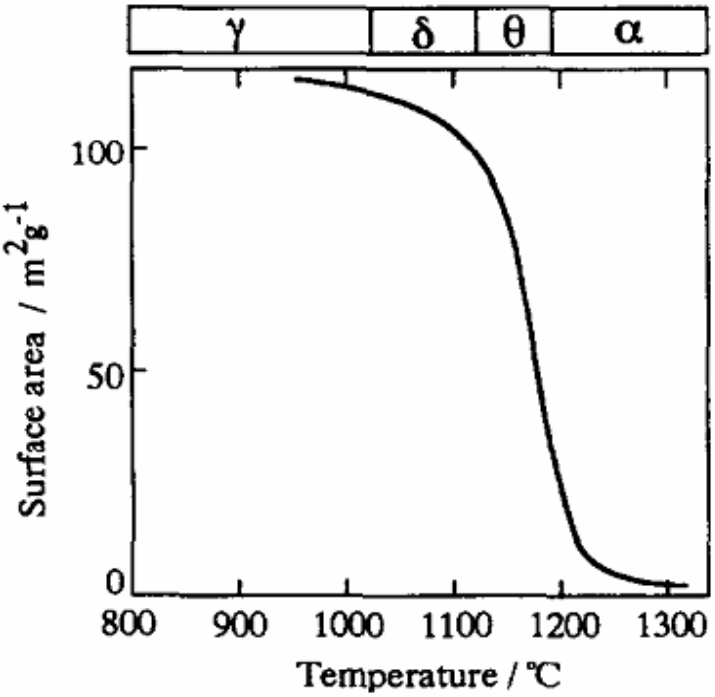

Figure 2.5.5 – Phase transformation and surface area of Al_2O_3 as a function of temperature [47]

Several researchers have studied the effect that surface area reduction has on NO_x conversion of LNTs. Both Nguyen et al. and Toops et al. have shown that reductions in surface area closely correlate with reductions in NO_x conversion [40, 48]. Toops et al. found that the total surface area of a $Pt/Rh/Ba/Al_2O_3$ LNT (cordierite + washcoat) decreased from 28 to 17 m^2/g after cyclic aging in an engine at an average temperature of 780^oC, and that this reduction in surface area correlated well with a reduction in steady state NO_x conversion when evaluating at 400^oC from 68 to 44% after the same aging treatment. However, this LNT did not contain any stabilizers such as Ce, and it is expected that the additives in this fully-formulated LNT may help limit surface area reductions.

Wu et al. studied the effect of Ce-Zr mixed oxides on the phase transition stability of Al_2O_3 at elevated temperatures [49]. They found that the transformation to α-Al_2O_3 could be delayed until temperatures above 1222^{o}C with the addition of Ce-Zr mixed oxides. The concentration of the oxides was varied, and the best stabilizing effect was observed for 20% of Ce-Zr mixed oxides. A Minor θ-Al_2O_3 phase was detected after aging at 1050^{o}C for 50 hours on samples with ≥20% Ce-Zr mixed oxides doping concentration.

Lanthanum (La) has also been shown to stabilize Al_2O_3 at high temperatures. Experiments performed by Ozawa et al. have compared La-doped Al_2O_3 samples with pure Al_2O_3 samples. At 1200^{o}C the surface area of a 0.5 - 1.5 mol % La/Al_2O_3 sample was 88-92 m^2/g, which was much higher than 45 m^2/g for pure Al_2O_3 at the same temperature [50]. Below 1000^{o}C, the addition of La did not have an appreciable impact on the surface area of Al_2O_3. The catalysts used in the present study contain La, and so it is not expected that the γ-Al_2O_3 will transition to δ-Al_2O_3 even at the highest temperature experienced in this study (1070^{o}C).

2.5.3 –Physicochemical Changes of Barium

Kim et al. have reported that thermal aging at 1000^{o}C for 10 hours of a highly dispersed BaO/$BaCO_3$/Al_2O_3 LNT led to the formation of low surface area crystalline $BaAl_2O_4$ [51]. Figure 2.5.6 shows the XRD patterns from samples calcined at 500, 900, and 1000^{o}C. The $BaAl_2O_4$ diffraction peaks at 2θ = 19.60, 28.20, and 34.30^o not seen in the samples calcined at 500 and 800^{o}C are clearly seen in the sample calcined at 1000^{o}C.

Kim et al. also observed the formation of a $BaAl_2O_4$ phase after aging a model $Pt/Ba/Al_2O_3$ LNT at 900°C in a flow of 10% O_2/He [43].

The effect of Ba loading and calcination temperature on the formation of $BaAl_2O_4$ on a BaO/Al_2O_3 LNT was studied by Szailer et al. [52]. LNTs with Ba loadings of 2, 8, and 20 wt.% BaO/Al_2O_3 were calcined at temperatures of 500, 800, 900, and 1000°C. The XRD spectra taken of these samples are shown in Figure 2.5.7. The spectra taken of the samples with 2 and 8 wt.% BaO/Al_2O_3 do not show evidence of $BaAl_2O_4$ formation even after calcining at 1000°C. However, $BaAl_2O_4$ formation is seen on the sample with 20 wt.% BaO/Al_2O_3 after calcining for 2 h at a temperature of 800°C, and the intensity of the peak grows as the aging temperature is increased.

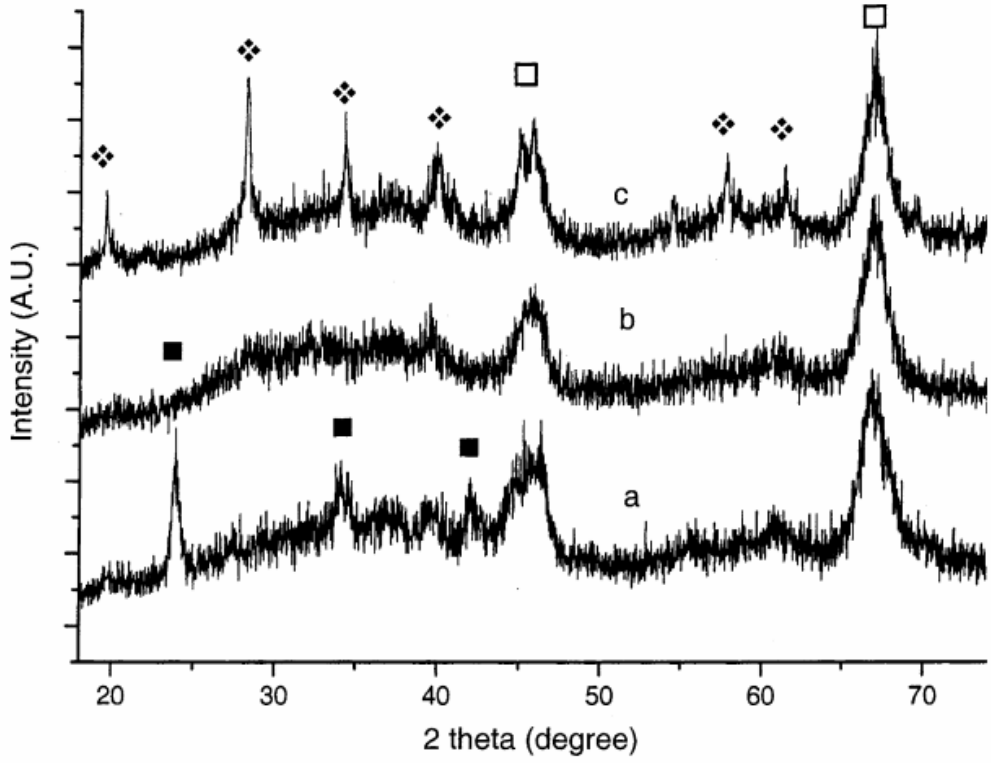

Figure 2.5.6 – XRD patterns of 20 wt% BaO/Al_2O_3 samples calcined at 500°C (a), 900°C (b), and 1000°C (c) (■: $BaCO_3$,□: Al_2O_3, ❖ $BaAl_2O_4$) [51]

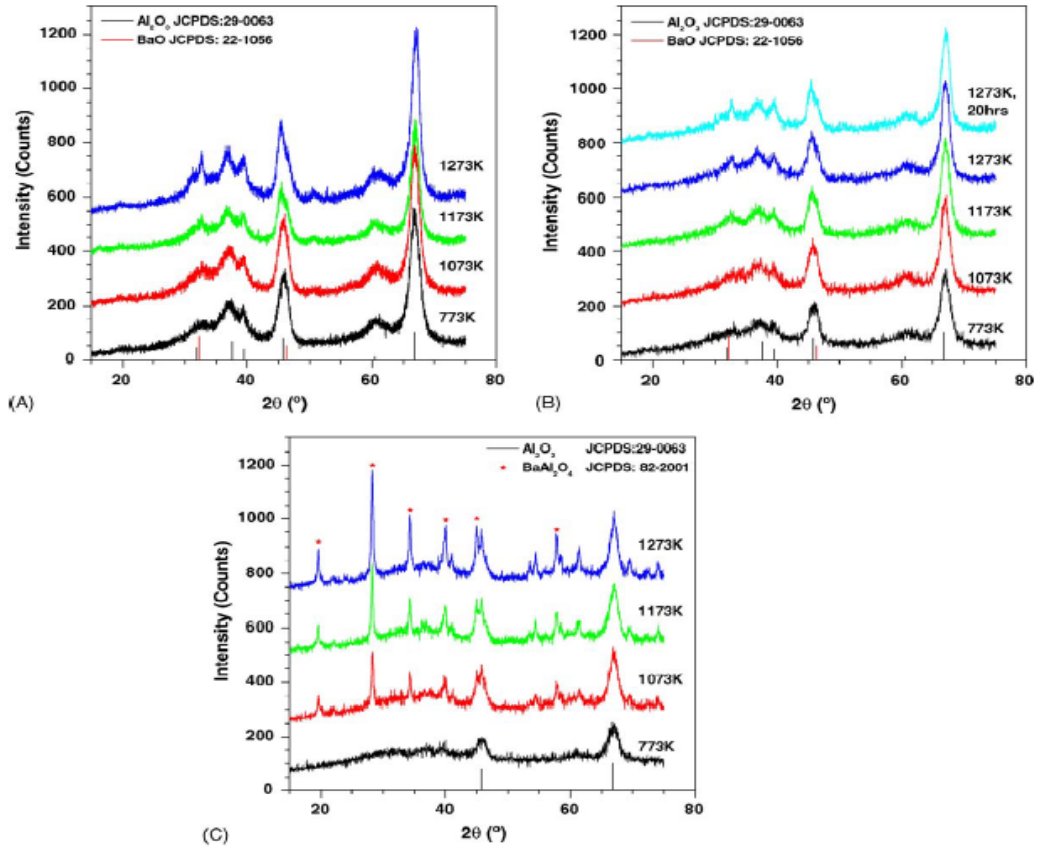

Figure 2.5.7 – XRD spectra of 2 wt.% (A), 8 wt.% (B), and 20 wt.% BaO/Al_2O_3 (C) LNT catalysts after calcining for 2 h at different temperatures [52]

The authors speculate that with lower loadings of Ba (6 and 8 wt.%) a very stable monolayer of Ba forms on the Al_2O_3 support, but once the Al_2O_3 is completely covered with a monolayer, any additional Ba added to the catalyst is much less stable than the monolayer. They speculate that it is this additional Ba that reacts with Al_2O_3 to form $BaAl_2O_4$. However, more recent literature has indicated that a Ba loading of 16 to 25 wt.% is necessary for a monolayer coverage [22, 53].

The effect that $BaAl_2O_4$ has on NO_x conversion is not universally agreed upon. Epling et al. and Jang et al. have stated that high temperature $BaAl_2O_4$ formation acts as a deactivation mechanism by decreasing the overall number of NO_x storage sites [9, 54, 55].

However, Hodjati et al., in a series of papers comparing the NO_x sorption/desorption abilities and the sulfur tolerance of BaO and $BaAl_2O_4$, found $BaAl_2O_4$ to be a good candidate for NO_x trapping applications [56, 57]. They claimed that strongly bonded carbonates, which readily form on BaO, do not compete with nitrates for sorption sites on $BaAl_2O_4$. In Figure 2.5.8, infrared spectra of a BaO and a $BaAl_2O_4$ sample saturated with NO_x at 25^oC, the band at 1430 cm^{-1}, found only on the BaO spectra, is representative of a unidentate carbonate.

Migration and agglomeration of the NO_x storage media must also be considered as possible deactivation mechanisms. Nguyen et al. have reported that cyclic aging significantly effects the storage media of model "Ba+K" LNTs [40]. The researchers used EPMA elemental maps shown in Figure 2.5.9 to show that aging experiments similar to those performed in the current study induce the migration of potassium from the washcoat to the substrate at temperatures as low as 830^oC. Furthermore, Ba migration is found to occur at temperatures close to 830^oC and an eventual transition from $BaCO_3$ to $BaAl_2O_4$ occurs around 1000^oC.

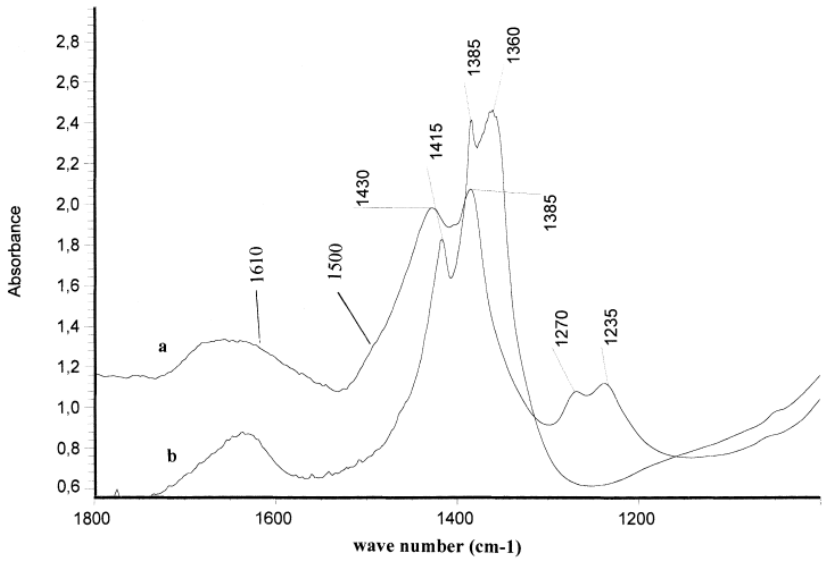

Figure 2.5.8 - Infrared spectra of catalysts saturated with NO_x at 25°C: (a) BaO; (b) $BaAl_2O_4$ [56]

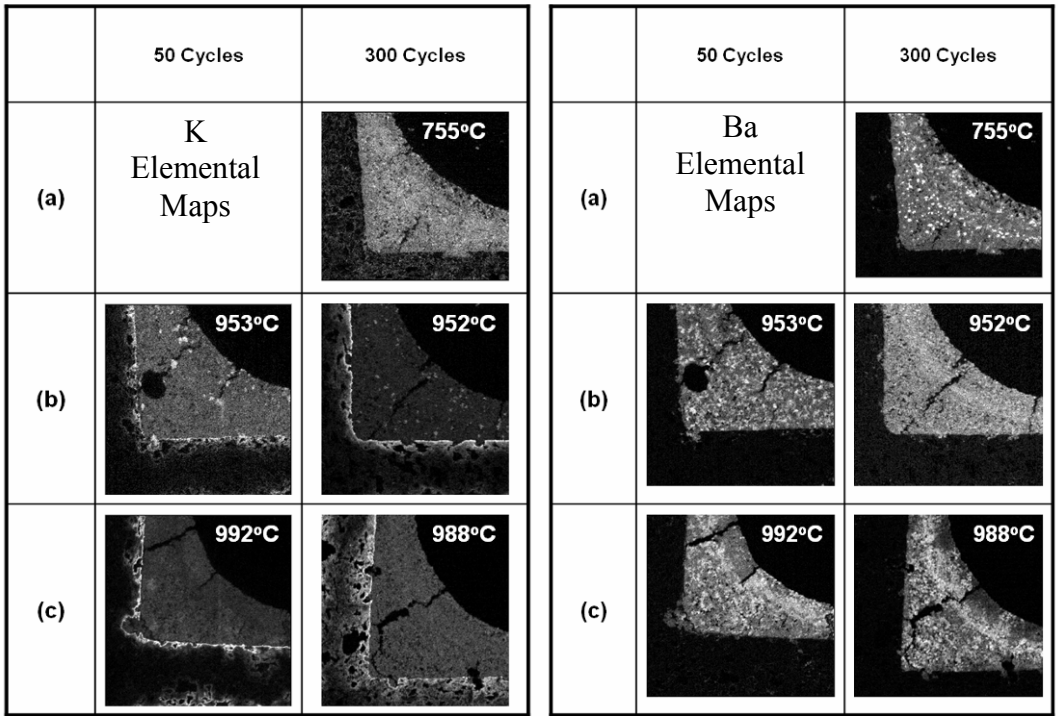

Figure 2.5.9 – Migration of K (Left) and agglomeration of Ba (Right) after aging a model "Ba+K" LNT at the indicated temperature for either 50 or 300 cycles [40]

Chapter 3

EXPERIMENTAL APPARATUS

This section provides a detailed description of the experimental apparatus used to evaluate and age the catalysts and a brief explanation of the equipment used to perform surface characterization studies. Section 3.1 is an overview of the bench-flow reactor (BFR). Sections 3.2 and 3.3 describe the LNT reactor and the components of the BFR. The procedures and the gas compositions used for aging and evaluation experiments are outlined in Section 3.4. The chapter is closed out with a list of the techniques used to investigate the effects of aging on the catalysts in Section 3.3.

3.1 – Overview of Bench-Flow Reactor

A bench-flow reactor (BFR) located in the University of Tennessee's Science and Engineering Research Facility (SERF) is used to age and evaluate LNTs in the current study. Figures 3.1.1 and 3.1.2 are, respectively, a photograph and a schematic of the BFR. The BFR is used to control and analyze the gases sent to the LNT reactor. Mass flow controllers (MFCs) control the concentrations of the lean and rich bank gases, and two 3-way switching valves are used to switch between the two banks. A peristaltic water pump and a tube heater generate steam which is pushed through the steam generator with carrier gases (N_2 and CO_2). The carrier gases as well as all other gases are pre-heated by heat tapes and temperature controllers before they get to the reactor or the steam generator.

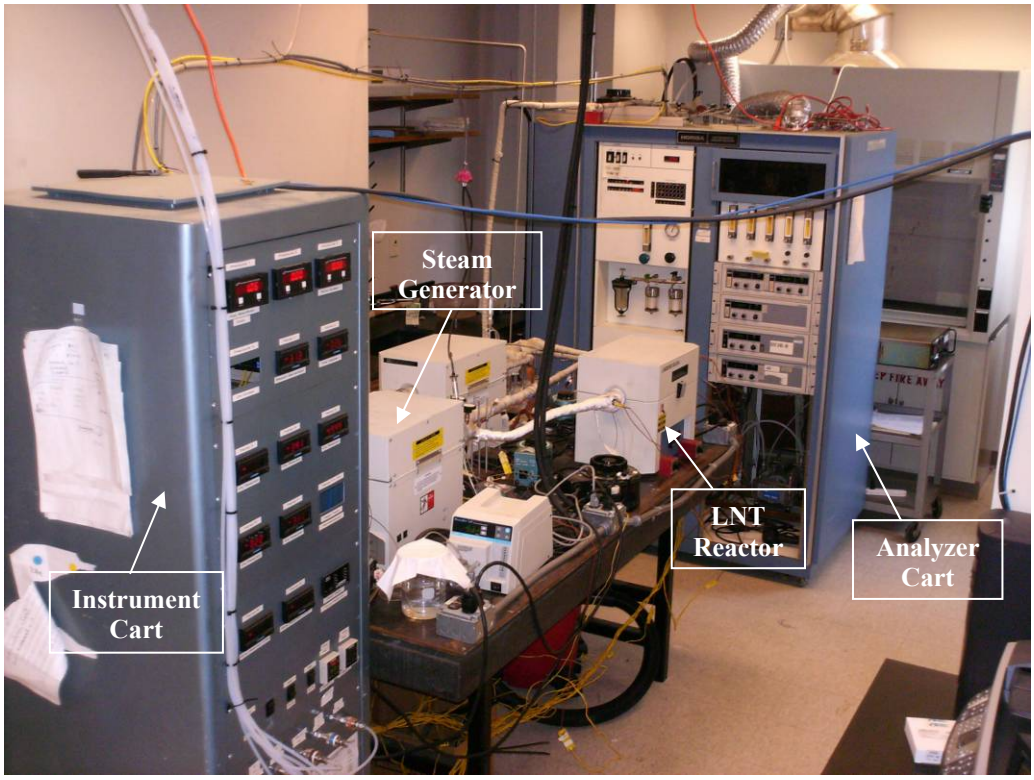

Figure 3.1.1 – Photograph of the Bench-Flow Reactor (BFR)

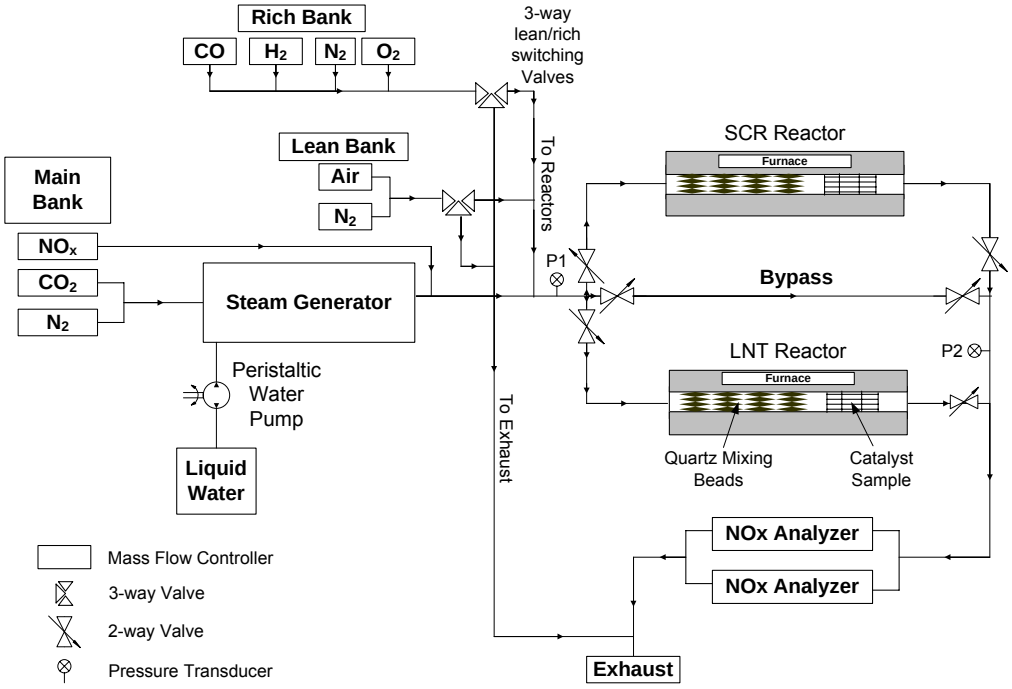

Figure 3.1.2 – Schematic of the Bench-Flow Reactor

Six high temperature valves direct the gas flow to either the LNT reactor or the bypass line. After either passing through one of the two reactors or the bypass line, the gas is pumped through the two NO_x analyzers which determine the concentrations of NO and NO_x in the exhaust gases. An ammonia trap is used to remove ammonia from the system before the analyzers since ammonia can form in LNT experiments. The components of the BFR are explained in detail in the following sections.

3.2 – Lean NO_x Trap System

The Lean NO_x Trap (LNT) system consists of a LNT catalyst, a quartz tubular reactor, and a Lindberg/Blue Minimite furnace.

3.2.1 – Catalyst and Reactor

The catalyst used in this study is a fully-formulated Delphi Lean NO_x Trap. The exact composition of the washcoat is unknown, but XRD Rietveld analysis and EPMA line scans have been used to approximate the concentrations of known washcoat components. These concentrations and the method used to obtain them are shown in Table 3.1. These concentrations only add up to about 90% because approximately 10 wt.% of each XRD sample was cordierite. The cored samples are 7.6 cm long and 2.15 cm in diameter with a cell density of 46.5 cells/cm^2 (300 cpsi). The catalyst is wrapped in FiberFLEX^{TM} glass wool and inserted into a quartz tube with an inside diameter of 2.2 cm, an outside diameter of 2.54 cm, and a length of 45.7 cm. To enhance mixing and preheating of the simulated exhaust gases the front half of the quartz tube is filled with

Table 3.1 – LNT washcoat component concentrations and the method used to determine each concentration

Component	**Concentration (wt.%)**	**Method**
Al_2O_3	66	XRD Rietveld
PGM (Pt, Pd, and Rh)	1	XRD Rietveld and EPMA Line Scans
Ba	4 to 7	XRD Rietveld and EPMA Line Scans
CeO	9.5	XRD Rietveld
$Ce_2Zr_3O_{10}$	8.5	XRD Rietveld
La	1	EPMA Line Scans

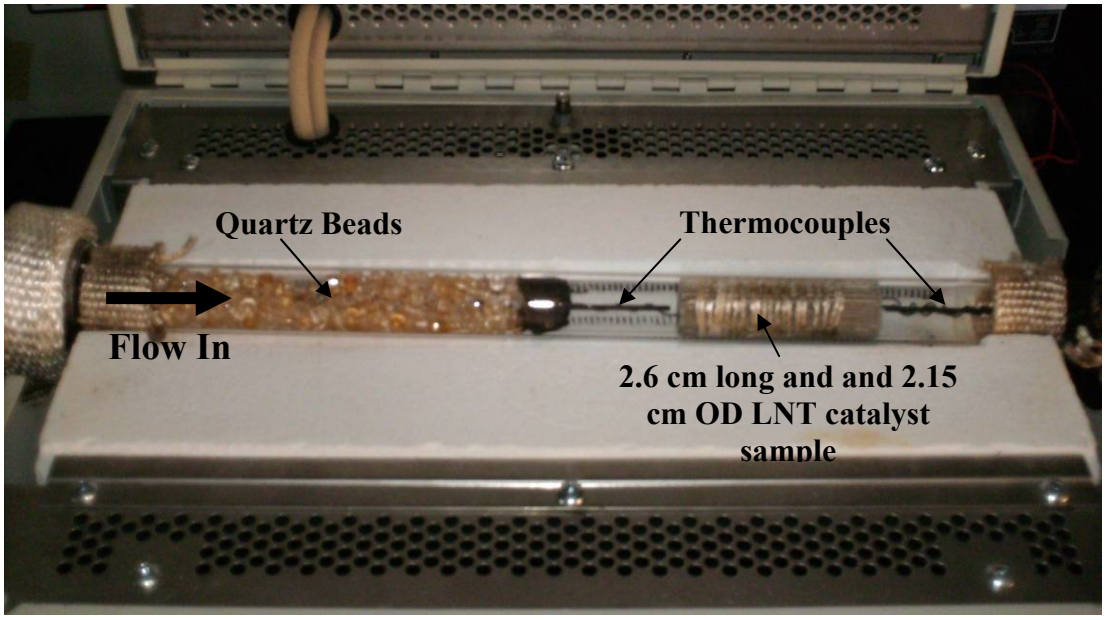

Figure 3.2.1 – Photograph of the LNT reactor

quartz beads with a diameter of 5 mm. Figure 3.2.1 is a photograph of the LNT reactor. Stainless steel fittings which compress graphite ferrels around the ends of the tube are used to couple the quartz tube to the rest of the bench-flow system. The fittings are constructed by welding three small Swagelok fittings to a 2.54 cm Swagelok end cap. The smaller fittings are used to connect the gas line and also serve as thermocouple wells.

3.2.2 - Thermocouples

Six Omega Type-K thermocouples are used to measure the temperatures at various locations inside the catalyst. Figure 3.2.2 shows the positions of the thermocouples. There is one thermocouple 5 mm from the inlet, one 5 mm downstream from the exit, and four within the catalyst. Because the thermal aging simulated in this

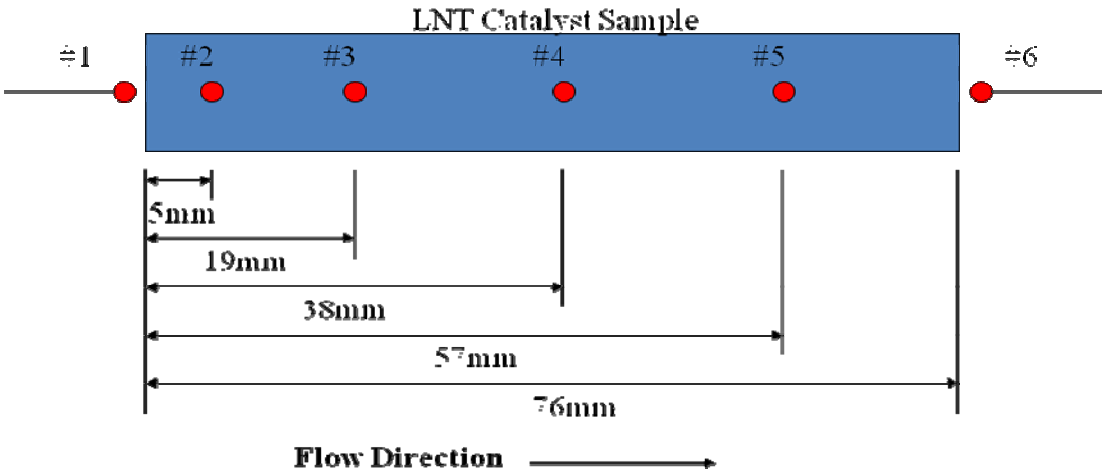

Figure 3.2.2 – Positions of thermocouples

study is cyclic and not hydrothermal, different sections of the catalyst are aged at different temperatures. In other words, in an aging experiment in which the front of the catalyst experiences an aging temperature of 1070^{o}C, the rear of the catalyst may only be aged at 950^{o}C. Consequently, the front half of the catalyst is more severely aged than the rear half of the catalyst. With temperature variation across the catalyst during aging, the effect of aging temperature on surface morphology can also be investigated. When surface studies are performed on the catalysts, the catalysts are sectioned at the locations where the thermocouples are positioned since the aging temperature of that section is known.

3.3 – Components of the Bench-Flow Reactor

3.3.1 – Mass Flow Controllers

Mass flow controllers (MFCs) are used to precisely control the amount of each gas flowing. The MFCs are split up into three groups: the main bank (which continuously goes through the BFR), the lean bank (those which go through the BFR during the lean phase), and the rich bank (those which go through the BFR during the rich phase). Because MFCs are originally calibrated with N_2, a K factor is used when flowing a gas other than N_2. All MFCs are controlled by a 0-5V input signal from Labview®. A 0-5V feedback signal is also monitored with Labview to ensure proper flow. Table 3.2 lists the MFCs, which bank they are in, their volumetric flow rate, K factor, and manufacturer.

Table 3.2 – Mass flow controller ranges and K factors

Main Bank	Volumetric Flow Rate (L/min)	K Factor	Manufacturer
N_2	0-4	1.000	Unit
CO_2	0-4	0.737	Unit
NO_x	0-.35	0.976	Tylan
Lean Bank			
Air	0-5	1.006	Omega
N_2	0-10	1.000	Omega
Rich Bank			
CO	0-10	1.000	Mks
H_2	0-2	1.010	Mks
N_2	0-10	1.000	Tylan
O_2	0-5	0.992	Hastings

3.3.2 – Pressure Transducers

Two Cole Parmer® pressure transducers (Model 07356-50) with a range of 15 psig are located before and after the catalyst in order to monitor the pressure drop across the catalyst and the system backpressure. The pressure transducer before the catalyst is also used to ensure constant pressure when switching from the lean to the rich bank, and vice versa.

3.3.3 – Tubing and Heat Tapes

Stainless steel tubing, 0.64 cm inner diameter, and stainless steel Swagelok fittings are used to connect all the components of the BFR system. The gas lines coming out of the instrument cart are heated with heat tapes controlled by variable voltage transformers. The gas coming into the steam generator is heated above 200^{o}C to avoid water pulsation from the steam generator. Water pulsation was an issue at the lowest aging temperature, and could be easily identified by small, periodic temperature excursions.

The line from the steam generator to the LNT reactor is heated by a high temperature Omega® heat tape (STH101-040) controlled by a programmable temperature controller. The temperature of this line is changed depending on the evaluation temperature. Swagelok VCR-type connectors are used to connect the LNT reactor to the BFR system. These connectors use graphite gasket fittings, which are easily disassembled even after exposing to high temperatures. The lines from the outlet of the reactor to the condenser are all heated above 100^{o}C to prevent condensation of the steam.

3.3.4 – Lean/Rich Switching Valves

Two Peter Paul Electronics® 3-way valves, S1 and S2, are used to control the lean and rich bank gases. The valves, model number 76Z00040GV, have a maximum pressure differential of 60 psi. The rapid actuation of these valves minimizes mixing of the lean and rich bank gases during switching. During the lean cycle, S1 sends the flow from the lean bank to the BFR and S2 sends the flow from the rich bank to exhaust. During the rich cycle, S2 sends the flow from the rich bank to the BFR and S1 sends the flow from the lean bank to exhaust.

3.3.5 – Bypass Line

The heated bypass line is used to check gas concentrations before and after each experiment. Three high-temperature Swagelok valves and three Newport Corporation® pneumatic high-temperature valves (Model 150) control the flow of gases to the reactors and the bypass. There is a valve at the inlet and exit of the LNT reactor and the bypass. When a test on the LNT reactor is run, all the valves are shut except the valves at the inlet and exit of the SCR reactor. To check the gas concentrations, both LNT valves are shut, and the two bypass valves are opened.

3.3.6 – Steam Generator and Peristaltic Pump

A Cole Parmer Masterflex™ peristaltic pump is used to supply liquid water to the steam generator. The pump has a range of 0.1 to 580 mL/min. The steam generator is constructed of a 1.26cm OD stainless steel tube placed inside a Lindberg/Blue M tube

furnace (TF55030A-1) maintained at 350˚C. Figures 3.3.1 and 3.3.2 are, respectively, a picture of the water pump and the steam generator. The front 1.5-cm of the stainless steel tube is packed with quartz wool while the rest is filled with glass beads. The tube is connected to a Swagelok union tee type fitting. One end of the fitting is connected to a 0.64-cm OD heated line of the inert carrier gases (N_2 and CO_2); the other to a bored 0.16-cm Swagelok fitting. A 0.16-cm OD stainless steel tube is inserted through the bored Swagelok fitting with and its end is buried inside the quartz wool. The other end is connected to the PVC tubing with liquid water from the water pump. Liquid water is injected by the pump, absorbed onto the quartz wool, evaporated, and is swept away by the carrier gases.

3.3.7 –NO_x Analyzers and Ammonia Trap

Two gas analyzers are used to measure the concentration of NO and NO_2 in the exhaust stream. A Horiba Model CLA-220 analyzer is used to measure NO, and a California Analytical Instruments (CAI) Model 400-HCLD analyzer is used to measure NO_x. Figure 3.3.3 is a photograph of the two NO_x analyzers used in this study. \

Both analyzers employ the chemiluminescent method of detection. The Horiba analyzer uses silicon photodiodes to detect photons emitted when NO reacts with ozone (O_3) to produce NO_2 and O_2. The amount of light emitted is directly proportional to the concentration of NO in the gas stream. The CAI analyzer is a heated chemiluminescent analyzer, in which an internal oven maintains all components in contact with the sample gas above 60^{o}C.

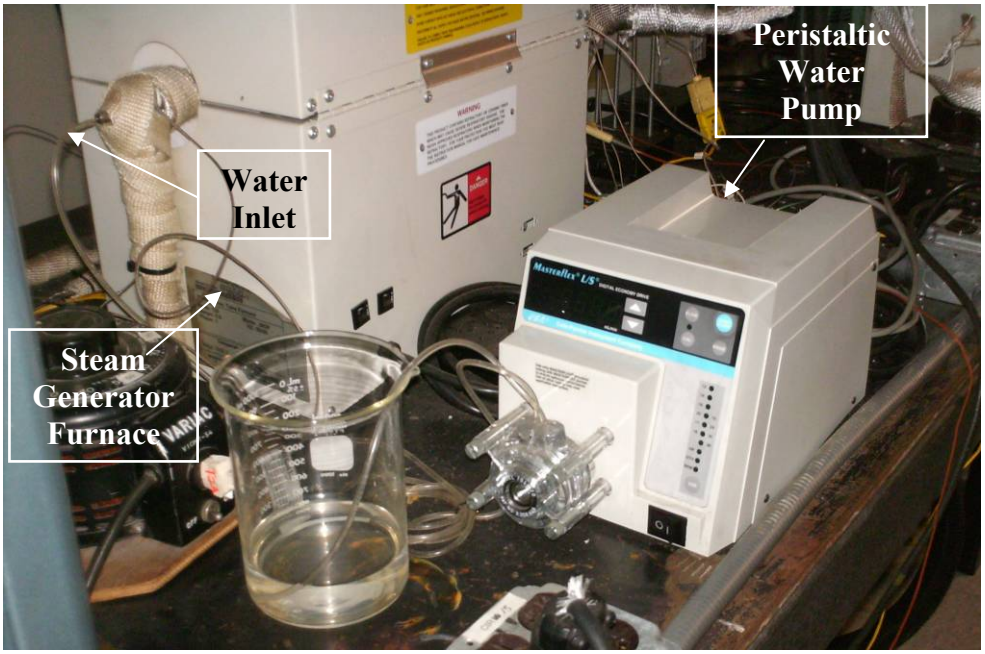

Figure 3.3.1 – Peristaltic water pump

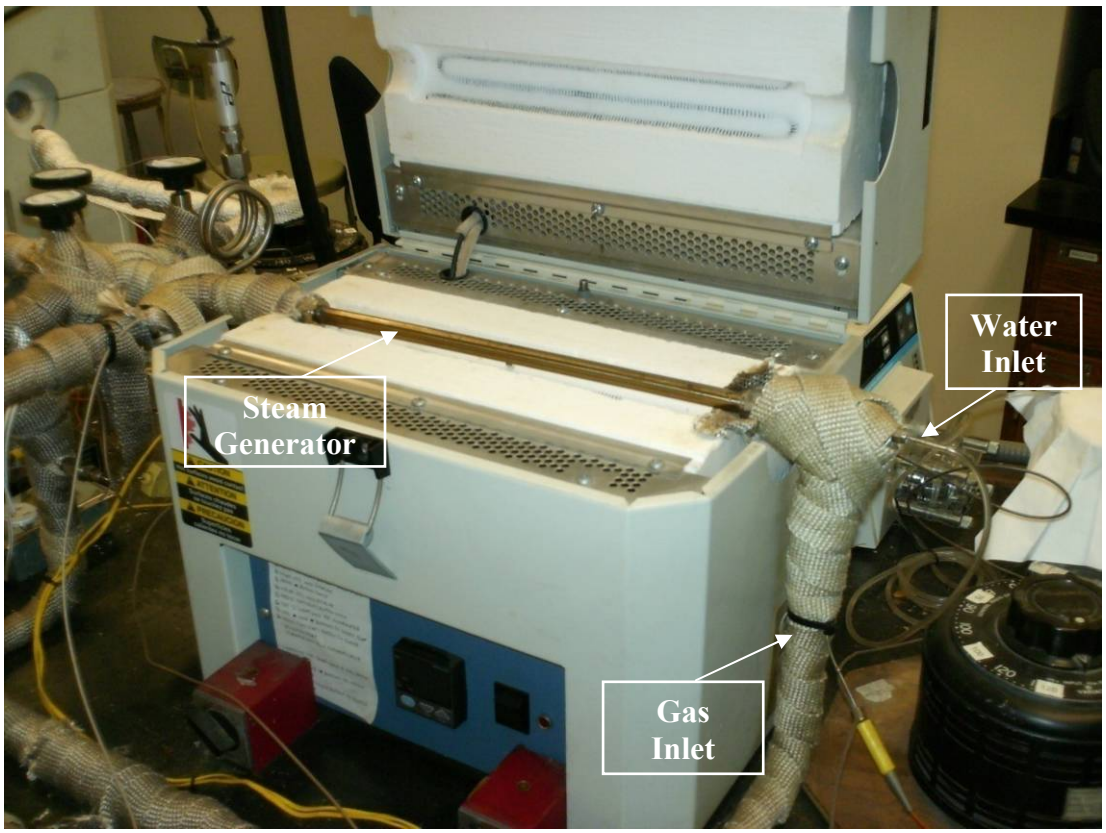

Figure 3.3.2 – Steam generator assembly

Figure 3.3.3 – Horiba NO_x analyzer (top) and California Analytical Instruments NO_x analyzer (bottom)

A Perma Pure AS-200-8-EB ammonia trap heated by a Watlow® jacket heater is installed upstream of the analyzers because high ammonia concentrations (>10 ppm) can reduce the efficiency of the NO_2 to NO conversion in the analyzers. The ammonia scrubbing media is replaced once a month.

3.3.8 – Data Acquisition System

National Instruments® (NI) hardware and software serve as the data acquisition system. A Dell® Precision 350 computer runs a graphic user interface built in Labview 8.2. The Labview virtual instrument (vi) is used to control the MFCs and the lean/rich switching valves. The raw data from the analyzers, the thermocouples, the pressure transducers, and the MFCs are also processed by the data acquisition system and saved as

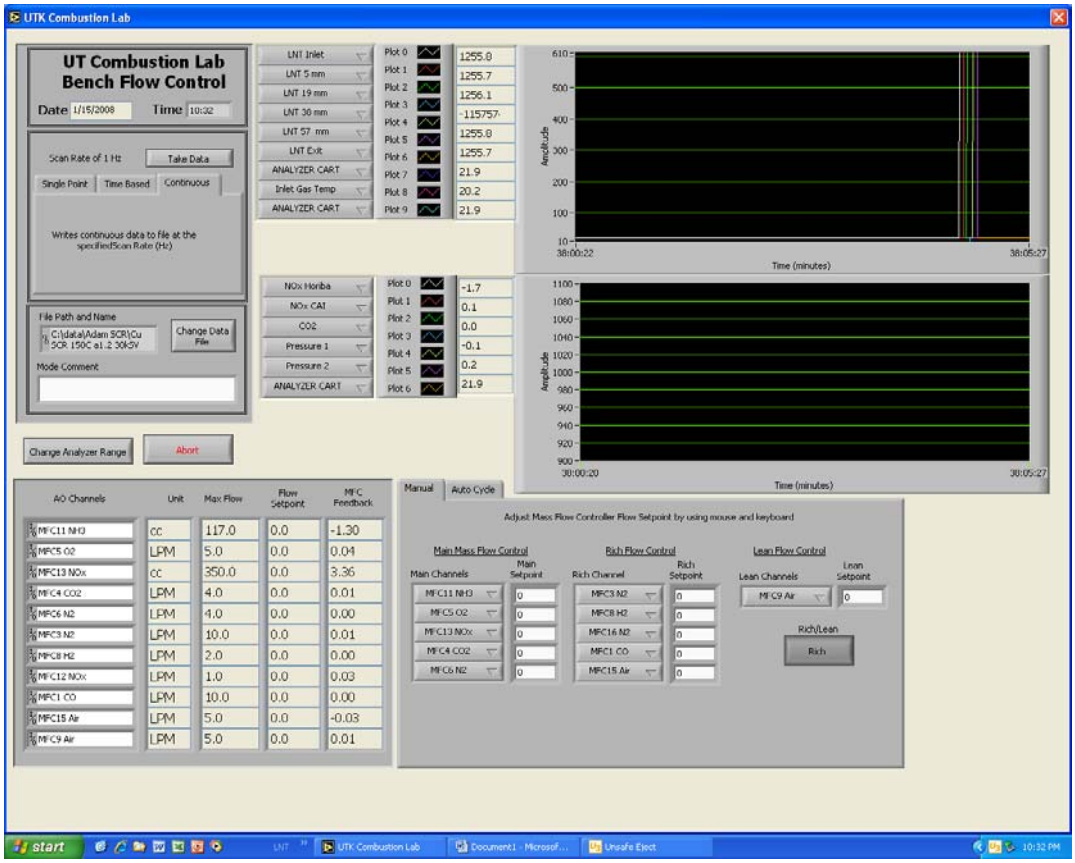

Figure 3.3.4 – Data acquisition system user interface

a text file. The raw data are collected by a 31-channel NI TC 2095 thermocouple receptor and a NI BNC 2090. Figure 3.3.4 is a photograph of the DAQ user interface.

3.4 – Experimental Procedure

3.4.1 – Startup Procedure

Prior to each experiment the same startup procedure is used. The heat tapes, the reactor furnace, and the steam generator furnace are all turned on and allowed to come to temperature. While the system is heating up, the analyzers are calibrated using 1000 ppm

NO in a balance of 99.999% ultra high purity (UHP) N_2 with a mixture uncertainty of +/- 2%. Two valves on top of the analyzer cart control the flow of gases to the cart. The cart is either connected to the gases coming from the bench-flow reactor or to the calibration gases.

Once the analyzers have been calibrated, the analyzer cart is connected to the BFR. The cart is turned on, and a small flow of N_2 (approximately 1 L/min) is introduced to the reactor through the main bank. The vacuum pump, an Air Dimensions Incorporated® DIA-VAC™ powered by a GE 1/3 hp motor, is turned on, and the flow rate of N_2 is increased until the desired flow rate is reached. At this point, the N_2 flow is maintained until the catalyst has reached the operating temperature and the temperature gradient across the catalyst is small (less than 7^oC). The temperature of the LNT reactor and the inlet heat tape are adjusted until there is approximately no temperature differential across the catalyst. H_2O is then introduced via the steam generator, and Air is then added to the lean bank. The lean bank gases are flowing through the reactor at this point.

Any residual NO_x left on the catalyst is "cleaned" before performing the experiment. The rich bank gases are switched on and are flowed through the reactor until the NO_x analyzers no longer detect any NO_x coming from the catalyst. The lean gases are once again sent to the reactor and continue to flow until the temperatures reach steady state. Once temperatures are steady, data acquisition is begun and cycling is started.

3.4.2 – Evaluation of LNTs

Fresh and aged LNTs are evaluated at three different temperatures: 200, 300, and 400°C at a gas hourly space velocity (GHSV) of 30,000 h^{-1}. The calculation of the space velocity is shown below in Equation 3.1, where α=.6 is the correction factor for the LNTs wall volume.

$$GHSV(h^{-1}) = \frac{(L/\min)(61.02in^3/L)(60\min/h)}{\alpha * V_{catalyst}} \qquad (3.1)$$

The same flow rates are used for all three temperatures. Table 3.3 lists the flow rates used in the lean and rich flows and Table 3.4 lists the gases used and their purities. Evaluations are performed using an evaluation cycle consisting of a 60 second lean phase and a 5 second rich phase. Evaluation experiments are run until steady state cycle-to-cycle average NO_x conversion is achieved.

Table 3.3 – Composition of simulated exhaust gases used for evaluation (GHSV = 30,000 h^{-1})

	Lean (60s)	**Rich (5s)**
NO_x, ppm	300	300
CO_2, %	5	5
CO, %	0	1.13
H_2, %	0	0.68
Air, %	10	0
H_20, %	5	5
N_2	Balance	balance

Table 3.4 – Purities of gases used for evaluation and aging experiments

Gas	Composition	Purity
O_2 (Eval.)	21% O_2 / N_2 bal.	Research
O_2 (Aging)	100%	UHP
CO_2	100%	Research
NO	1% NO / N_2 bal.	UHP
CO	20% CO / N_2 bal.	Research
H_2	40% H_2 / N_2 bal.	Research
N_2	100%	UHP

3.4.3 – Aging of LNTs

LNTs are aged at four different temperatures: 700, 800, 900, and 1000°C. Tables 3.5 to 3.8 list the gas concentrations used in the lean and rich flows for aging temperatures of 700, 800, 900, and 1000°C, respectively. The gas concentrations are determined experimentally on a catalyst sample. Different space velocities are used at different aging temperatures in order to minimize the temperature differential across the LNT. Lower GHSVs of 50,000 h^{-1} and 54,000 h^{-1} are used at 700°C and 800°C, respectively, while a higher GHSV of 57,000 h^{-1} is used when aging at 900 to 1000°C in order to enhance the convection heat transfer to the rear-half of the LNT. Aging experiment cycles consist of a 130 s lean phase and a 50 s rich phase and are performed for a set number of cycles: 5, 25, 50, 100, 150, and 200 cycles at 700 and 800°C; 5, 25, 50, 100, 150, 200, and 300 cycles at 900°C; and 5, 25, 50, 100, 150, 200, and 350 cycles at 1000°C. Evaluations of the NO_x conversion are carried out after each aging experiment.

Table 3.5 – Gas compositions of lean and rich phases used for aging at 700°C (GHSV = 50,000 h^{-1})

	Lean (130s)	**Rich (50s)**
NO_x, ppm	300	300
CO_2, %	6	6
CO, %	0	4.2
H_2, %	0	1.25
O_2, %	12	3.5
H_20, %	4.5	4.5
N_2	balance	balance

Table 3.6 – Gas compositions of lean and rich phases used for Aging at 800°C (GHSV = 54,000 h^{-1})

	Lean (130s)	Rich (50s)
NO_x, ppm	300	300
CO_2, %	6	6
CO, %	0	4.5
H_2, %	0	2.5
O_2, %	12	3.5
H_20, %	4.75	4.75
N_2	Balance	balance

Table 3.7 – Gas compositions of lean and rich phases used for Aging at 900°C (GHSV = 57,000 h^{-1})

	Lean (130s)	Rich (50s)
NO_x, ppm	300	300
CO_2, %	5	5
CO, %	0	5.1
H_2, %	0	3.25
O_2, %	11	4
H_20, %	4.2	4.2
N_2	Balance	balance

Table 3.8 – Gas compositions of lean and rich phases used for Aging at 1000°C (GHSV = 57,000 h^{-1})

	Lean (130s)	Rich (50s)
NO_x, ppm	300	300
CO_2, %	5	5
CO, %	0	5.9
H_2, %	0	4.55
O_2, %	11	5
H_20, %	4.2	4.2
N_2	Balance	balance

3.5 – Surface Characterization Techniques

3.5.1 – Powder X-ray Diffraction

Powder X-ray diffraction (P-XRD) is one of a group of non-destructive techniques that are used to extract information about the crystallographic structure, chemical composition, and physical properties of a sample. In a typical P-XRD, a powder sample is bombarded by X-rays from an X-ray tube. The X-rays are scattered by the sample, and the intensity of the scattered X-rays is measured by a flat plate detector. A diffractogram is created by plotting the intensity of the reflected radiation against the scattering angle of the radiation, 2θ. The X-ray emitter and detector simultaneously rotate through the chosen range where the peaks of interest are located.

P-XRD measurements are based on the principles of Bragg diffraction. William Lawrence Bragg and his son discovered that crystalline structures, when bombarded by radiation of a certain wavelength and at a certain incident angle, create intense peaks of reflected radiation. This phenomenon led to Bragg's Law, shown in Equation 3.2,

$$2 * d * \sin(\theta) = n * \lambda \qquad (3.2)$$

Where d is the distance between atomic layers in the crystal, θ is the angle of incidence, and λ is the wavelength of the incident X-ray beam. Because every compound has a unique amount of space between atomic layers, d, the diffractogram for each compound is distinct and serves as a fingerprint by which the compound can be identified. However, several compounds have very similar d-spacings which can create peak overlap and make analysis difficult. The Scherrer equation shown in Equation 3.3, is used to calculate average crystallite size from P-XRD data [ff].

$$d_v = K\lambda / \beta\cos(\theta) \qquad (3.3)$$

The average crystal size is represented by d_v. K is the Scherrer constant, a value that falls between 0.87 and 1 and is assumed to be 1 in the present study. Lambda, λ, is the wavelength of the X-ray radiation. Beta, β, is defined as the line broadening of a particular peak, and is calculated with Equation 3.4 where b is the line broadening due to the diffractometer and FWHM is the full width half maximum defined in degrees (2θ). In this study, the line broadening due to the diffractometer is calculated with respect to a LaB_6 sample.

$$\beta = \sqrt{(FWHM(\frac{\pi}{180}))^2 - b^2} \qquad (3.4)$$

The PANalytical® X'Pert PRO instrument is located at Oak Ridge National Laboratory's (ORNL) High Temperature Materials Laboratory. The machine has a spinning sample stage, which eliminates any effects of texturing, i.e., the crystallographic orientations are completely random. The anode used to generate X-rays is copper, and the samples are placed on a zero background tray to ensure that the reflected radiation is not a result of the sample stage. Prior to analysis, samples are pretreated overnight at 250°C in a 100 sccm flow consisting of 5% CO_2 in Ar in order to drive all Ba phases to $BaCO_3$. Acetone is used to disperse the sample and also to hold the sample to the zero background tray during transportation to the machine. The tube voltage and current used are 45kV and 40 mA, respectively. Scans are performed from $2\theta = 15^o$ to 85^o, with a 0.017^o step size. Figure 3.5.1 is a photograph of the P-XRD instrument used in the study.

Figure 3.5.1 – Photograph of X-ray diffraction instrument used at ORNL

3.5.2 – Scanning Transmission Electron Microscopy/Scanning Electron Microscopy/Energy Dispersive Spectroscopy

Scanning transmission Electron Microscopy (TEM) is used to determine growth in Pt particle size as a result of thermal aging. TEM instruments generate a beam of electrons which is focused by electromagnetic lenses into a fine beam and then directed at an ultra-thin sample. As the beam passes through the sample, some of the electrons are scattered by the sample, while others transmit through the sample and hit a fluorescent screen. The image formed by the received electrons is then either digitized or captured with a camera for analysis.

The TEM instrument used in this study, a Hitachi HF-3300 cold FE-STEM/TEM, is equipped with a cold field emission electron source which aids nanoscale analysis with its high energy resolution and high brightness. The TEM instrument is also equipped with an energy dispersive X-ray spectrometer (EDS) and a scanning electron microscope (SEM). Energy dispersive X-ray spectroscopy is a technique used for the elemental analysis of a sample. The spectrometer analyzes X-rays emitted by high-energy outer shell electrons moving to fill low-energy inner shell electron holes created by the electron beam. The specific X-rays released are characteristic of the atomic structure of the element from which they are released. Scanning electron microscopy is a method of determining the morphological properties of a sample by scanning the sample with a beam of electrons in a raster scan pattern. The Hitachi HF 3300 instrument used in this is shown in Figure 3.5.2. It is located in the High Temperature Materials Laboratory (HTML) at the Oak Ridge National Laboratory (ORNL).

Figure 3.5.2 – Picture of Hitachi HF 3300 TEM instrument used in this study

3.5.3 – Electron Probe Microanalysis

Electron Probe Microanalysis (EPMA) is used to determine the chemical composition of a sample as well as to map the physical location of selected components of the sample. The sample is bombarded by an intense electron beam, which upon contacting the surface of the sample, energizes electrons to a higher unstable energy level. The X-ray radiation emitted when these electrons return to a more stable energy level as well as the electrons that are dislocated from the sample are analyzed by detectors.

The EPMA instrument used in this study is shown in Figure 3.5.3. It is a Cameca Model SX-52, and it is located at the University of Tennessee's Science and Engineering Research Facility (SERF). A backscatter detector measures the intensities of the dislocated electrons and creates a qualitative plot of average atomic number. Washcoat cracking and delamination from the substrate are easily seen in the backscatter images. The X-ray radiation emitted by the excited electrons is analyzed by wavelength dispersive spectrometers in order to plot line scans and element maps. A line scan is a plot of the concentration of selected elements versus position. The excitation area at each point scanned is approximately 3 μm, and scans were taken every 3 μm along the chosen path. A typical line scan is approximately 130 μm in length and consists of 43 scans. The elements scanned for in this study are: Ba, Pt, Zr, Ce, Mg, La, Si, and Al. Line scans determine the distribution of elements within the washcoat. Elemental maps are qualitative maps which show the location and the concentration of a single element on the catalyst surface. Elemental maps are collected for Ba, Ce, and Pt. Line scans and elemental maps are used to check for particle migration or agglomeration as a result of aging.

Figure 3.5.3 – Cameca EPMA Hardware

Correct sample preparation is a very important part of EPMA. Because the sample is assumed to have no texture, everything possible is done to make a smooth, flat scan surface. Samples are placed in circular plastic holders and held in place with low viscosity epoxy. A vacuum pump is used to force the epoxy into the micropores of the washcoat. The top 1 mm of the sample is then cut off using a diamond saw and the resulting surface is sanded and polished to a 1 μm finish.

3.5.4 – BET Surface Area Analysis

BET, named after Stephen Brunauer, Paul Hugh Emmett, and Edward Teller, the researchers who published the first article on the subject, is used to determine the surface area of a porous media [59]. BET theory is based on the Langmuir equation and the principles of monolayer and multilayer adsorption. The Langmuir equation shown in Equation 3.5, relates the adsorption of particles onto a surface to the concentration of the adsorbate particles, their strength of adsorption, and the temperature of the environment.

$$\theta = \frac{\alpha * P}{1 + \alpha * P} \tag{3.5}$$

In Equation 3.5, θ is the percentage of the surface covered by the adsorbate, P is the gas pressure or concentration, and α is the Langmuir adsorption constant.

In a multipoint BET analysis used in the present study, an adsorption isotherm, the BET plot, is used to determine the volume of an adsorbate gas adsorbed at standard temperature and pressure (STP) at monolayer coverage, v_m, and the BET constant, C. The BET plot is constructed by plotting the left hand side of Equation 3.6, the BET equation, vs. P/P_o. In Equation 3.6, P is the partial pressure of the adsorbate gas, P_o is the saturation vapor pressure of the adsorbate gas, V is the total volume adsorbed at pressure P, and C has been approximated in Equation 3.7, where q_1 and q_L are the heats of adsorption in the first and succeeding monolayers, respectively. From the BET plot, the slope equals $(C-1)/v_mC$, and since C, which is always positive, is much greater than one for both N_2 and Ar, the slope may be approximated as $1/v_m$. Once v_m has been determined, the total surface area can then be easily calculated with Equation 3.8 using Avogadro's number, N, the cross sectional area of the adsorbate gas, s, and the molar volume of adsorbed gas, v_m [60].

$$\frac{P/P_0}{V(1-P/P_0} = \frac{(C-1)}{v_m C}(P/P_0) + \frac{1}{v_m C} \tag{3.6}$$

$$C = e^{(q1-qL)/RT} \tag{3.7}$$

$$A = \frac{v_m N}{s} \tag{3.8}$$

The current setup, located at NTRC, utilizes a Stanford Research Systems® residual gas analyzer to measure concentration of Ar. A schematic of the microreactor/mass spectrometer system is shown in Figure 3.5.4. A mixture of 100 cc of Ar and He is continuously flowed, and the Ar concentrations used are 1.5, 2.5, 3.5, 4.5, 5.5, 6.5, and 7.5%. These concentrations are chosen because they fit within the BET preferred range for best results of $0.05 < P/P_o < 0.4$. Ar is chosen as the adsorbate gas because its melting point of -189°C is higher than the temperature of liquid nitrogen of -196°C, which means that it will physisorb to the LNT surface when submerged in liquid nitrogen. Ar is used rather than N_2 because it has a smaller cross-sectional area of 0.138 nm^2 as compared to 0.162 nm^2 for N_2 and is thus expected to better cover the surface. Also, the m = 28 mass spectrometer trace of N_2 is the same as that for CO, a gas that is commonly analyzed in the microreactor used for BET experiments. Thus, since it is not easy to purge lines of N_2, it is best if it is never introduced into the system. Helium is chosen as the carrier gas because its melting point of -272°C ensures that it remains in the gas phase even when the sample is submerged in liquid nitrogen. Ten-minute experiments are run at each Ar concentration. The first minute, with the sample at room temperature, is used to calibrate the mass spectrometer (MS). At the beginning of the second minute, the sample is submerged in a liquid nitrogen bath and Ar adsorbs on the sample. After four minutes of adsorption, by which time the surface of the sample is equilibrated, the liquid nitrogen bath is removed and the sample is submerged in a dewar of room temperature (20°C) water. The adsorbed Ar desorbs and the test is allowed to run until the 10-minute mark. The same test is run at seven different concentrations of Ar in order to construct an adsorption isotherm from which v_m, the volume of adsorbate gas

adsorbed (STP) at monolayer coverage and the surface area can be determined as described above.

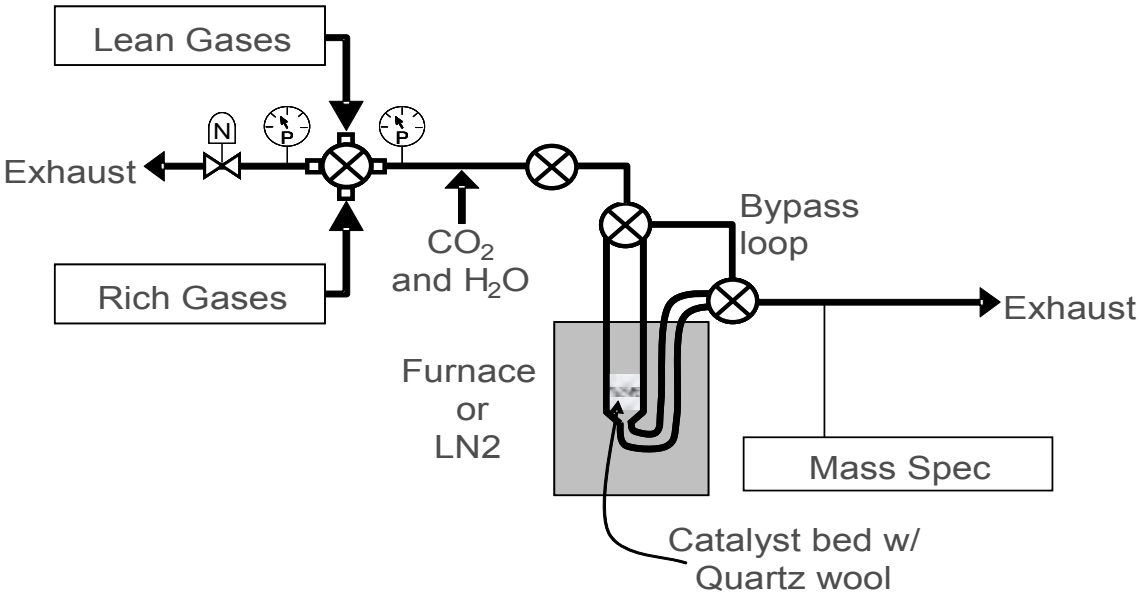

Figure 3.5.4 – Schematic of the microreactor/mass spectrometer system used to measure BET surface area

Chapter 4

RESULTS AND DISCUSSION

The determination of the simulated exhaust gas composition used for the LNT evaluation experiments is explained in Section 4.1. Sections 4.2 and 4.3 describe the aging and evaluation experiments performed on the bench-flow reactor. Following this description is the discussion of the results from these NO_x conversion experiments in Section 4.4. Finally, in Section 4.3, the results of the surface characterizations performed on the fresh and aged LNTs are presented and discussed.

4.1 – Determination of Gas Concentrations used for Evaluation

The composition of simulated exhaust gases used during NO_x conversion performance evaluations follows the standards set forth by the DOE Cross-Cut Lean Exhaust Emissions Reduction Simulation (CLEERS) program. "CLEERS is a R&D focus group of the Diesel Cross-Cut Team whose overall objective is to promote development of improved computational tools for simulating realistic full-system performance of lean-burn engines and associated emissions control systems [58]."

CLEERS protocol for laboratory characterization of LNTs recommends a GHSV of 30,000 h^{-1}, a lean phase of 60s duration, and a rich phase of 5s duration. The composition of the simulated exhaust gases shown in Table 3.2, with the exception of the reductants used in the rich phase, is also outlined in the CLEERS protocol. Because the amounts of reductant necessary for catalyst regeneration depends on the specific catalyst

being tested, the CLEERS protocol only specifies that a 3:5 ratio of H_2 to CO be used. This particulatr ratio is obtained from Equations 4.1.1 and 4.1.2, which indicate that the stoichiometric amounts of H_2 and CO needed to react with one mole of $Ba(NO_3)_2$ are 3 and 5 moles, respectively. As mentioned in Chapter 2, it is conventionally assumed that the majority of the NO in the exhaust gases is stored on Ba sites in the form of nitrate.

$$Ba(NO_3)_2 + 3H_2 \rightarrow 3H_2O + BaO + N_2 + O_2 \qquad (4.1)$$

$$Ba(NO_3)_2 + 5CO \rightarrow 5CO_2 + BaO + N_2 \qquad (4.2)$$

The optimum concentration of reductants, referred to hereafter as the "sweetspot", is defined as the minimum concentration of reductants required to achieve 100% NO_x conversion when evaluating at the LNTs optimum operating temperature of 300^oC. Since the sweetspot is a function of the catalyst formulation, the evaluation temperature, and the gas hourly space velocity, the sweetspot has to be determined experimentally. Beginning with the stoichiometric amounts of H_2 and CO needed to reduce all the NO in the simulated diesel exhaust gases, the reductant concentration is increased until there is no NO_x detected at the exit of the LNT. Initially, when the stoichiometric reductant concentrations are used, NO_x breakthrough is immediate. Even with 1.5 and 1.9 times the stoichiometric amount of reductants, NO_x breakthrough is still substantial as can be seen in Figures 4.1.1 and 4.1.2. However, with twice the stoichiometric amount of reductants, i.e., 1.13% CO and 0.68% H_2, 100% NO_x conversion is finally achieved as shown in Figure 4.1.3.

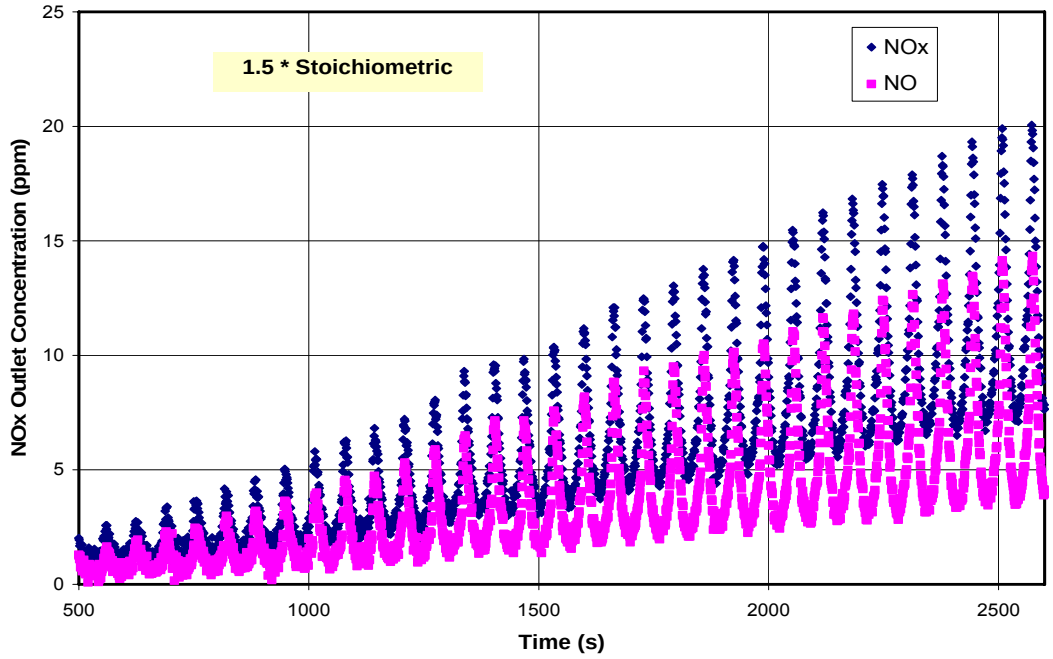

Figure 4.1.1 – Sweetspot determination of LNT catalyst at T=300°C and GHSV=30,000 h^{-1}. Lean: NO_x=300ppm, CO_2=5%, O_2=10%, H_20=5%, N_2=balance. Rich: NO_x=300ppm, CO_2=5%, H_20=5%, CO=0.84%, H_2=0.51%, N_2=balance

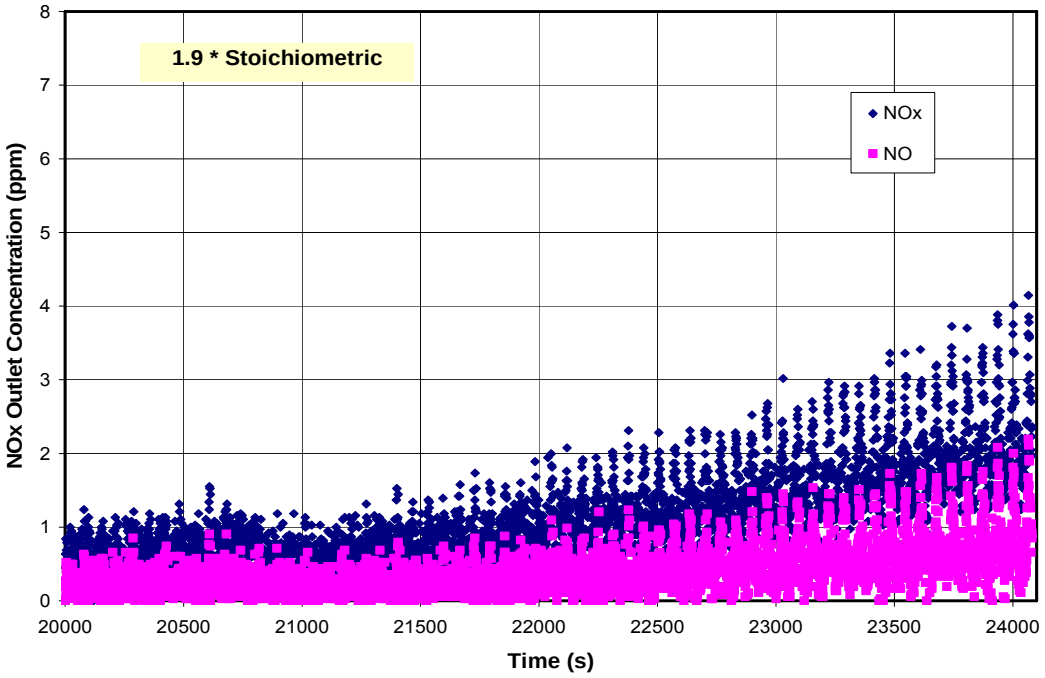

Figure 4.1.2 – Sweetspot determination of LNT catalyst at T=300°C and GHSV=30,000 h^{-1}. Lean: NO_x=300ppm, CO_2=5%, O_2=10%, H_20=5%, N_2=balance. Rich: NO_x=300ppm, CO_2=5%, H_20=5%, CO=1.07%, H_2=0.64%, N_2=balance

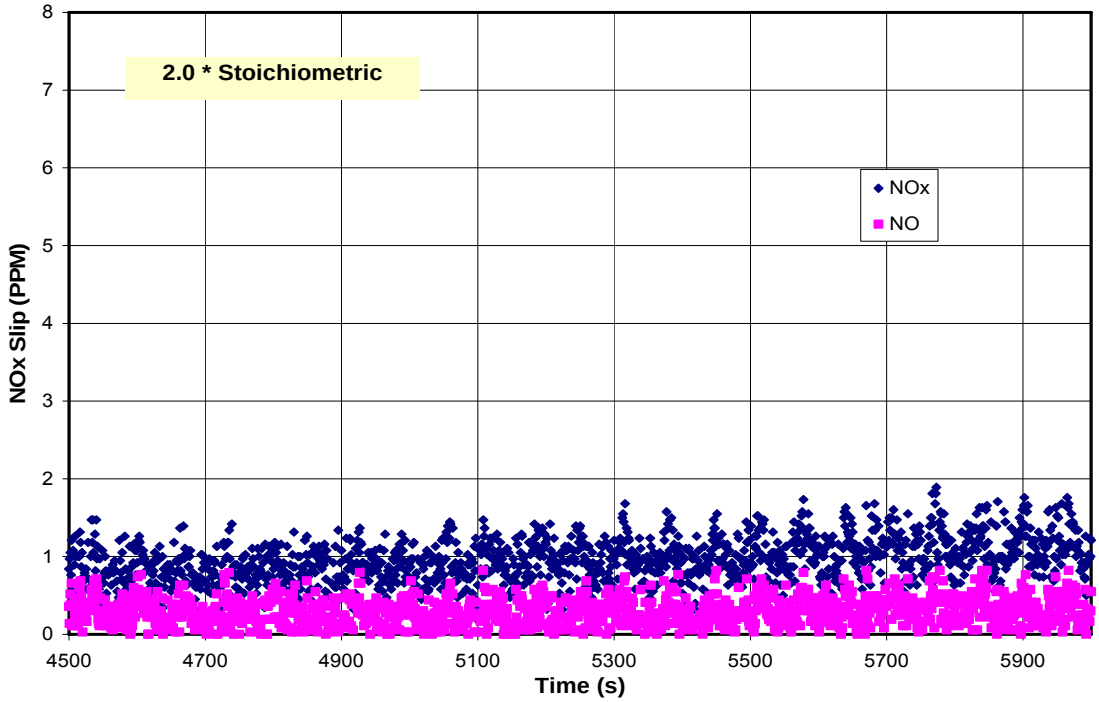

Figure 4.1.3 – Sweetspot determination of LNT catalyst at T=300°C and GHSV=30,000 h^{-1}. Lean: NO_x=300ppm, CO_2=5%, O_2=10%, H_20=5%, N_2=balance. Rich: NO_x=300ppm, CO_2=5%, H_20=5%, CO=1.13%, H_2=0.68%, N_2=balance

4.2 –Thermal Aging of LNTs

Thermal aging of LNTs is performed in order to simulate the periodic high-temperature de-sulfurization required as a result of sulfur poisoning of LNT catalysts. As discussed in detail in the introduction, the aging experiments performed in this study are cyclic, alternating between a lean and rich phase. Figures 4.2.1 to 4.2.8 show the temperature history at different locations in the LNT and the axial temperature profiles during thermal aging for the four aging temperatures of 700, 800, 900, and 1000°C. The temperature histories show the temperature at different locations for a single aging cycle, whereas the axial temperature profiles show the progression of the thermal front inside the catalyst during a single aging cycle.

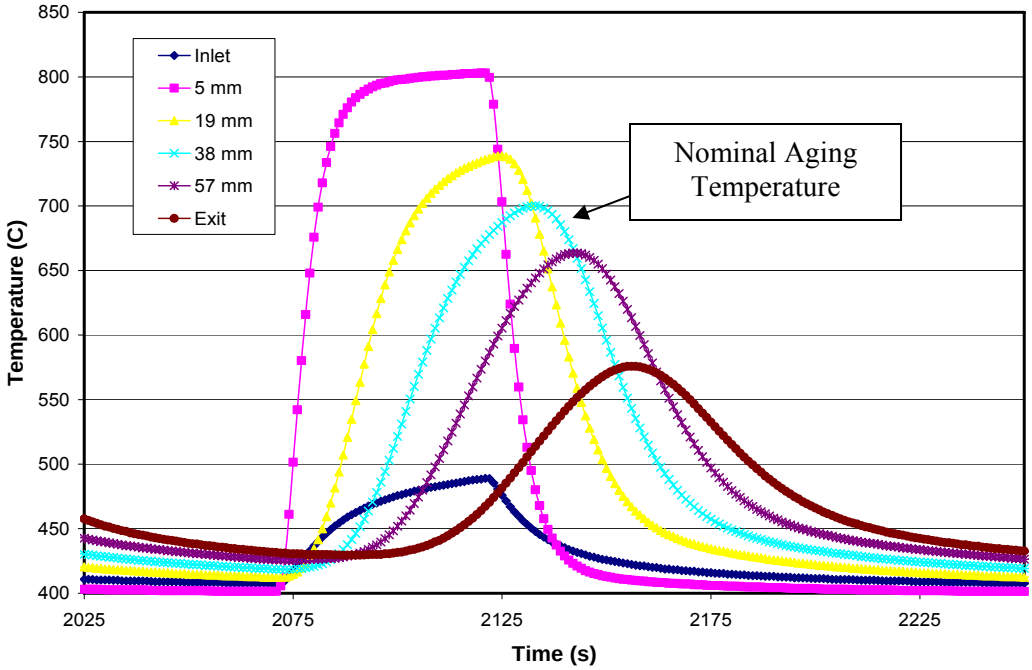

Figure 4.2.1 – Temperature history for LNTs aged at 700°C and GHSV=50,000 h^{-1}. Lean: NO_x=300ppm, CO_2=6%, O_2=12%, H_20=4.5%, N_2=balance. Rich: NO_x=300ppm, CO_2=6%, H_20=4.5%, O_2=3.5%, CO=4.2%, H_2=1.25%, N_2=balance

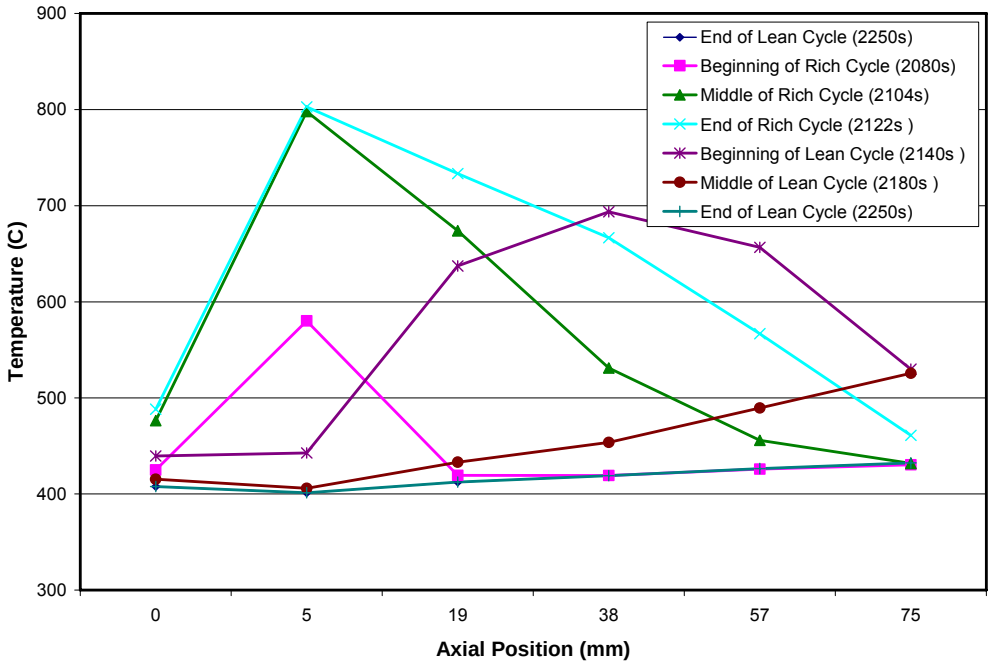

Figure 4.2.2 – Typical axial temperature profile at various times of one aging cycle for LNTs aged at 700°C

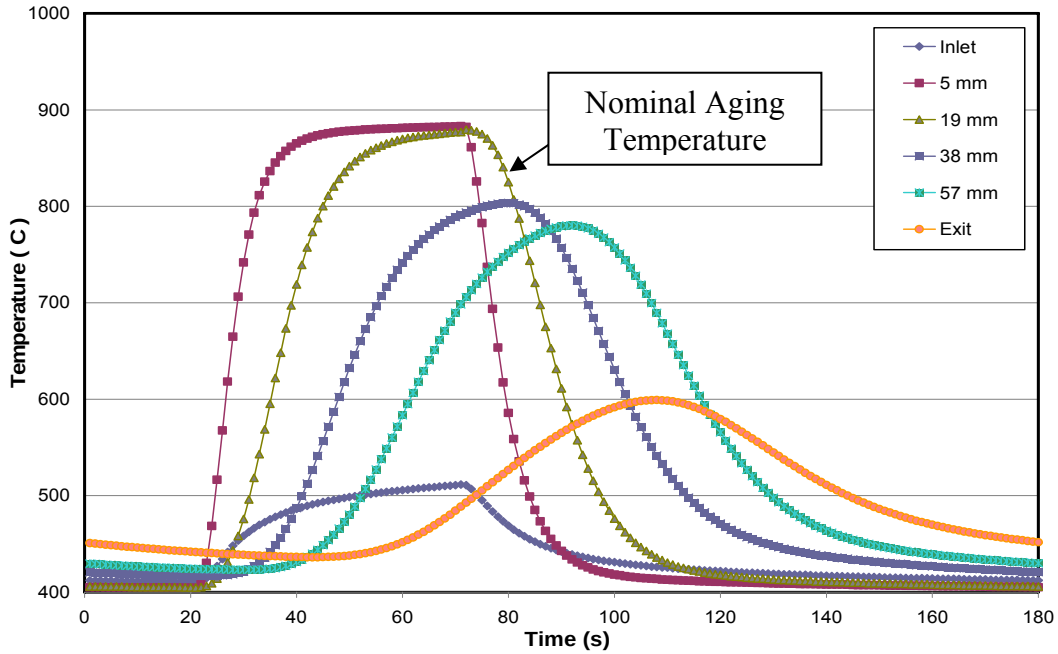

Figure 4.2.3 – Temperature history for LNTs aged at 800°C and GHSV=54,000 h^{-1}. Lean: NO_x=300ppm, CO_2=6%, O_2=12%, H_20=4.75%, N_2=balance. Rich: NO_x=300ppm, CO_2=6%, H_20=4.75%, O_2=3.5%, CO=4.5%, H_2=2.5%, N_2=balance

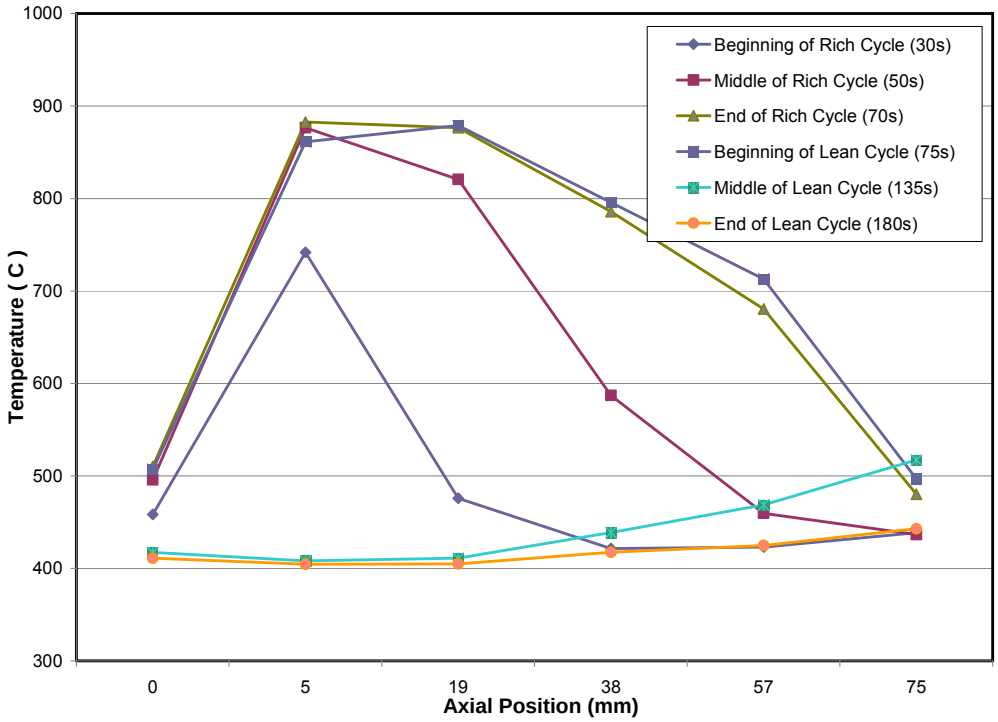

Figure 4.2.4 – Typical axial temperature profile at various times of one aging cycle for LNTs aged at 800°C

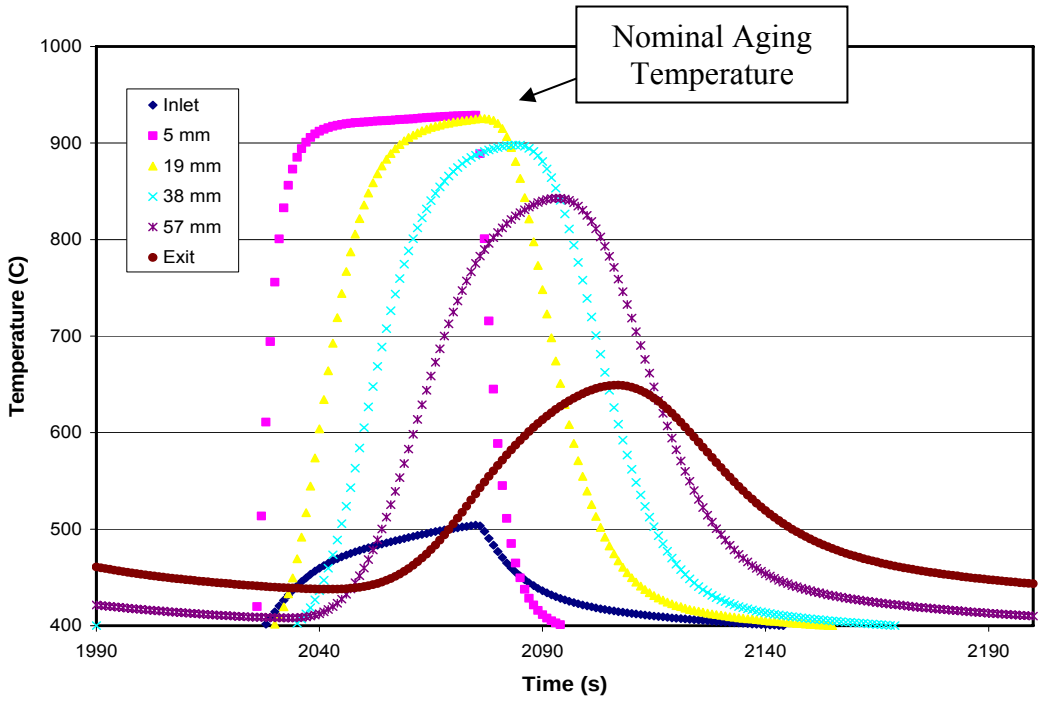

Figure 4.2.5 – Temperature history for LNTs aged at 900°C and GHSV=57,000 h^{-1}. Lean: NO_x=300ppm, CO_2=5%, O_2=11%, H_20=4.2%, N_2=balance. Rich: NO_x=300ppm, CO_2=5%, H_20=4.2%, O_2=4%, CO=5.1%, H_2=3.25%, N_2=balance

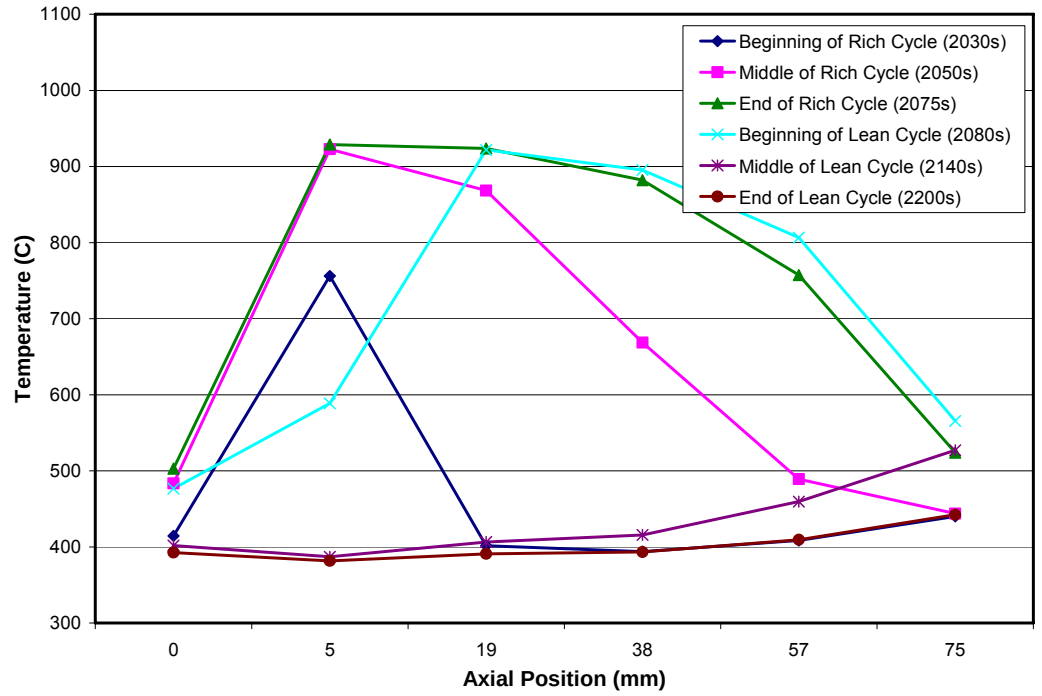

Figure 4.2.6 –Typical axial temperature profile at various times of one aging cycle for LNTs aged at 900°C

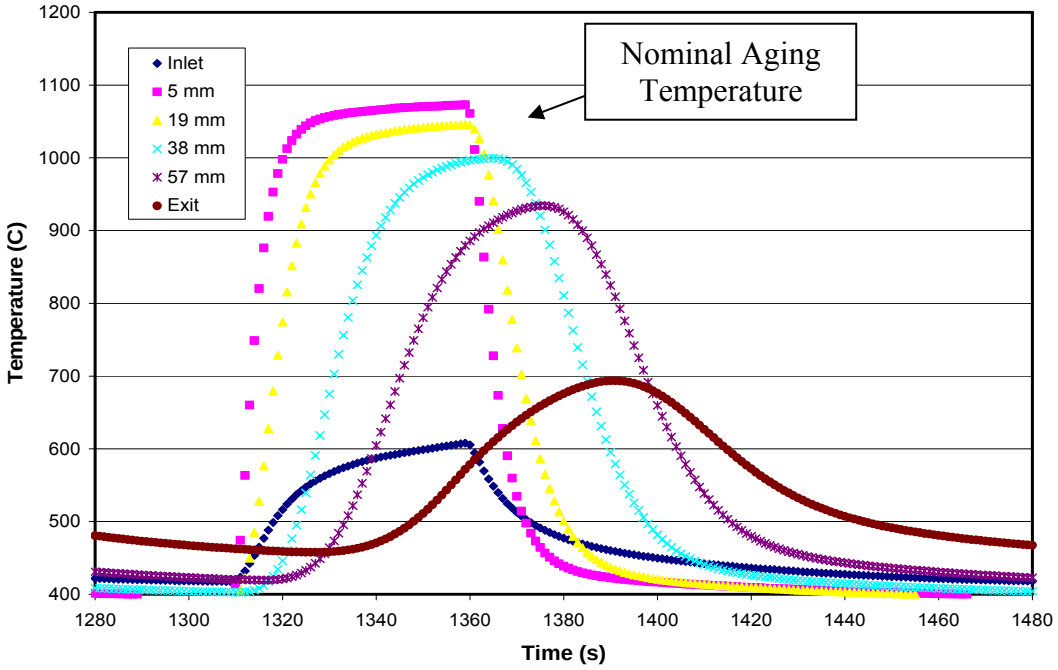

Figure 4.2.7 –Temperature history for LNTs aged at 1000°C and GHSV=57,000 h^{-1}. Lean: NO_x=300ppm, CO_2=5%, O_2=11%, H_20=4.2%, N_2=balance. Rich: NO_x=300ppm, CO_2=5%, H_20=4.2%, O_2=5%, CO=5.9%, H_2=4.55%, N_2=balance

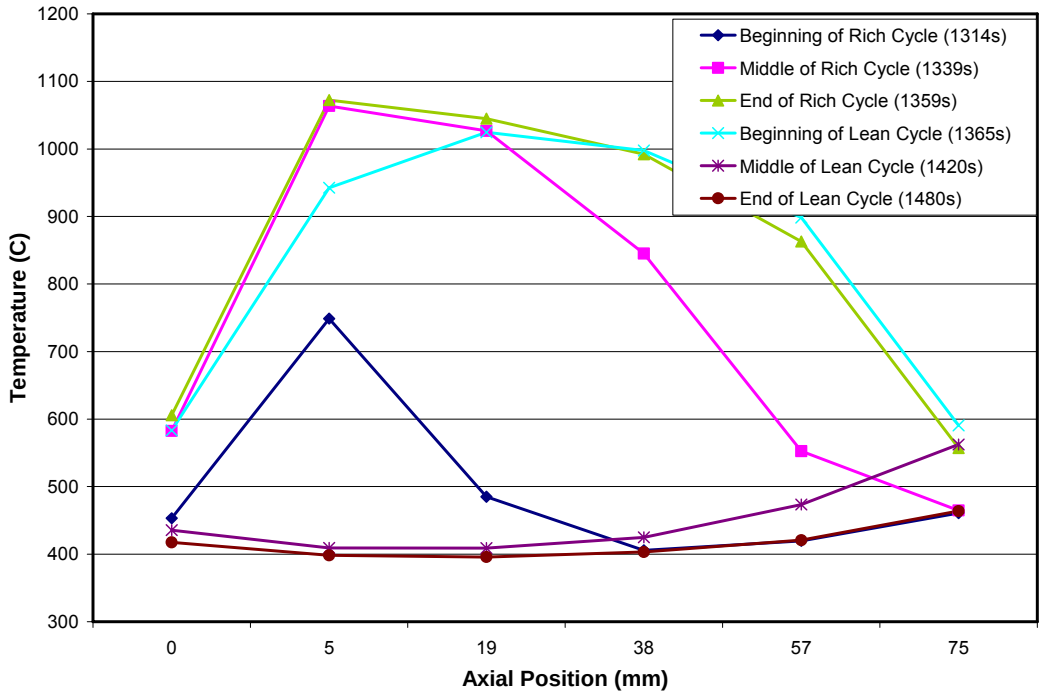

Figure 4.2.8 – Typical axial temperature profile at various times of one aging cycle for LNTs aged at 1000°C

Figure 4.2.2 shows the axial temperature profile for aging at 700°C. When the rich cycle begins at 2080 s, the temperature at a location 5 mm downstream from the LNT inlet begins to increase, while the rest of the catalyst remains at the furnace temperature of 400°C. At 2104 s, halfway through the rich cycle, the temperature at the 5 mm-location has reached its maximum of 800°C, whereas the temperature at the 19 mm-location is approximately 675°C, and the temperature within the remainder of the catalyst is beginning to increase. By the end of the rich cycle at 2122 s, the front of the catalyst is still at 800°C, while the 19 mm-location is now at its maximum temperature of 740°C, and the temperatures at the rear-half of the catalyst are still increasing. It is not until the beginning of the lean cycle at 2140 s, that the nominal aging temperature of 700°C is achieved at the mid-section of the LNT located 38 mm from the inlet, and the 57 mm-location reaches its maximum temperature of approximately 660°C. The temperatures inside the LNT continue to decrease for the remainder of the lean cycle, and toward the end of the cycle at 2250 s, the LNT's temperature is not much higher than the furnace temperature. From Figure 4.2.2 it is apparent that during aging the front-half of the LNT experiences much higher temperatures and consequently more severe degradation in NO_x performance than the rear-half of the LNT. The same general trend is observed in the axial temperature profiles at other nominal aging temperatures of 800°C, 900°C, and 1000°C.

The temperature histories and the axial temperature profiles can be used to ascertain the relative severity of aging at each of the four axial locations. The temperatures in the front half of the LNT, i.e., at 5, 19, and 38 mm from the inlet, are much higher than those in the rear-half because the majority of the reductants are

consumed in these locations. As a result, it is expected that the degradation in NO_x conversion will be more severe in the front-half of the LNT. On the other hand, the increase in temperature in the rear-half of the LNT is mainly due to the convection of hot gases generated by the exothermic oxidation reactions between the reductants and oxygen in the front-half of the LNT. Because the majority of the reductants are consumed in the front-half of the LNT, the temperatures in the rear-half are much lower than those in the front-half. As can be seen in Figure 4.2.1, the temperature at a location of 57 mm from the LNT's inlet never reaches the nominal aging temperature of 700°C. In all aging experiments, the nominal aging temperature always occurs at the mid-section of the LNT, located 38 mm from the inlet.

4.3 – Evaluation of LNTs

Fresh and aged LNTs are evaluated at 200, 300, and 400°C; these temperatures are selected since they represent typical in situ operating temperatures of a LNT. Prior to each evaluation experiment, while the temperature of the reactor is increasing to the next evaluating temperature, a 30 s pulse of the rich phase gases is introduced to the reactor in order to ensure complete removal of the stored NO_x on the LNT from the previous evaluation.

4.3.1 – Evaluation of LNTs at 200°C

At an evaluating temperature of 200°C, the average NO_x outlet concentration of fresh and aged LNTs does not reach steady state even after three hours of evaluation,

regardless of the aging temperature or the number of aging cycles. Figure 4.3.1 shows the NO and NO_x outlet concentration histories for an entire evaluation experiment at 200°C, whereas Figure 4.3.2 shows only a snapshot of four lean/rich cycles from the same evaluation experiment. The inability of the LNT to achieve steady state NO_x conversion when evaluating at 200°C is manifested in Figure 4.3.1; the NO_x conversion has not reached steady state after two hours of evaluating. The troughs and peaks, which correspond to NO_x storage and NO_x reduction, respectively, are seen more clearly in Figure 4.3.2 and are still increasing in intensity at the end of the experiment. This indicates that the storage capacity is continuing to decrease and that the amount of NO_x released during the rich cycle is also still increasing in magnitude.

Figure 4.3.3 shows the NO_x conversion history of the final cycle of each evaluation experiment performed at 200°C after aging at 900°C. Interestingly, neither the NO_x storage nor the NO_x excursion portions of the history appear to change with number of aging cycles until after aging for 300 cycles. This is probably a result of the experimental procedure used when evaluating at 200°C. Typically, since evaluations at 200°C did not reach steady state, only the evaluation experiments performed on the fresh LNT and the LNT aged for the greatest number of aging cycles (in this case 300) are allowed to continue for more than two hours. The other evaluations have durations of approximately 30 minutes. Therefore, it is predicted that the NO_x storage for the evaluation experiments after aging for 5, 25, 50, 100, 150, or 200 cycles would lie somewhere between that shown for the fresh LNT and the LNT aged for 300 cycles if these experiments had been run for similar durations.

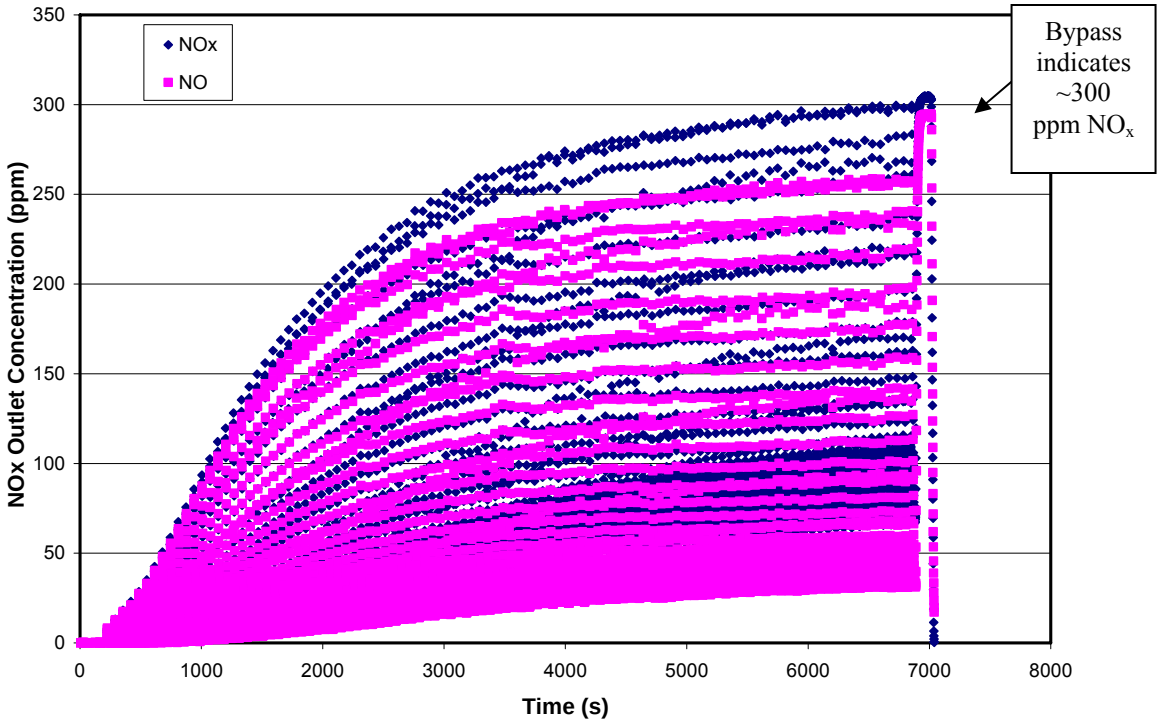

Figure 4.3.1 – NO_x outlet concentration history of fresh LNT evaluated at 200°C

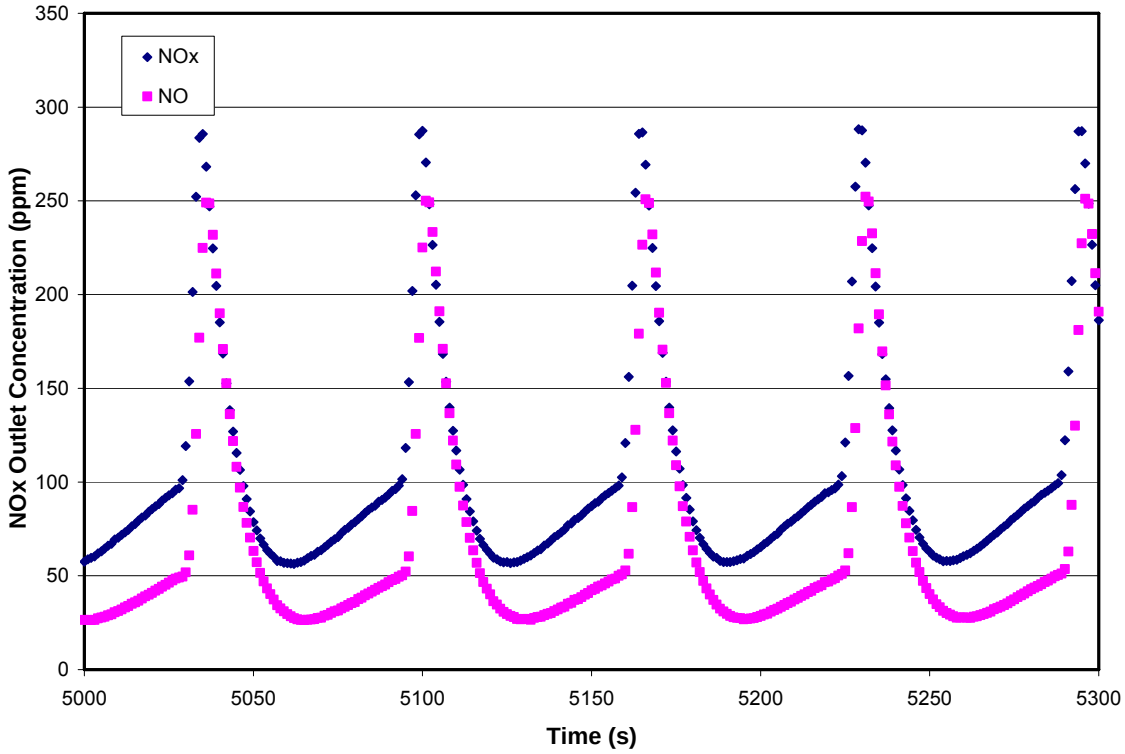

Figure 4.3.2 – Snapshot of evaluation of fresh LNT at 200°C shows large NO_x excursions and small storage capacity

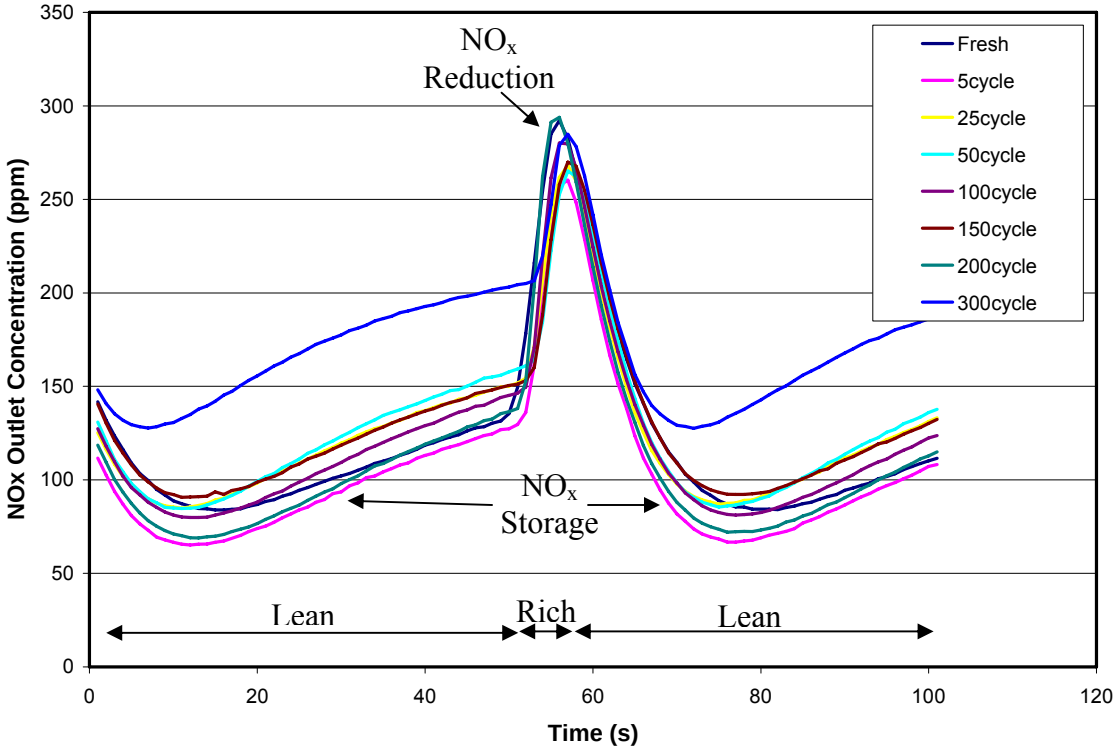

Figure 4.3.3 – NO_x outlet concentration histories of one cycle of LNTs evaluated at 200°C and aged at 900°C for the indicated number of aging cycles

The increase in magnitude of the NO_x outlet concentration during the storage phase (reduction and storage phases are labeled on the figure) with increasing number of aging cycles indicates that the NO_x storage capacity decreases as a result of aging. In comparison to evaluation experiments at 300°C (presented in Section 4.3.2), the quantity of NO slipping through the catalyst unoxidized is relatively high, indicating that the NO to NO_2 oxidation reaction is not as effective at 200°C as it is at 300°C. On the other hand, there is also a lot of NO_2 slipping through the LNT unreduced, indicating that either the NO_2 formed cannot be stored on the LNT, or the stored NO_x cannot be released and reduced. Recently, the NO_x storage mechanism of this LNT has been examined in a set of experiments (not presented) which has shown that NO_x storage readily occurs at 200°C.

For this reason, and because of high surface nitrate stability and low reduction reaction rate at low temperatures, ineffective NO_x release and reduction is probably responsible for the large NO_x slip. The large NO_x excursions at 200^{o}C are a result of low reduction reaction rate at low temperatures [9, 16-18, 35-37]. Overall, the large NO_2 outlet concentration during both lean and rich phases indicates that evaluations at 200^{o}C are limited by the release and reduction of NO_x, and not the oxidation of NO to NO_2.

Figure 4.3.4 shows the temperature history during three typical evaluation cycles at 200^{o}C. The peaks are a result of the exothermic reactions between the reductants and O_2, and the troughs are a result of cooling during the NO_x storage process. Since the catalytic activity at each axial location (inlet, 5 mm, 19 mm, 38 mm, 57 mm, and exit) can be represented by the magnitude of the rich-cycle temperature excursion, this figure indicates that the majority of the reductants are consumed in the front half of the catalyst where the temperature excursions are largest. The majority of the reductants appear to be consumed at the 5 and 19 mm-locations where the exotherms are approximately 8 and 10^{o}C, respectively, followed by the 38 mm-location where the exotherm is approximately 7^{o}C. However, it is difficult to tell whether the gradients at the 19 and 38 mm-locations are a result of exothermic reactions or convection without analyzing the concentration of reductants remaining at these locations. The 38 and 57 mm-locations have higher baseline temperatures because of the temperature gradient across the catalyst. The gradient is normally less than 5^{o}C when evaluation experiments are begun, but it can increase during the experiment.

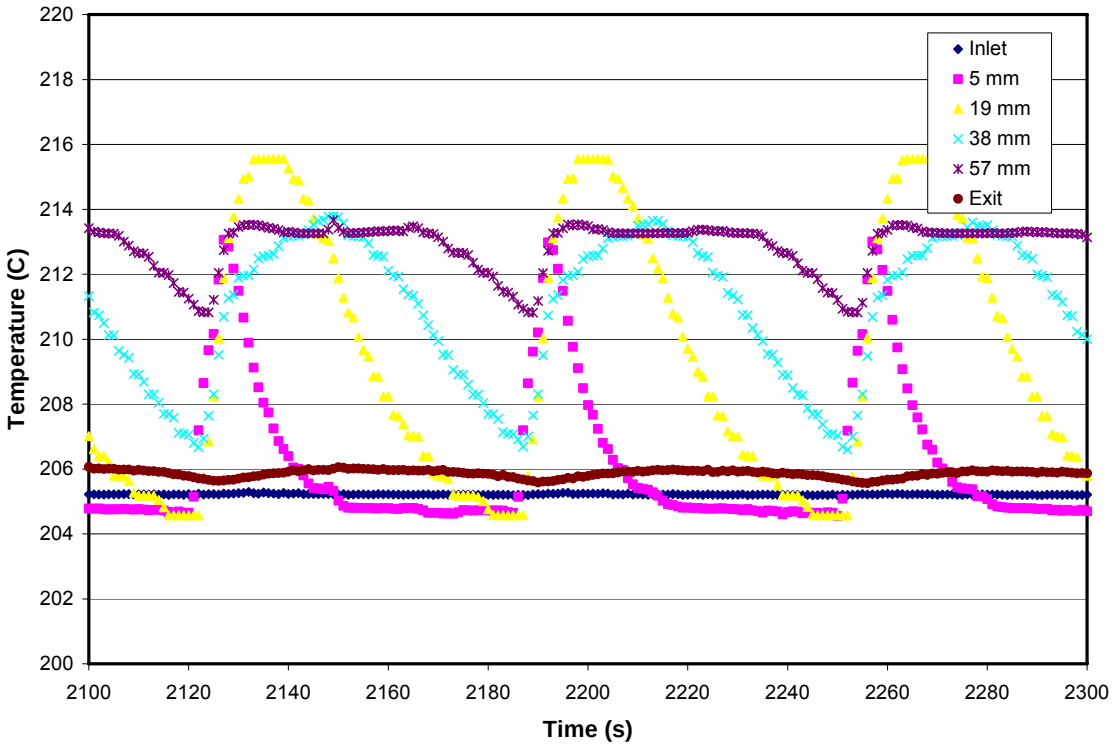

Figure 4.3.4 – Temperature history during evaluation of fresh LNT at 200°C

4.3.2 – Evaluation of LNTs at 300°C

Unlike evaluation at 200°C, steady state average NO_x outlet concentrations are always achieved when the LNT is evaluated at 300°C, irrespective of whether the LNT is fresh or aged. The outlet NO_x concentration of a fresh LNT evaluated at 300°C has already been shown in Figure 4.1.3, in which almost no NO_x is detected at the catalyst outlet. However, the NO_x outlet concentration increases as a result of aging. As seen in Figure 4.3.5 and Figure 4.3.6, a snapshot of the steady state portion of Figure 4.3.5, the average steady state NO_x outlet concentration is approximately 24 ppm corresponding to a NO_x conversion of approximately 92% after aging at 900°C for 50 cycles (See Section 4.5 for the method used to determine the NO_x). The abrupt increase in NO and NO_x outlet concentrations to approximately 296 and 304 ppm, respectively, at 2600 s is a result of diverting the flow of the simulated exhaust gases from the reactor to the bypass. This is done before and after each experiment in order to ensure the constancy of the NO_x inlet concentration and the accuracy of the NO_x analyzers.

Figure 4.3.7 shows the NO_x conversion history of the final cycle of each evaluation experiment performed at 300°C after aging at 900°C. In comparison to the NO_x excursions (peaks) and NO_x storage (troughs) seen in Figure 4.3.3 for the sample evaluated at 200°C, the NO_x excursions are much smaller and the amount of NO_x stored is much greater when evaluating at 300°C.

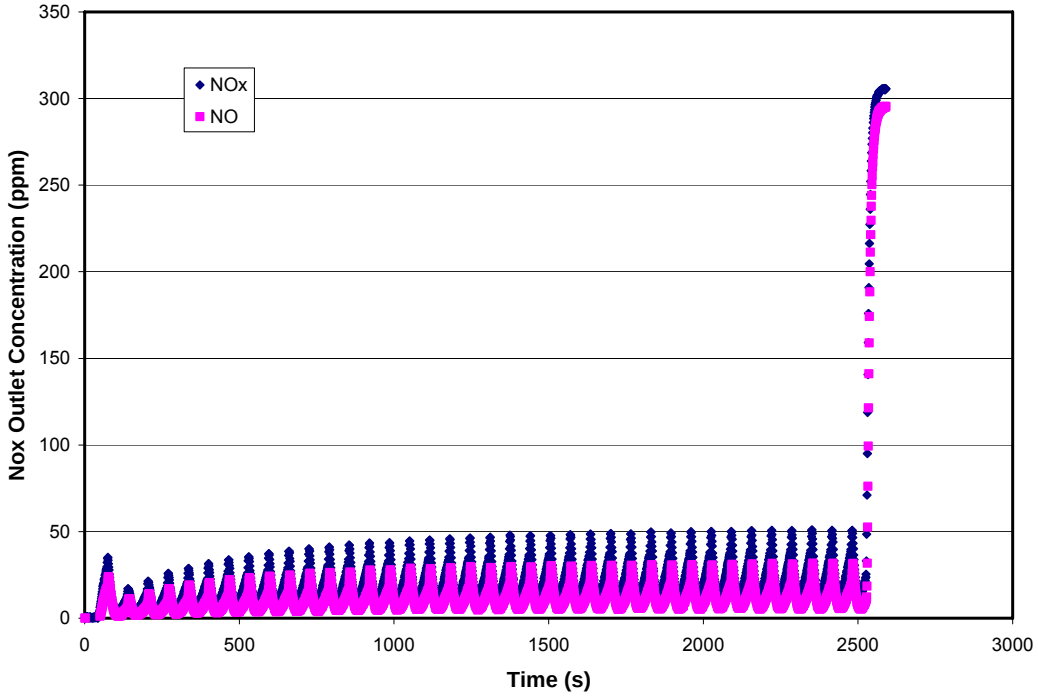

Figure 4.3.5 –NO_x outlet concentration history of LNT evaluated at 300°C after aging at 900°C for 50 cycles

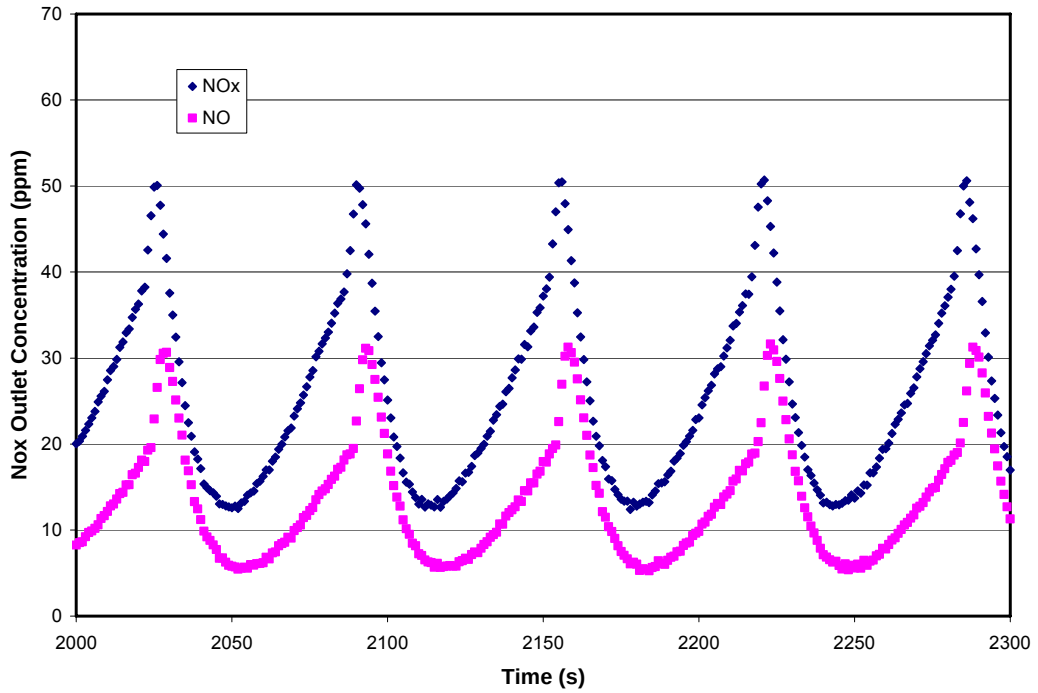

Figure 4.3.6 –Snapshot of evaluation of LNT at 300°C after aging at 900°C for 50 cycles shows smaller NO_x excursions and greater NO_x storage than at 200°C

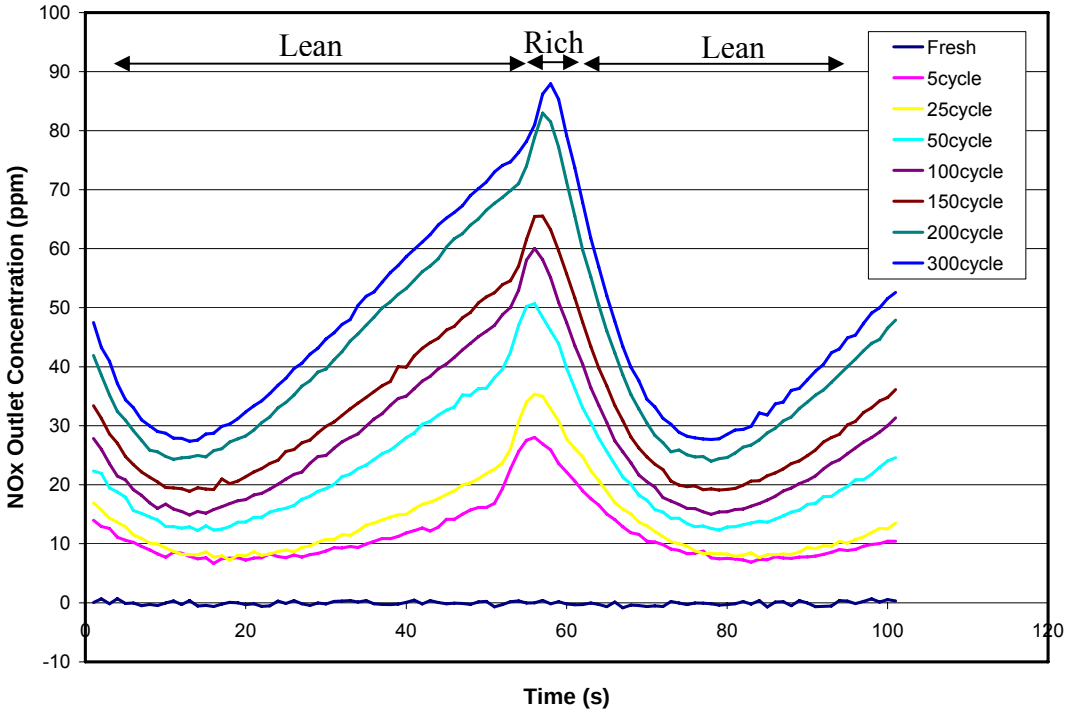

Figure 4.3.7 – NO_x outlet concentration histories of one cycle of LNTs evaluated at 300°C and aged at 900°C for the indicated number of aging cycles

Obviously, the NO_x outlet concentration increases during the storage phase with number of aging cycles indicating that the storage capacity decreases, but it is difficult to discern the effect that number of aging cycles has on the reduction of NO_x because the magnitude of the release increases relative to the loss in storage capacity.

The significant decrease in the amount of NO slip and the increase in the amount of NO_x stored are primarily due to the thermodynamically favorable conversion of NO to NO_2 over Pt and the lower stability of surface nitrates (improved NO_x release) at 300°C [9, 16-18]. The reduction in the magnitude of the NO_x excursion in comparison to that observed for the LNT evaluated at 200°C is a result of lower surface nitrate stability and the exponential increase in reaction rate with increasing temperature, indicated by the

Arrhenius rate law shown in Equation 4.1 [9, 35-37]. At 300°C NO_2 outlet concentrations are still much larger than NO outlet concentrations indicating that NO_x conversion is limited by either the NO_x storage or release/reduction mechanisms, and not by NO to NO_2 oxidation. However, it is difficult to determine which of these two mechanisms is controlling since both NO_x storage and NO_x release/reduction are extremely effective at 300°C.

$$Rate = A * e^{-E_a / RT} \tag{4.1}$$

The temperature history during evaluations at 300°C shown in Figure 4.3.8, indicates again that the majority of reductants are consumed in the front-half of the catalyst where the temperature excursions are the highest. In comparison to the temperature profile of the 200°C evaluation, the temperature excursions are much larger at evaluation temperatures of 300°C due to the increase in reaction rates with increasing temperature.

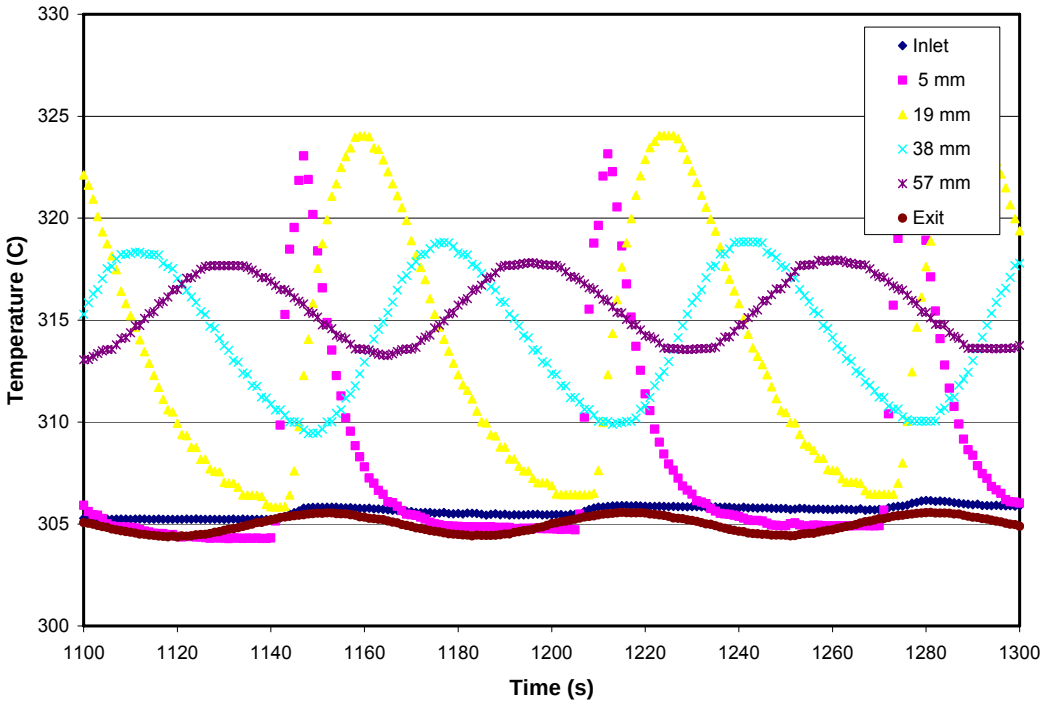

Figure 4.3.8 – Temperature history during evaluation of fresh LNT at 300°C

4.3.3 – Evaluation of LNTs at 400°C

A Typical NO_x outlet concentration history for evaluations performed at 400°C is shown in Figure 4.3.9, and a shapshot of four cycles of the steady state portion of this history is shown in Figure 4.3.10. Initially, there is no NO or NO_x slip, but the amount of NO and NO_x slipping through the LNT increases with increasing number of evaluation cycles, until after 20 evaluation cycles when a steady state average NO_x outlet concentration is reached.

Figure 4.3.11 shows the NO_x conversion history of the final cycle of each evaluation experiment performed at 400°C after aging at 900°C. From this figure it is clear from the NO_x outlet concentration during the storage phase that the NO_x storage capacity is less than that shown for evaluations at 300°C and higher than that shown for evaluations at 200°C. This is a result of two contributing factors. NO to NO_2 oxidation is equilibrium-limited at 400°C, and there is thus a much larger amount of NO slip than at 300°C. Also, the stability of nitrates is lower at 400°C than at 200 or 300°C, which means that less oxidized NO_2 can be stored and later reduced during the rich phase. Thus, there is also a large amount of NO_2 slip. Unlike at the other two evaluating temperatures, the storage capacity sharply decreases after only 5 aging cycles indicating that aging severely degrades NO_x storage at 400°C. The magnitude of the rich phase NO_x excursion follows the same trend as did NO_x storage, with larger NO_x excursions than those seen at 300°C and smaller ones than those observed at 200°C. The excursions are larger than at 300°C because a large portion of the oxidized NO_2 is never stored and is thus unlikely to be reduced on the PGM sites, and the excursions are smaller than those at 200°C

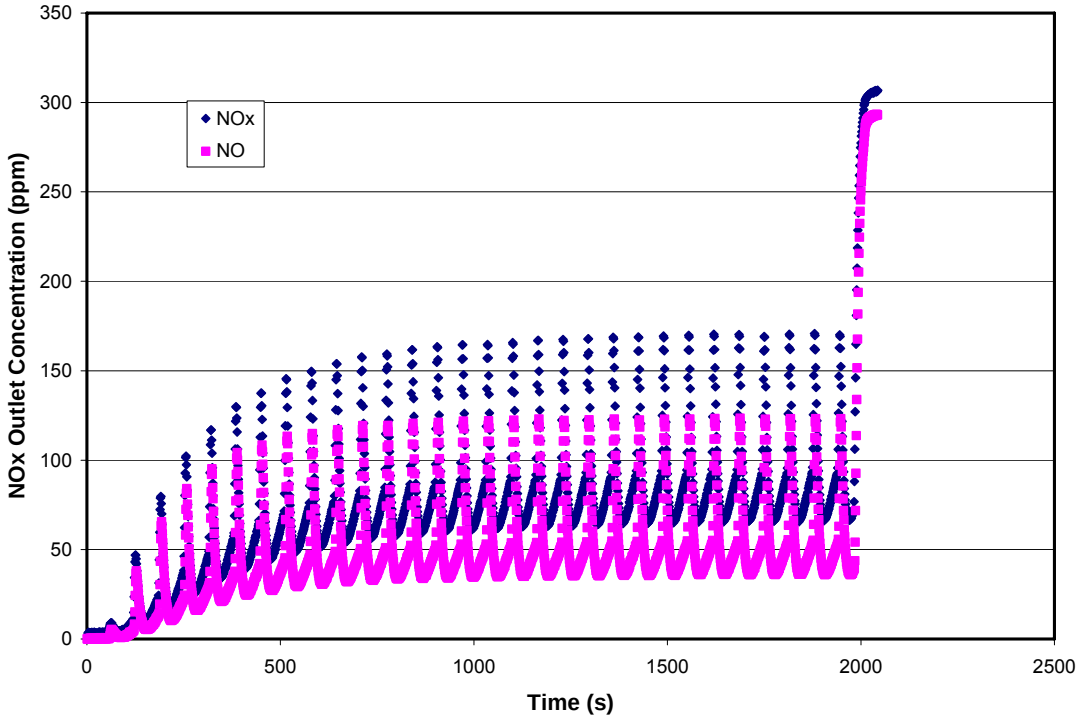

Figure 4.3.9 – NO_x outlet concentration history of LNT evaluated at 400°C after aging at 900°C for 50 cycles

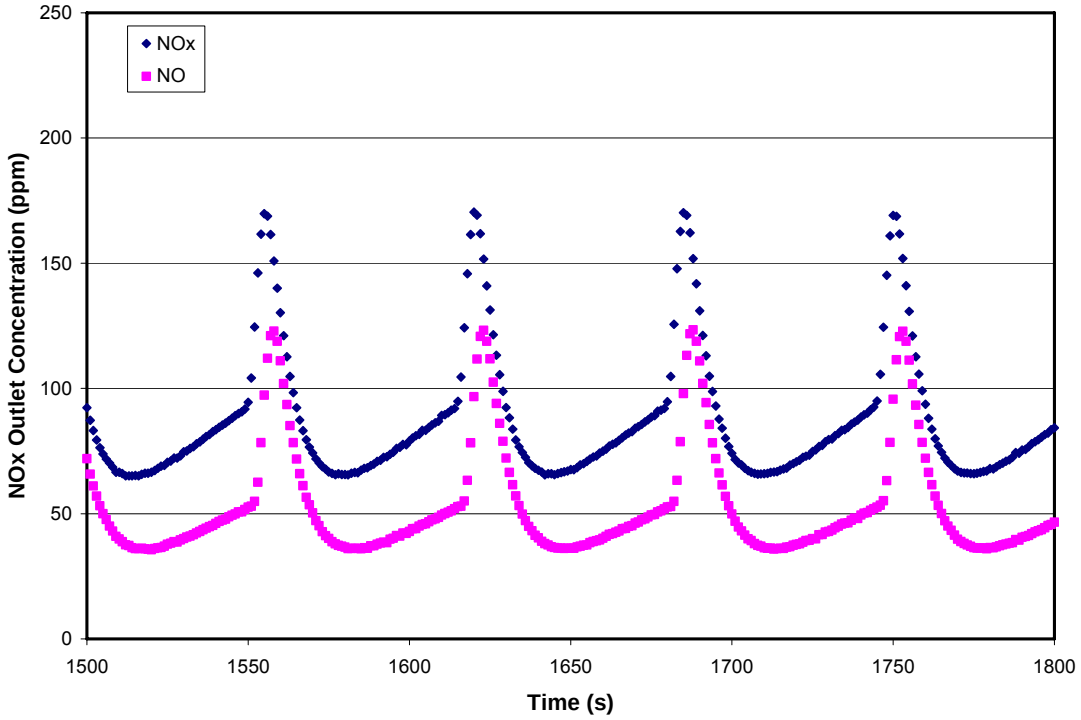

Figure 4.3.10 –Snapshot of evaluation of LNT at 400°C after aging at 900°C for 50 cycles

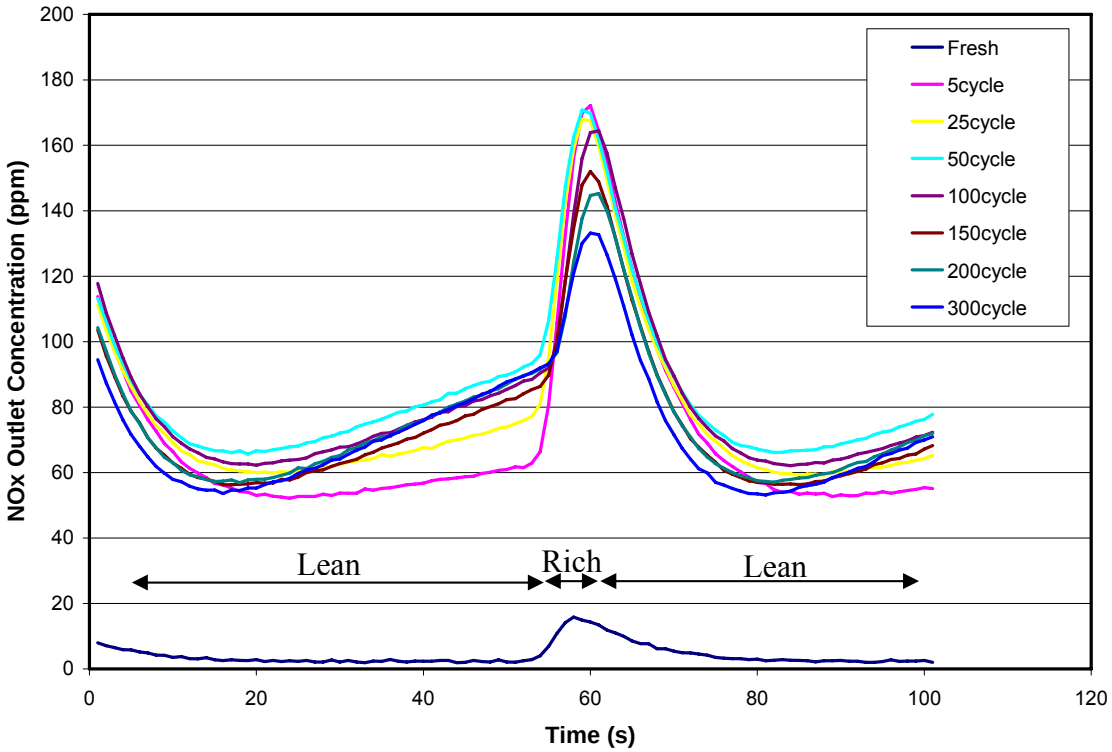

Figure 4.3.11 – NO_x outlet concentration histories of one cycle of LNTs evaluated at 400°C and aged at 900°C for the indicated number of aging cycles

because reduction of NO_x is much more efficient at 400°C [9, 35-37]. Overall, high NO_2 outlet concentrations indicate that NO_x conversion is still controlled by NO_x storage or release/reduction. However, at 400°C the controlling mechanism is likely to be NO_x storage because at high temperatures surface nitrates are no longer stable and are not easily formed.

The temperature history shown in Figure 4.3.12 is similar to those obtained at other evaluation temperatures, in which the magnitude of the temperature excursion decreases from the front to the rear of the catalyst. Again, this indicates that the majority of reductants are consumed in the front-half of the LNT.

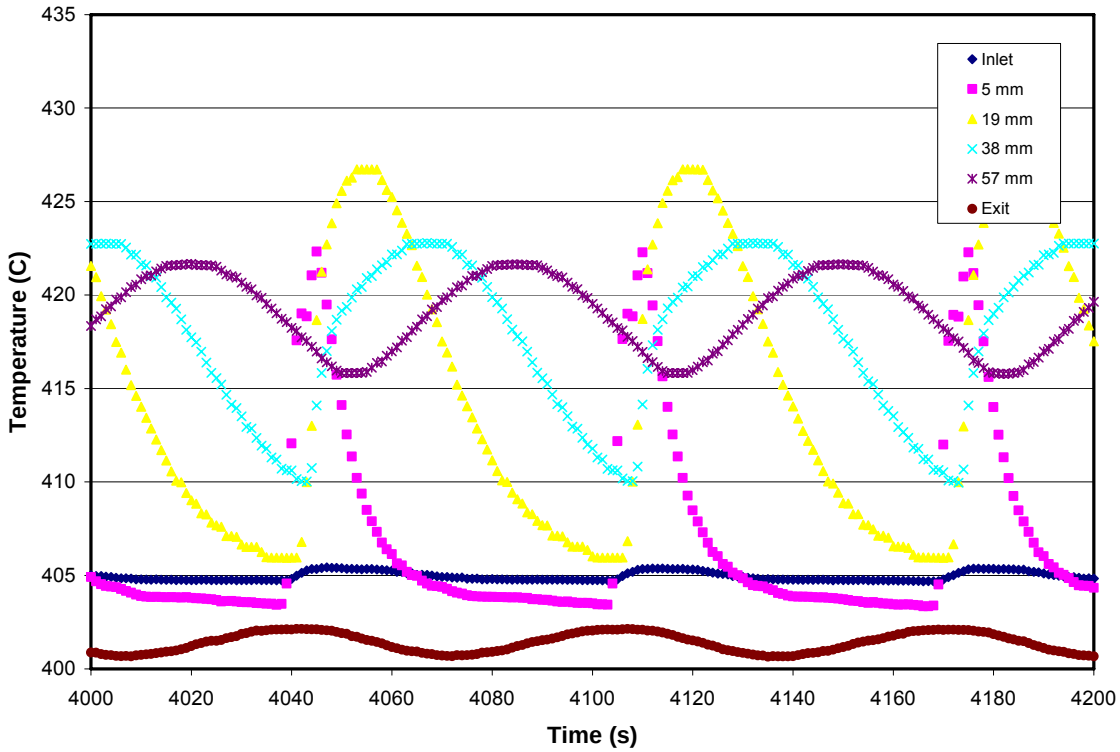

Figure 4.3.12 – Temperature history during evaluation of fresh LNT at 400°C

4.4 – Results of LNT NO_x Conversion Experiments

After each evaluation experiment is performed, NO_x conversion for that experiment is calculated. The NO_x conversion at a given aging temperature is then plotted against the number of aging cycles, and in this manner the effect of aging temperature and aging time on LNT performance can easily be ascertained. Before the plots are presented, the method used to determine the NO_x conversion is shown.

4.4.1 – Calculation of NO_x Conversion

Using a truncated portion of Figure 4.3.6, the NO_x conversion calculation will be illustrated. Figure 4.4.1 is the steady state portion of the evaluation experiment presented in Figure 4.3.6. Notice that the cycle-to-cycle maximum and minimum NO_x outlet concentrations do not change. The NO_x conversion is calculated by taking the average NO_x outlet concentration of the last five steady state cycles and dividing that by the inlet concentration of NO_x determined with the bypass as seen in Equation 4.4.

$$NO_x\ Conversion = \frac{Inlet\ NO_x\ Concentration - Average\ SS\ Outlet\ NO_x\ Concentration}{Inlet\ \ NO_x\ \ Concentration} \qquad (4.4)$$

The steady state average NO_x conversion is calculated rather than the average NO_x conversion of the entire experiment because vehicles using LNTs will primarily operate in the steady state regime.

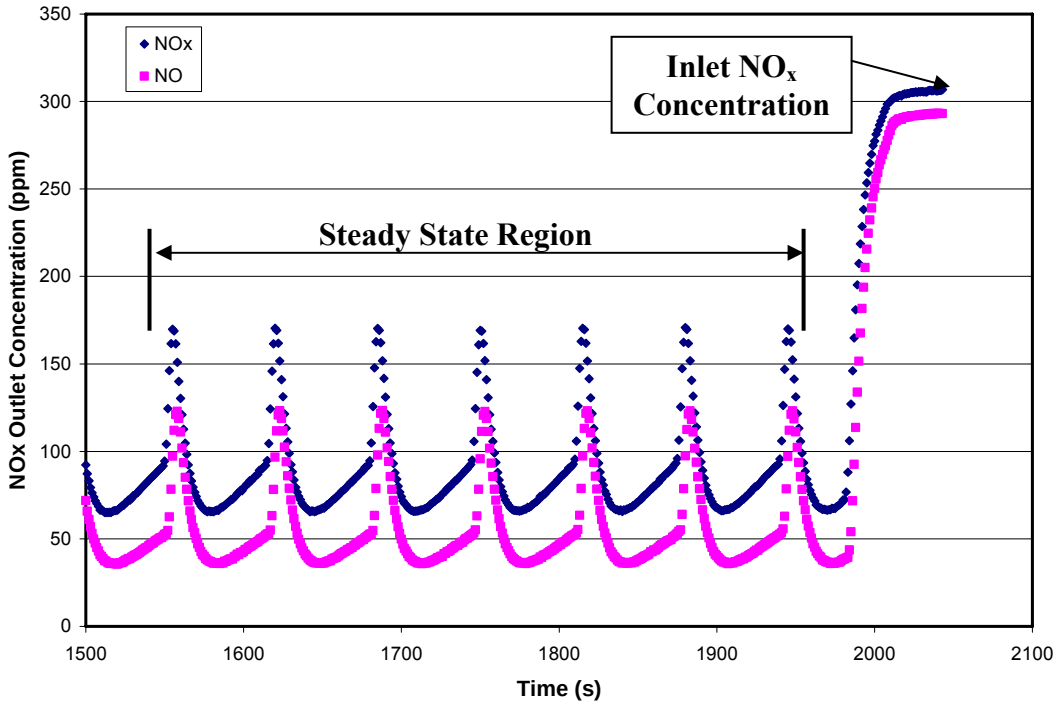

Figure 4.4.1 –Steady state portion of NO_x outlet concentration during evaluation of LNT at 400°C after aging at 900°C for 50 cycles

4.4.2 – Effect of High Temperature Aging on NO_x Conversion

Figures 4.4.2 to 4.4.5 show the effect of number of aging cycles on LNT performance after aging at 700, 800, 900, and 1000°C, respectively, and Tables 4.1 to 4.4 list the exact NO_x conversion values shown in the figures as functions of number of aging cycles and evaluation temperature. As seen in the figures, NO_x conversion is most affected at aging temperatures of 900 and 1000°C, with very little performance degradation after aging at 700 and 800°C. The reasons for this reduction in NO_x conversion after high-temperature aging are discussed later in Section 4.5.

Figures 4.4.6 to 4.4.8 present the effect of aging temperature and number of aging cycles for evaluations at 200, 300 and 400°C, respectively. These figures clearly indicate that the NO_x conversion at all three evaluating temperatures is most affected by aging at 900 and 1000°C. Notably, the NO_x conversion at 300°C gradually decreases to a steady state value, whereas the NO_x conversion at 400°C rapidly decreases to a steady state value after only 5 cycles of aging. This difference may indicate that the reduction in surface area plays a larger role in NO_x conversion at 400°C than it does at 300°C. The surface area measurements are presented later in Section 4.5.3, but they show a large decrease in surface area after aging at 900 and 1000°C for only 10 cycles. This rapid reduction in surface area correlates well with the rapid reduction in NO_x conversion when evaluating at 400°C.

Table 4.1 – Average steady state NO_x conversions after aging at 700°C as a function of the number of aging cycles and the evaluation temperature

Number of Aging Cycles	Evaluation Temperature (°C)		
	200	300	400
0	62.6	100	99.4
25	57.9	96.3	95.5
50	55.7	99.6	95.9
100	54.7	100	94.4
150	57	99.3	92.4
200	55.6	97.8	92.2

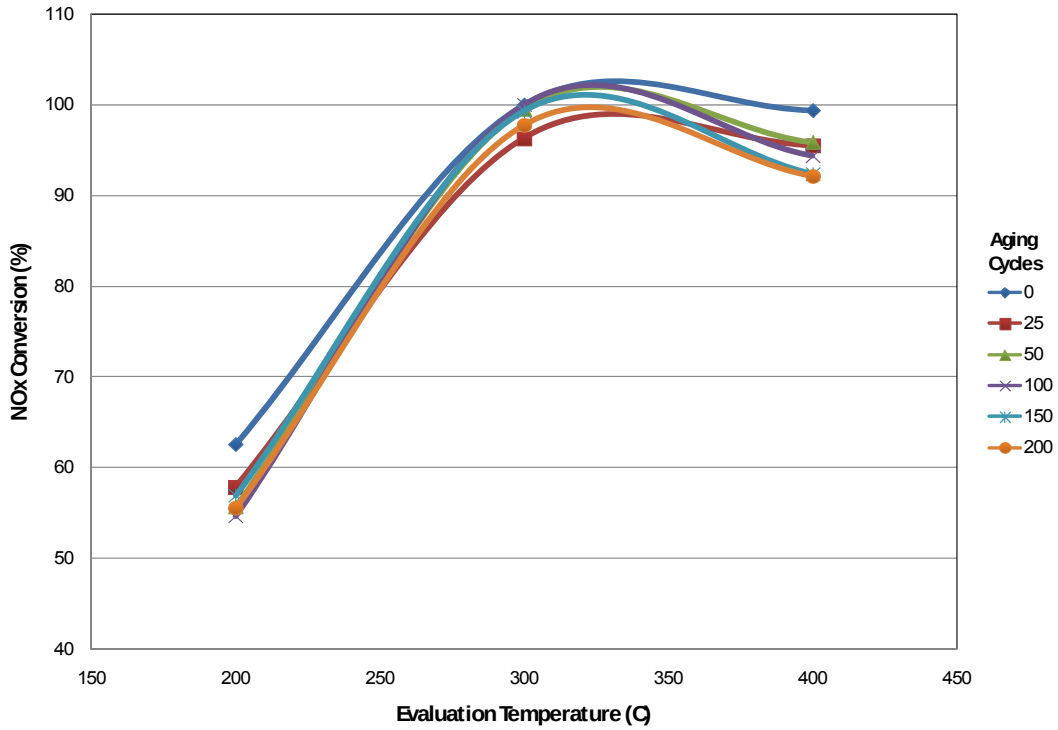

Figure 4.4.2 – Effect of number of aging cycles and evaluating temperature on NO_x conversion of LNTs aged at 700°C

Table 4.2 – Average steady state NO_x conversions after aging at 800°C as a function of the number of aging cycles and the evaluation temperature

Number of Aging Cycles	Evaluation Temperature (°C)		
	200	300	400
0	71.7	97.5	94.1
5	54.3	99.2	91.4
25	58.1	99.2	88.7
50	59.7	99.6	86.7
100	57.8	99.8	86.7
150	57.7	99.4	88.2
200	47.8	98.1	86.2

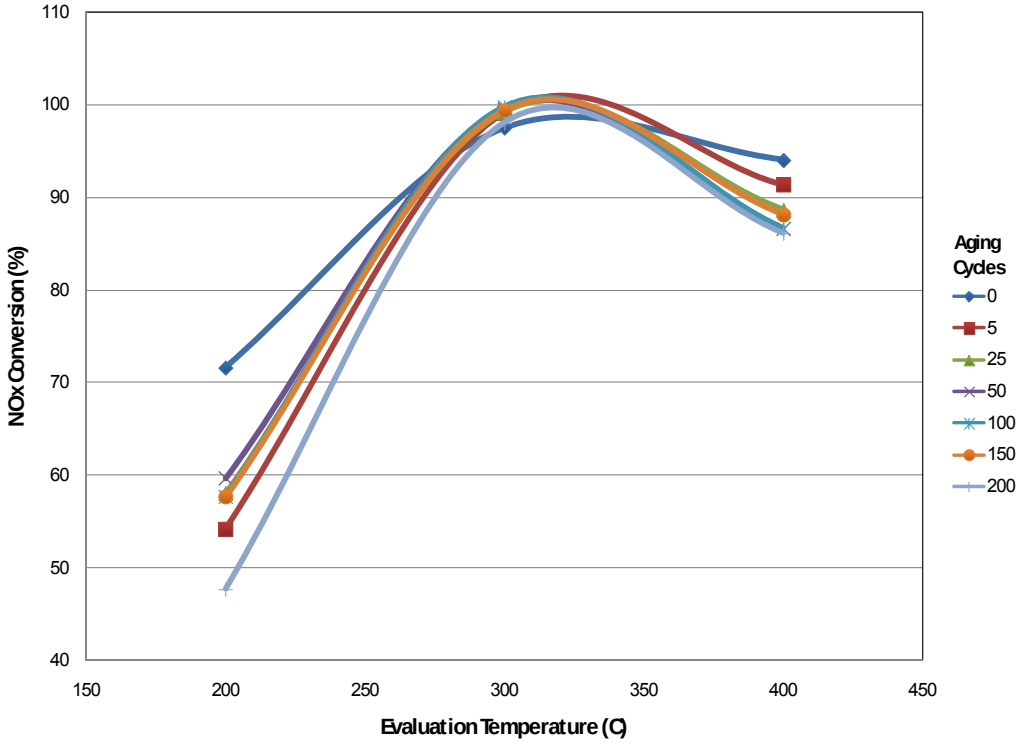

Figure 4.4.3 –Effect of number of aging cycles and evaluating temperature on NO_x conversion of LNTs aged at 800°C

Table 4.3 – Average steady state NO_x conversions after aging at 900°C as a function of the number of aging cycles and the evaluation temperature

Number of Aging Cycles	Evaluation Temperature (°C)		
	200	300	400
0	58	100	98.5
6	65	96	76
25	56.2	94.7	72.6
50	57.8	91.6	70.6
100	59.8	89.9	71.9
150	56.2	88	74
200	60.5	84.9	73.9
300	57.8	83.2	74.9

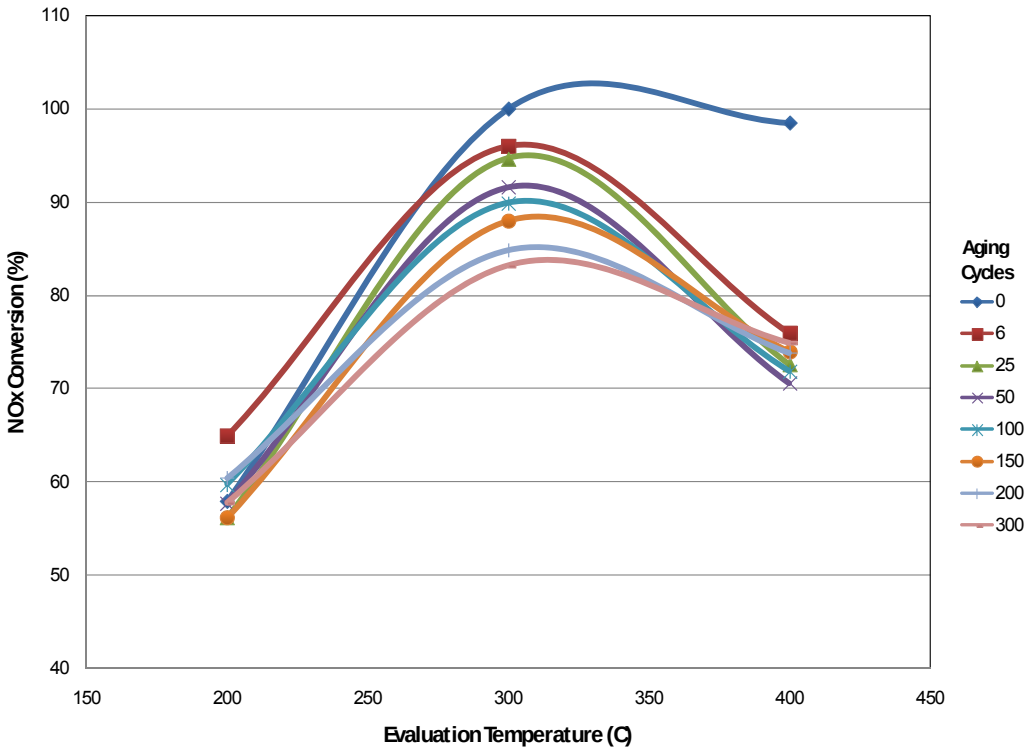

Figure 4.4.4 –Effect of number of aging cycles and evaluating temperature on NO_x conversion of LNTs aged at 900°C

Table 4.4 – Average steady state NO_x conversions after aging at 1000°C as a function of the number of aging cycles and the evaluation temperature

Number of Aging Cycles	Evaluation Temperature (°C)		
	200	300	400
0	64.8	98.2	90
5	59.9	94.4	75.5
25	63	88.4	76.2
50	54.5	84	75.1
100	50	78.1	73.7
150	43.3	76.1	72.6
200	45.5	74.7	71.8
300	42.9	68.4	71.1
350	42.4	69.3	71.2

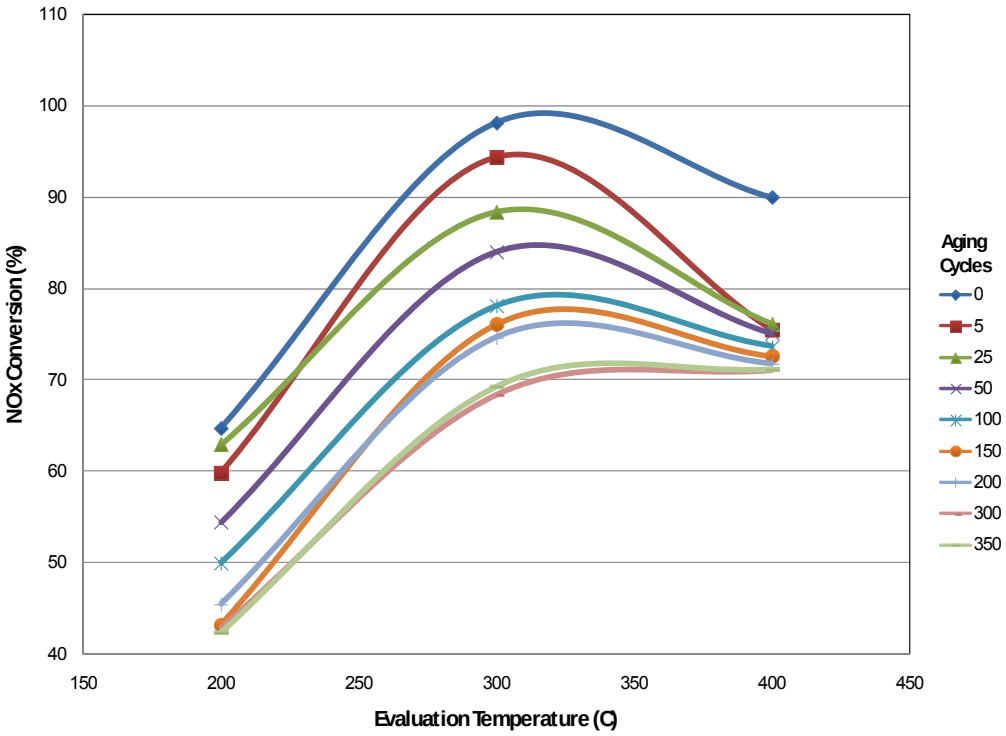

Figure 4.4.5 –Effect of number of aging cycles and evaluating temperature on NO_x conversion of LNTs aged at 1000°C

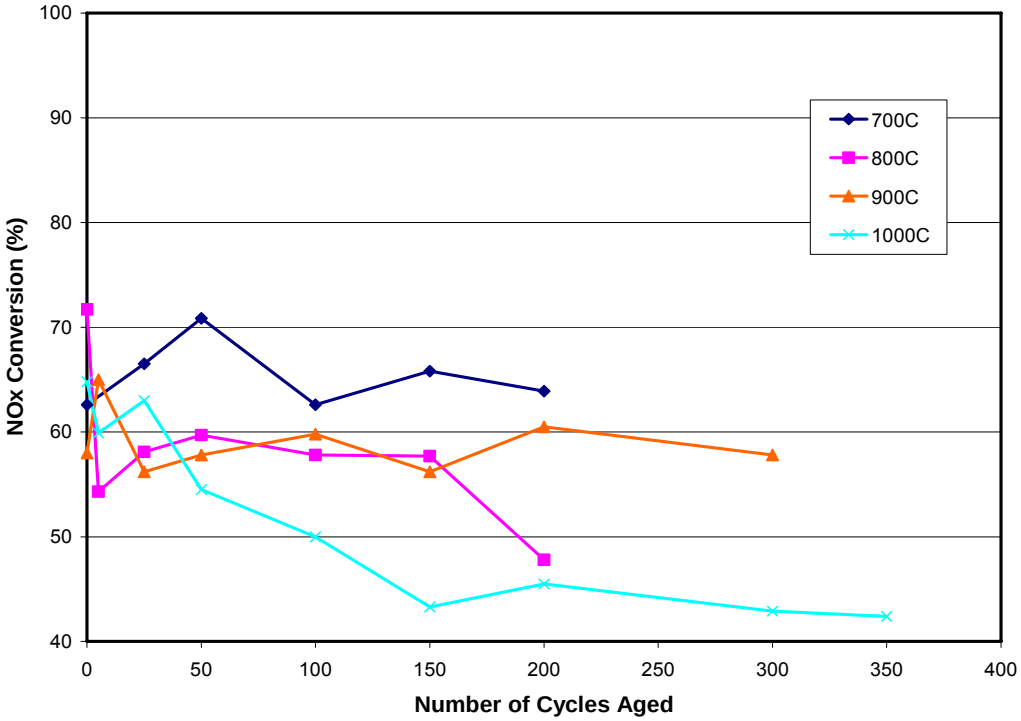

Figure 4.4.6 – NO_x conversion of LNTs evaluated at 200°C after aging at 700, 800, 900, and 1000°C

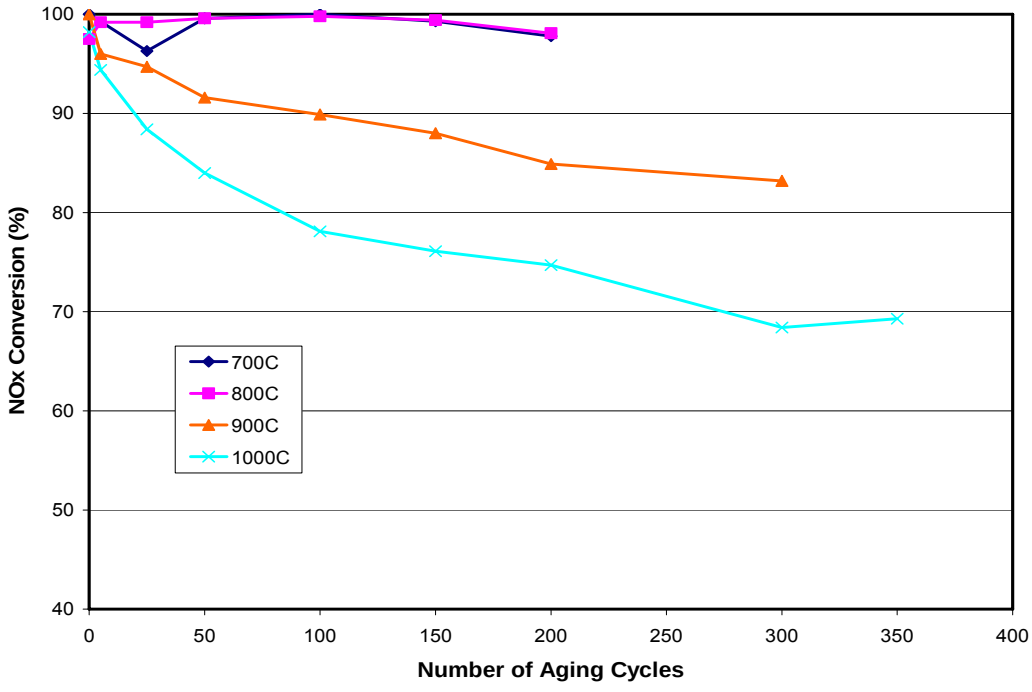

Figure 4.4.7 – NO_x conversion of LNTs evaluated at 300°C after aging at 700, 800, 900, and 1000°C

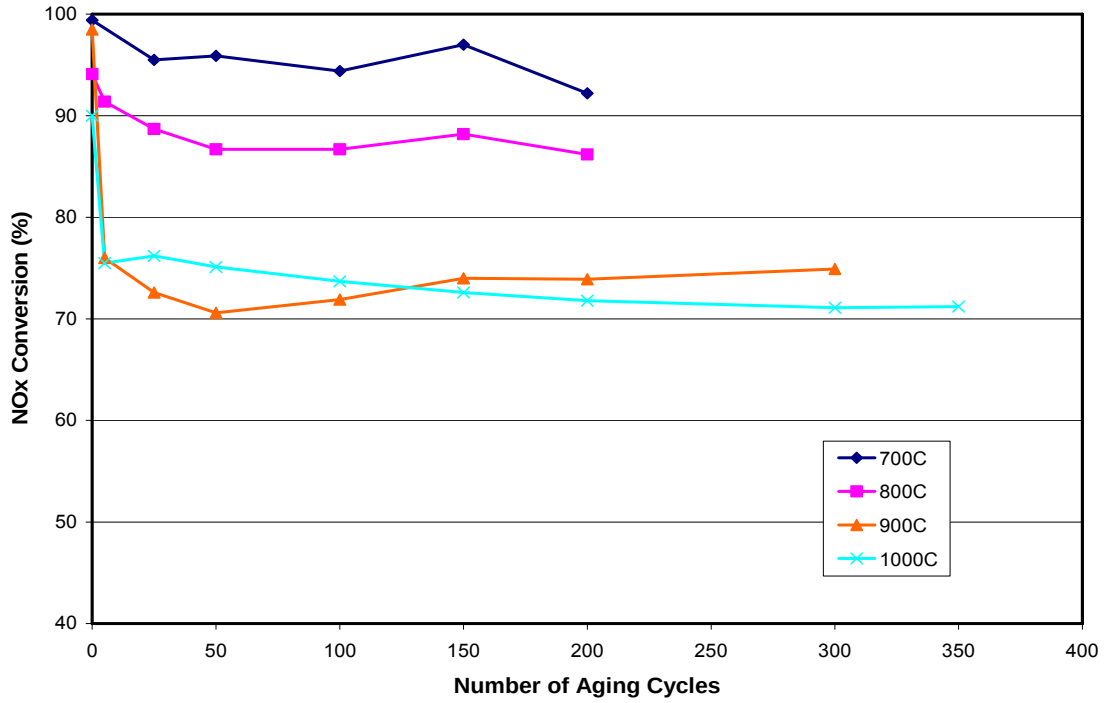

Figure 4.4.8 – NO_x conversion of LNTs evaluated at 400°C after aging at 700, 800, 900, and 1000°C

4.5 – Results of Surface Characterization Studies

Surface characterization studies are used to determine the deactivation mechanisms responsible for the reduction in the NO_x conversion performance as a result of thermal aging. The surface characterization techniques utilized for this study are chosen based on their ability to identify and quantify typical degradation mechanisms reported in the literature: PGM sintering; γ-Al_2O_3 phase transitions and surface area reduction; and Ba migration, agglomeration, and other physicochemical changes. As mentioned previously, powder XRD is used to determine average PGM particle size growth and to ascertain the formation of new compounds and phase transitions. TEM is used to obtain individual PGM particle sizes and particle size distributions, from which average PGM particle size can be calculated and compared with that obtained from XRD. Particle migration and agglomeration are analyzed with EPMA, and washcoat surface area reduction measurements are carried out with BET.

4.5.1 – EPMA Investigation of Ba and Ce Migration and Agglomeration

As described in Chapter 3, elemental maps and line scans are used to quantify migration and agglomeration of Ba and Ce, the NO_x storage and oxygen storage media, respectively. Line scans quantify the percentage of the selected element at a precise location and are used to analyze the distribution of the scanned elements within the washcoat. Figures 4.5.1 to 4.5.4 are line scans of fresh LNTs and LNTs aged at different temperatures and number of aging cycles. The line scans indicate that Ba remains well dispersed in the washcoat with an average concentration of 4.1 wt. percent even after

aging at 1070^{o}C for 350 cycles. Ce has an average concentration of 3.2 wt. percent and its distribution within the washcoat, though less uniform than that of Ba, also appears to remain unchanged after aging.

The Ba and Ce elemental maps of fresh LNTs and LNTs aged at the indicated temperature and number of aging cycles shown in Figures 4.5.5 and 4.5.6, respectively, appear to confirm qualitatively the results obtained from the line scans. The scale on the right side of each elemental map indicates the relative concentration of the scanned element. The concentration increases from black, none of the element is present, to red, only the element is present. As seen in both Figure 4.5.5 and 4.5.6, the substrate and the epoxy, neither of which contain any Ba or Ce, are almost completely black, whereas the washcoat is a shade of either blue, green, or red, depending on the Ba or Ce concentration. These results do not agree with those reported by Nguyen et al. in which they reported Ba agglomeration after aging at 830^{o}C for 100 cycles. Because of the similarity between the experimental setup and aging protocol used in the present study and those used by Nguyen et al., it is likely that the additives in this fully-formulated LNT prevented the migration and agglomeration of Ba.

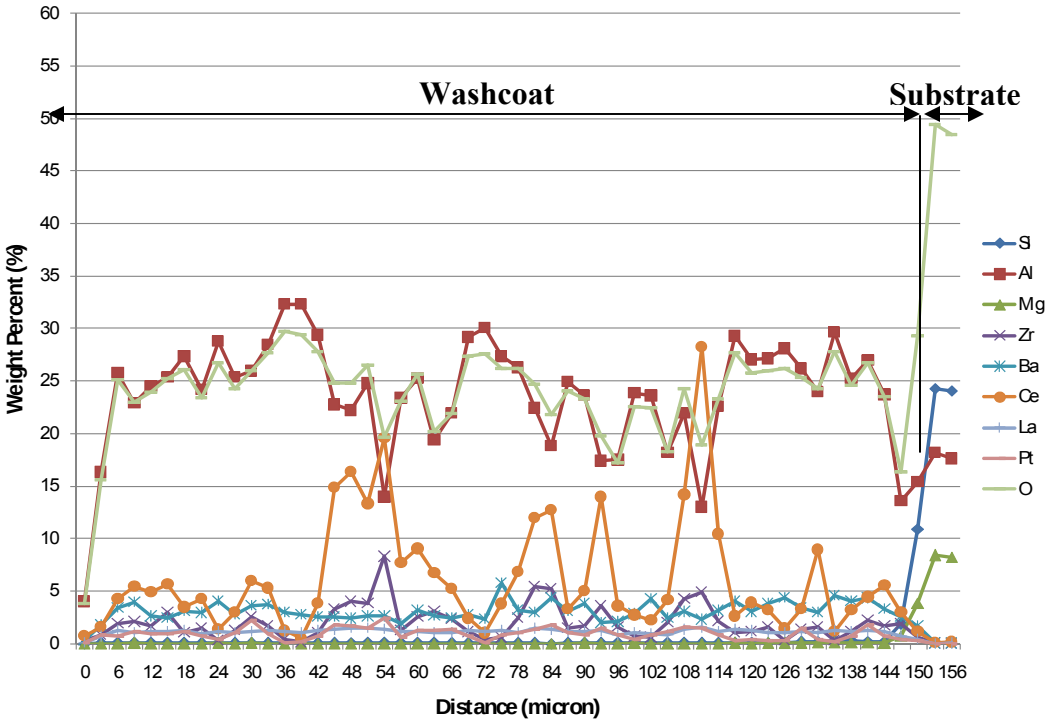

Figure 4.5.1 – EPMA line scan of fresh LNT

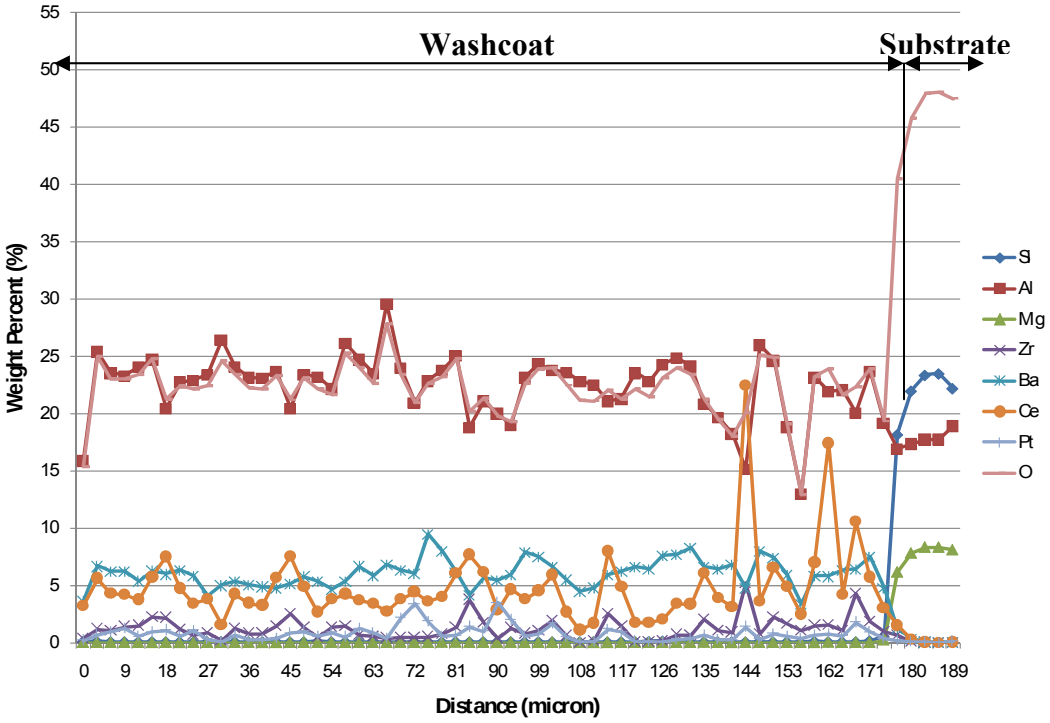

Figure 4.5.2 – EPMA line scan of LNT aged at 883°C for 200 cycles

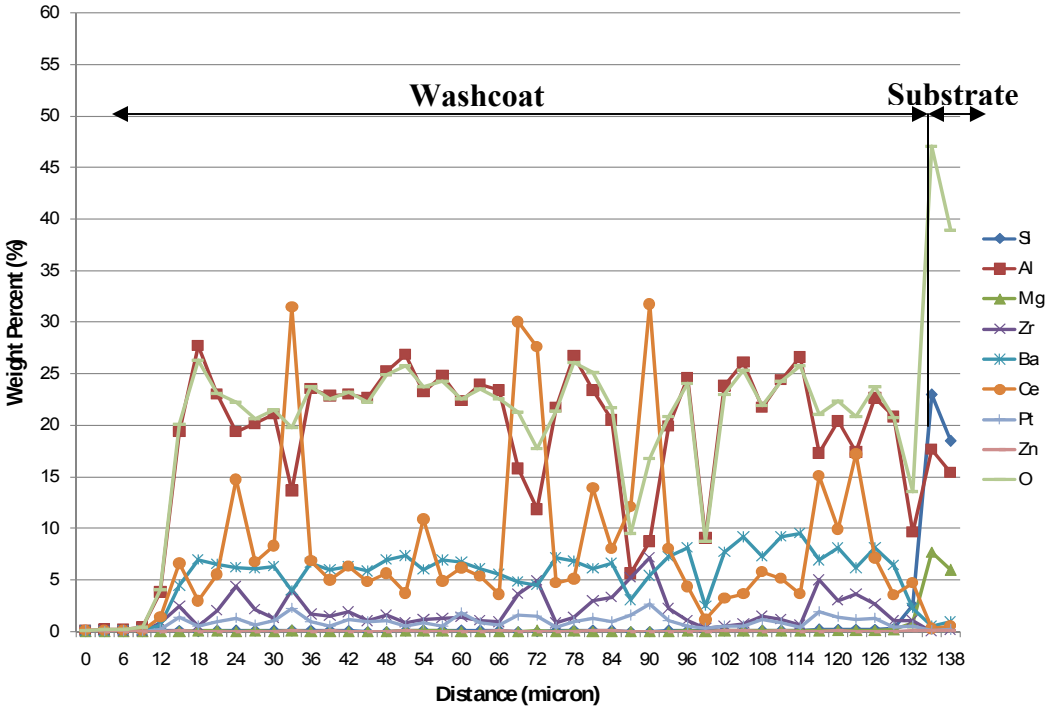

Figure 4.5.3 – EPMA line scan of LNT aged at 929°C for 300 cycles

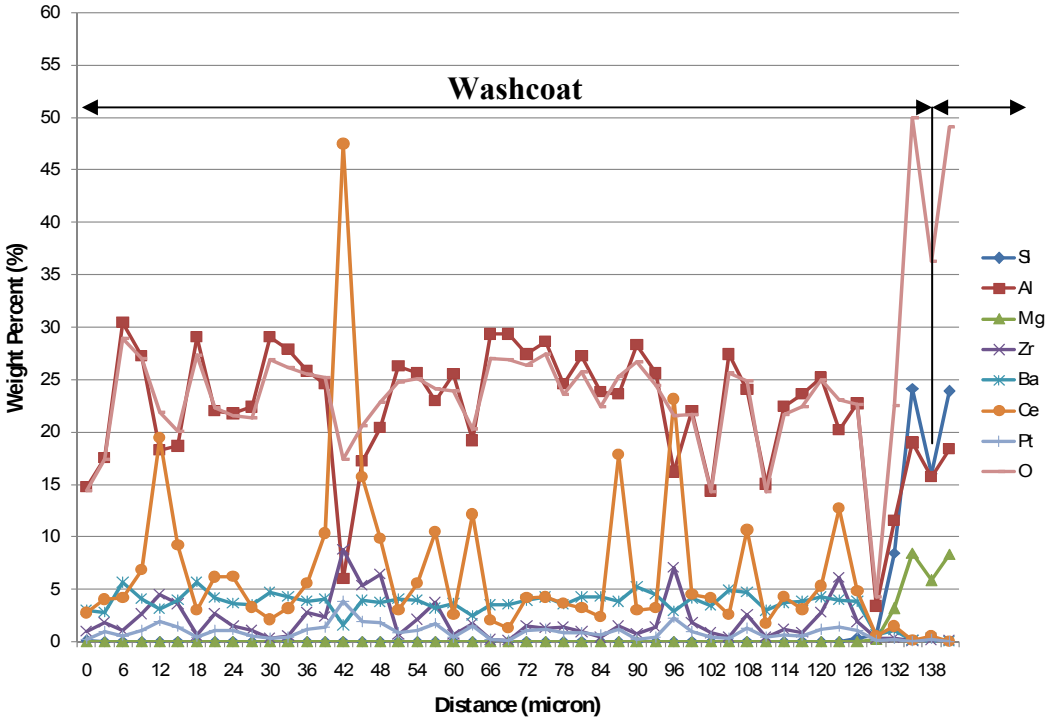

Figure 4.5.4 – EPMA line scan of LNT aged at 1070°C for 350 cycles

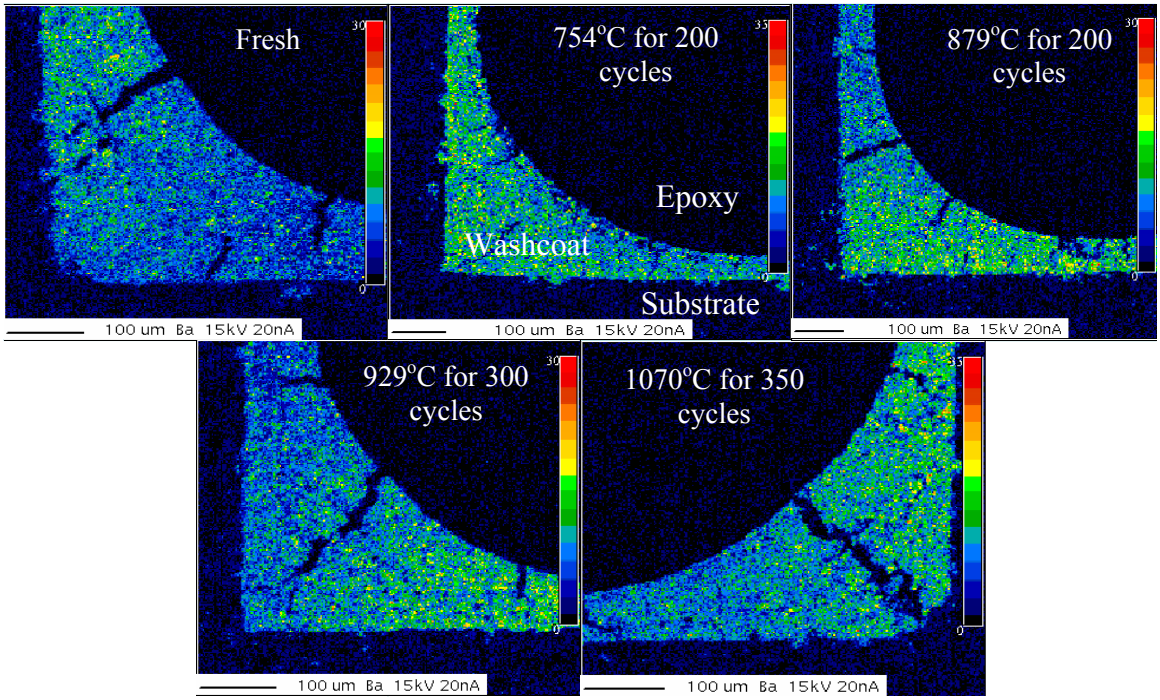

Figure 4.5.5 – EPMA Ba elemental maps of Fresh LNT and LNTs aged at different temperatures and number of aging cycles

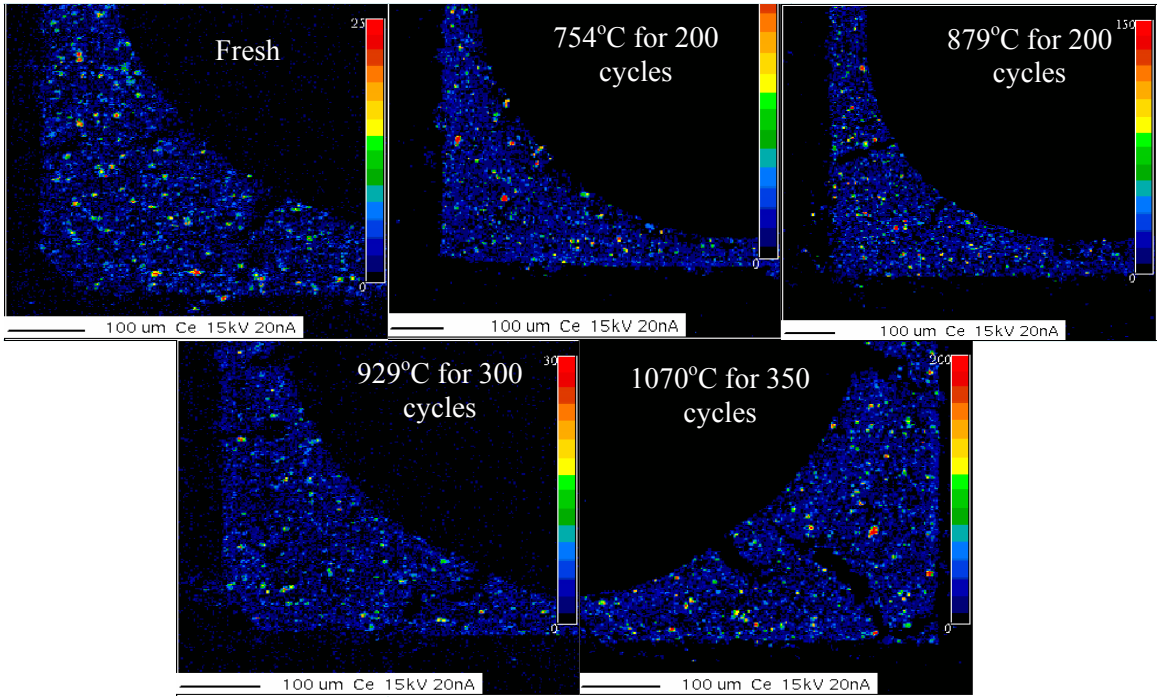

Figure 4.5.6 – EPMA Ce elemental maps of Fresh LNT and LNTs aged at different temperatures and number of aging cycles

4.5.2 – XRD and STEM-EDS Quantification of PGM Particle Size Growth

XRD patterns are used to obtain the growth of PGM particles as a result of aging. The Pt (111) peak centered at $2\theta = 40^{o}$ is used for the analysis because Pt is the most abundant of the precious metals used on this LNT, and its peak is the one with the highest intensity. The average PGM particle size is determined using the Scherrer equation and Rietveld analysis. In order to calculate the full-width at half maximum (FWHM) of the Pt (111) peak required for the Scherrer equation, Highscore® is used (Figure 4.5.7). Highscore, a software package used for XRD phase identification and quantitative analysis, is also used to perform Rietveld analyses, a technique used to deconvolute the different, overlapping peaks of complex XRD patterns (Figure 4.5.8). On the other hand, PGM particle size distributions are obtained from TEM micrographs using ImageJ®, an open-source image processing software and Microsoft Excel®. ImageJ is used to count and measure diameters of individual PGM particles, while Excel is used for statistical analysis and plotting of particle size distributions.

Average PGM particle sizes can be obtained from XRD patterns alone. However, the Pt (111) peak is only resolvable for particle sizes greater than 7.5 nm due to peak overlap at $2\theta = 40^{o}$. Figure 4.5.9 is a 3-D plot of XRD patterns of LNTs aged at different temperatures for 100 aging cycles, showing the progression of the growth of the Pt (111) peak with aging temperature. The Pt peak growth does not become significant until after the 8^{th} XRD pattern from the front, corresponding to the sample aged at 883^{o}C.

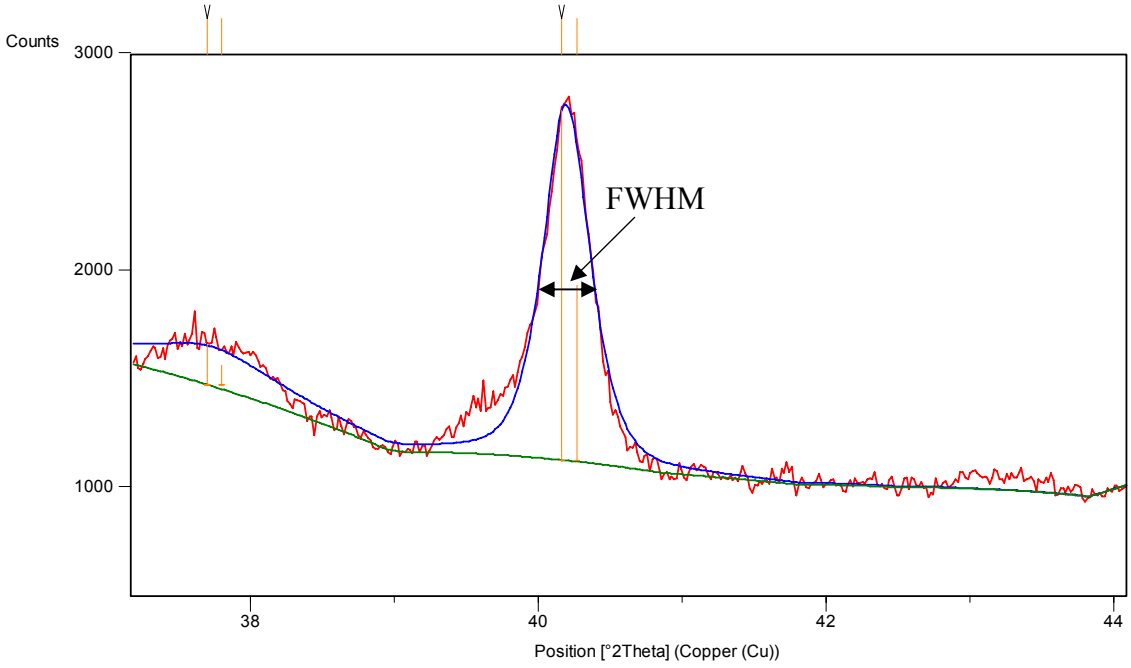

Figure 4.5.7 – Highscore is used to obtain the full-width at half maximum (FWHM) required by the Scherrer equation. This specific sample is aged at 1070°C for 350 cycles.

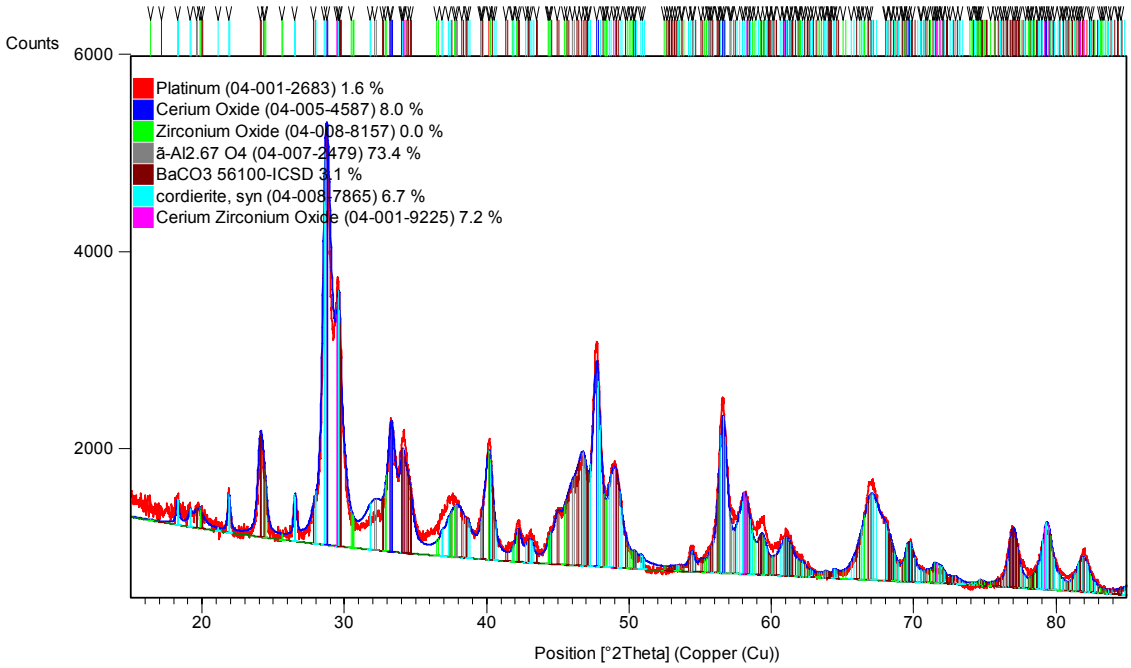

Figure 4.5.8 – Rietveld analyses are used to corroborate the particle size results calculated with the Scherrer equation.

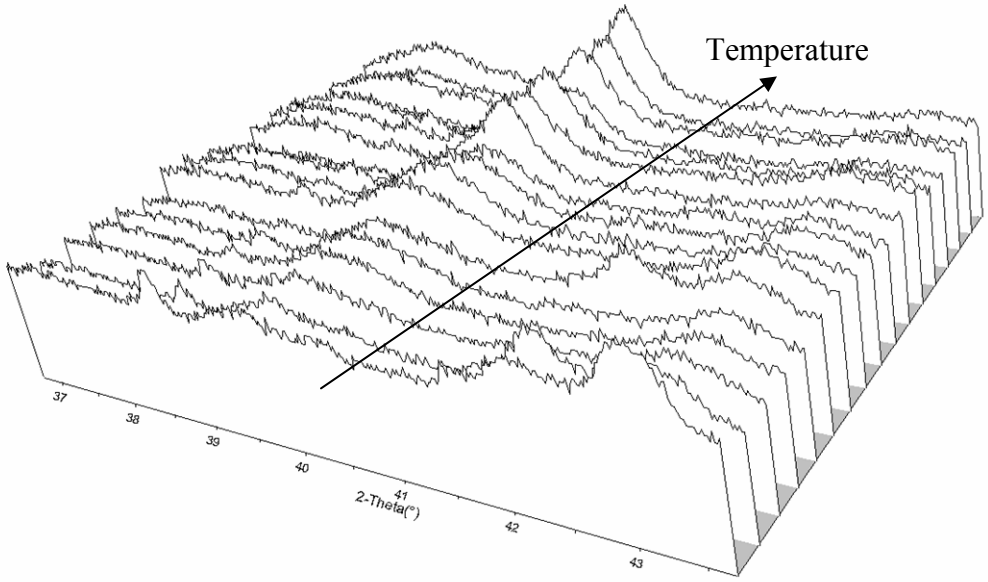

Figure 4.5.9 – Three-dimensional XRD patterns of LNTs aged at different temperatures for 100 cycles with the arrow indicating the direction of increasing aging temperature

Even with the limited resolution, XRD is still extremely useful in analyzing PGM particle size growth. In fact, it is the samples aged at the highest temperatures, with the most severe PGM sintering, that are the most interesting in this study; the Pt (111) peak becomes more discernible as the aging temperature increases. Analysis of those samples with average particle sizes within the resolution of the XRD instrument reveals that sintering of the PGM particles becomes more severe with increasing aging temperature and number of aging cycles. Figures 4.5.10 and 4.5.11 illustrate this growth with temperature and time, respectively, by showing the evolution of the Pt (111) peak. As the peak grows with increasing aging temperature or number of aging cycles, the FWHM decreases and the average particle size calculated with the Scherrer equation increases (See Chapter 3 for the Scherrer equation).

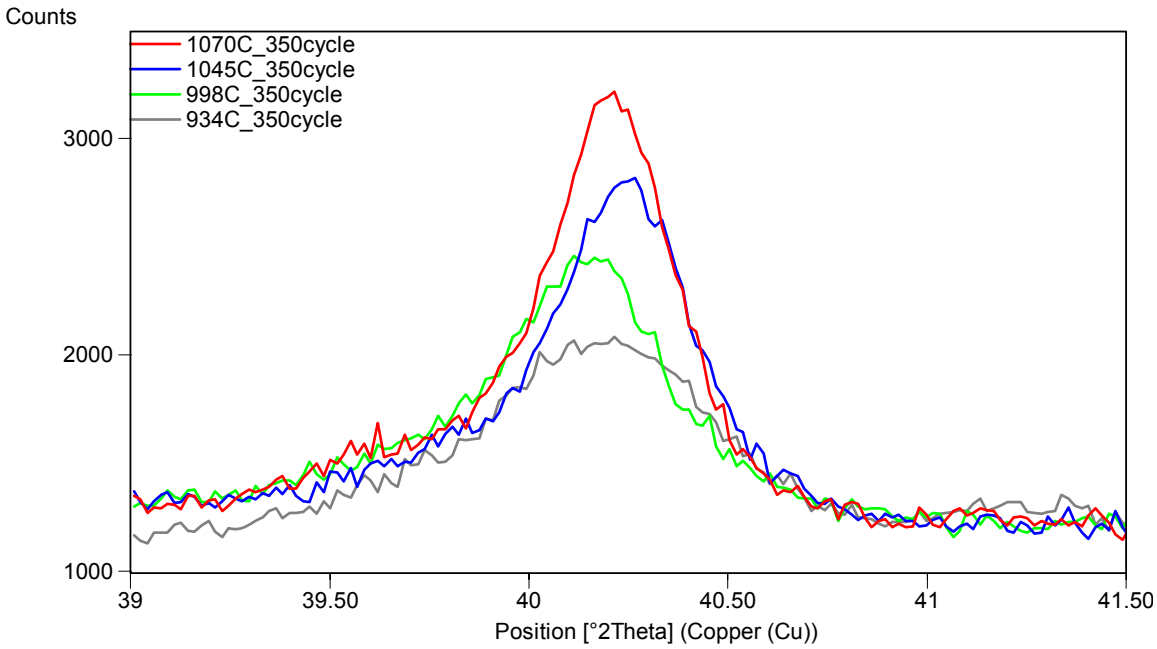

Figure 4.5.10 – XRD patterns indicate reduction in the FWHM of the Pt (111) peak with increasing aging temperature after aging for 350 cycles

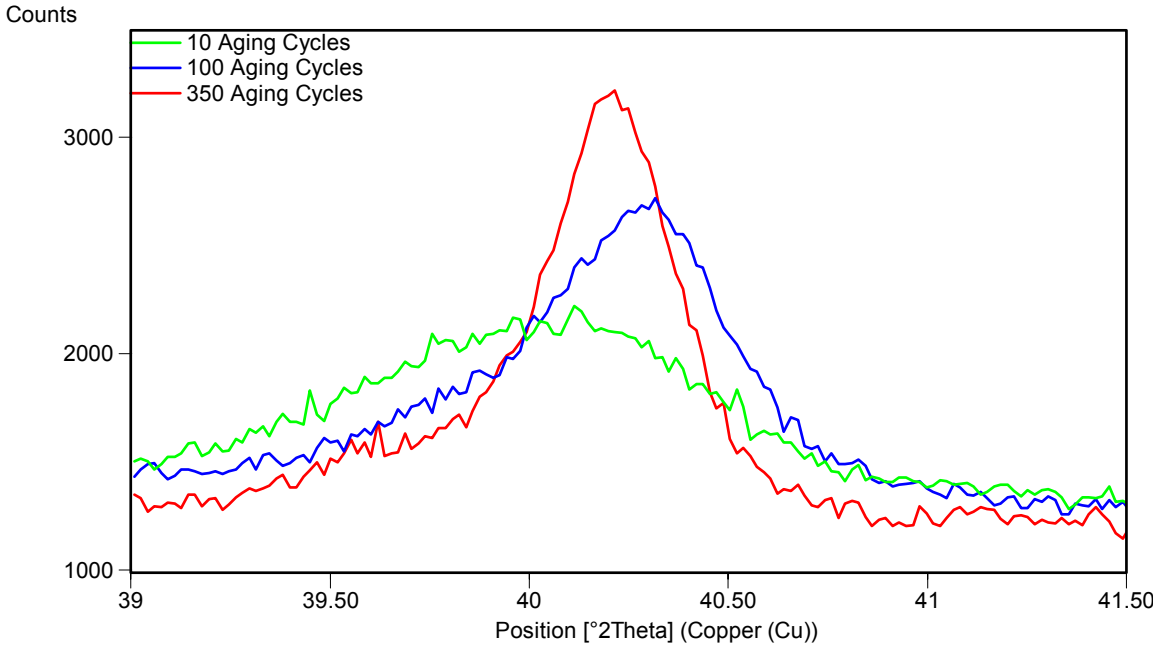

Figure 4.5.11 – Reduction in FWHM of Pt (111) peak as a result of aging at 1070°C for the indicated number of aging cycles

The results of the XRD analysis are listed in Table 4.5 and plotted in Figure 4.5.12. The average PGM particle size grows from a minimum measurable value of 7.4 nm after aging at 929^{o}C for 10 cycles to a maximum value of 24.7 nm after aging at 1070^{o}C for 350 cycles. Furthermore, it is clear that the PGM particle size growth is a function of both aging temperature and number of aging cycles. The average PGM particles sizes determined with XRD will next be compared to and complemented by those calculated with TEM.

The resolution of the TEM instrument is high enough to analyze the smallest particles on the fresh sample which is indiscernible with XRD. Figures 4.5.13 and 4.5.14 are high and low-resolution TEM micrographs of a fresh LNT, respectively. The low-resolution picture is useful in elucidating the morphology of the fresh LNT. As seen in the figure, the PGM particles are in a cluster supported by γ-Al_2O_3, with other components of the washcoat intermittently located near the PGM cluster. The high-resolution TEM micrograph is used for particle counting and statistical analysis. TEM experiments are also performed on the aged samples in order to validate the results from XRD; to determine the PGM particle size growth of the samples aged at 700 and 800^{o}C; and to obtain PGM particle size distributions. Figures 4.5.15 to 4.5.17 are a series of TEM micrographs with EDS results included to show the different morphologies and chemical compositions of the various catalyst components. The EDS results of Figure 4.5.15 clearly show that both of the PGM particles analyzed contain Pt, Pd, and Rh. Pt and Pd are seen in almost every EDS scan of a PGM particle, but Rh is more elusive, indicating that it is probably present in lower concentrations than Pt and Pd. In Figure 4.5.16 two large Ba “clumps” are identified with EDS, surrounded by Pt particles.

Table 4.5 – Average PGM particle size determined with XRD as a function of aging temperature and number of aging cycles

Aging Temperature	Number of Aging Cycles			
	10	100	300	350
843°C	7.4	11.1	11.2	
898 °C	7.4	13.2	12.5	
927 °C	7.4	13.0	13.5	
929 °C	7.4	13.2	14.1	
934 °C	9.4	13.9		14.5
998 °C	9.4	16.2		18.3
1045 °C	10.1	18.2		22.8
1070 °C	10.4	21.2		24.7

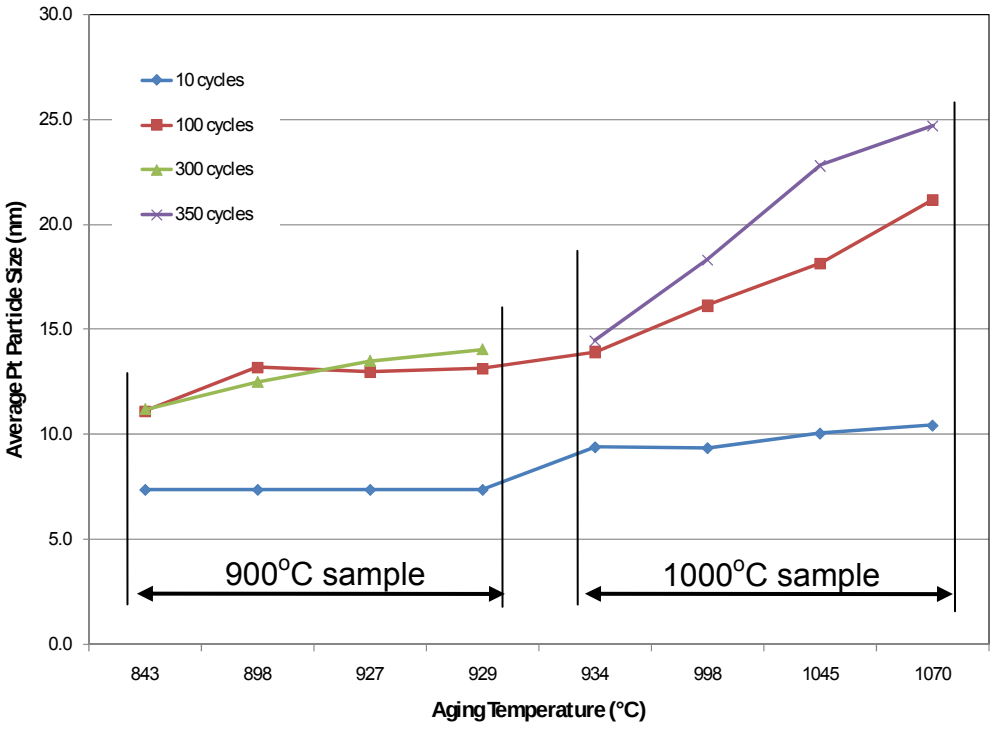

Figure 4.5.12 – PGM particle sizes determined from XRD patterns at aging temperatures of 900 and 1000°C

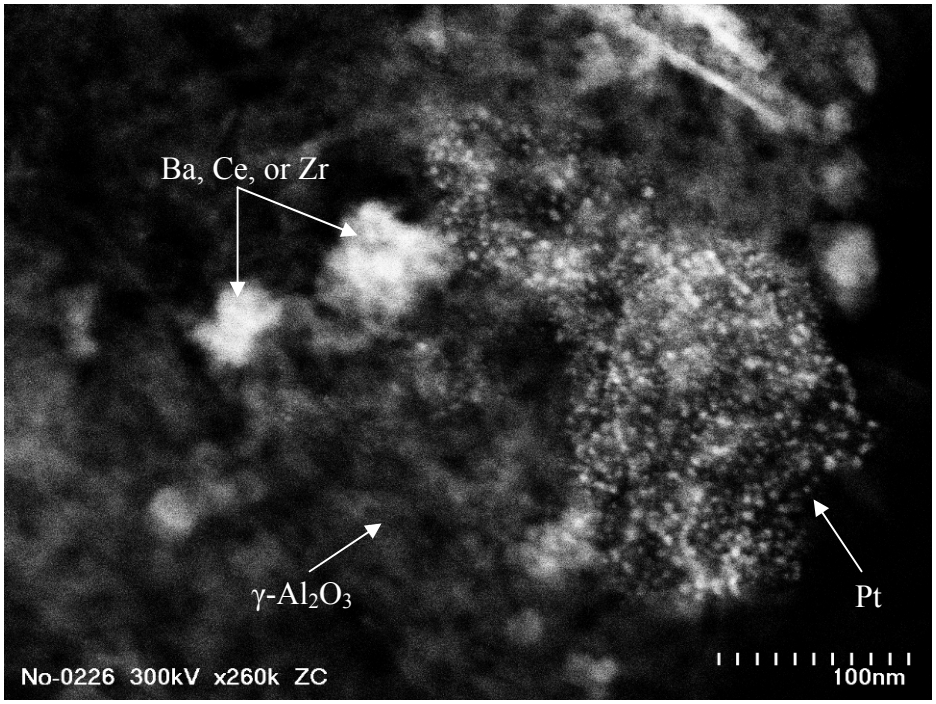

Figure 4.5.13 – Low-resolution TEM micrograph of fresh LNT. The cluster of fine PGM particles is clearly seen. The "cloud" is γ-Al_2O_3, and the irregular, bright, white areas are Ba, Ce, and Zr.

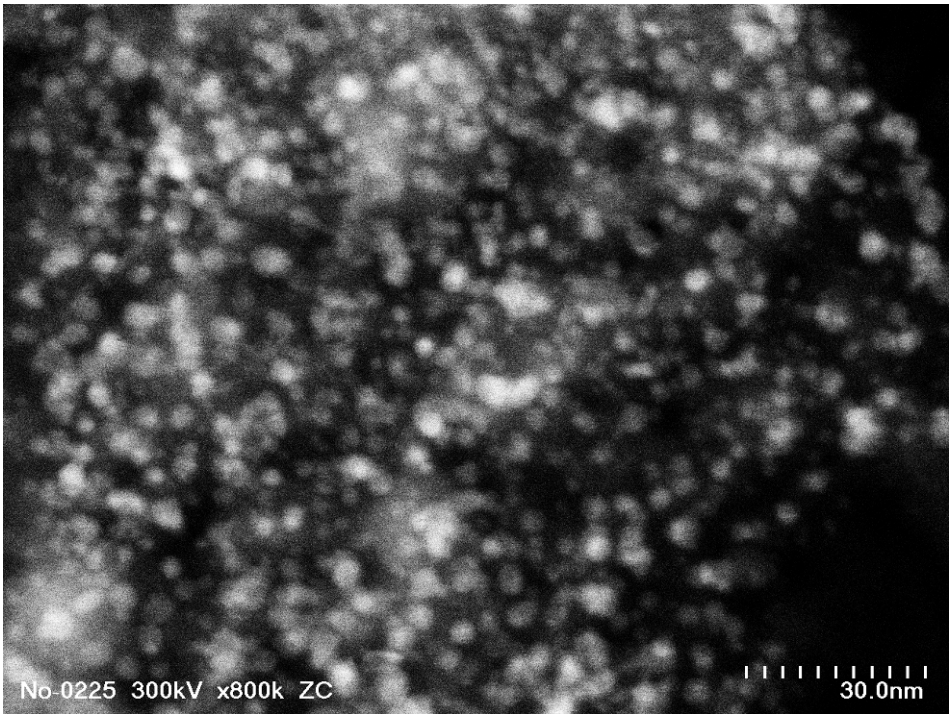

Figure 4.5.14 – High-resolution TEM micrograph of fresh LNT. The bright white spots are PGM particles.

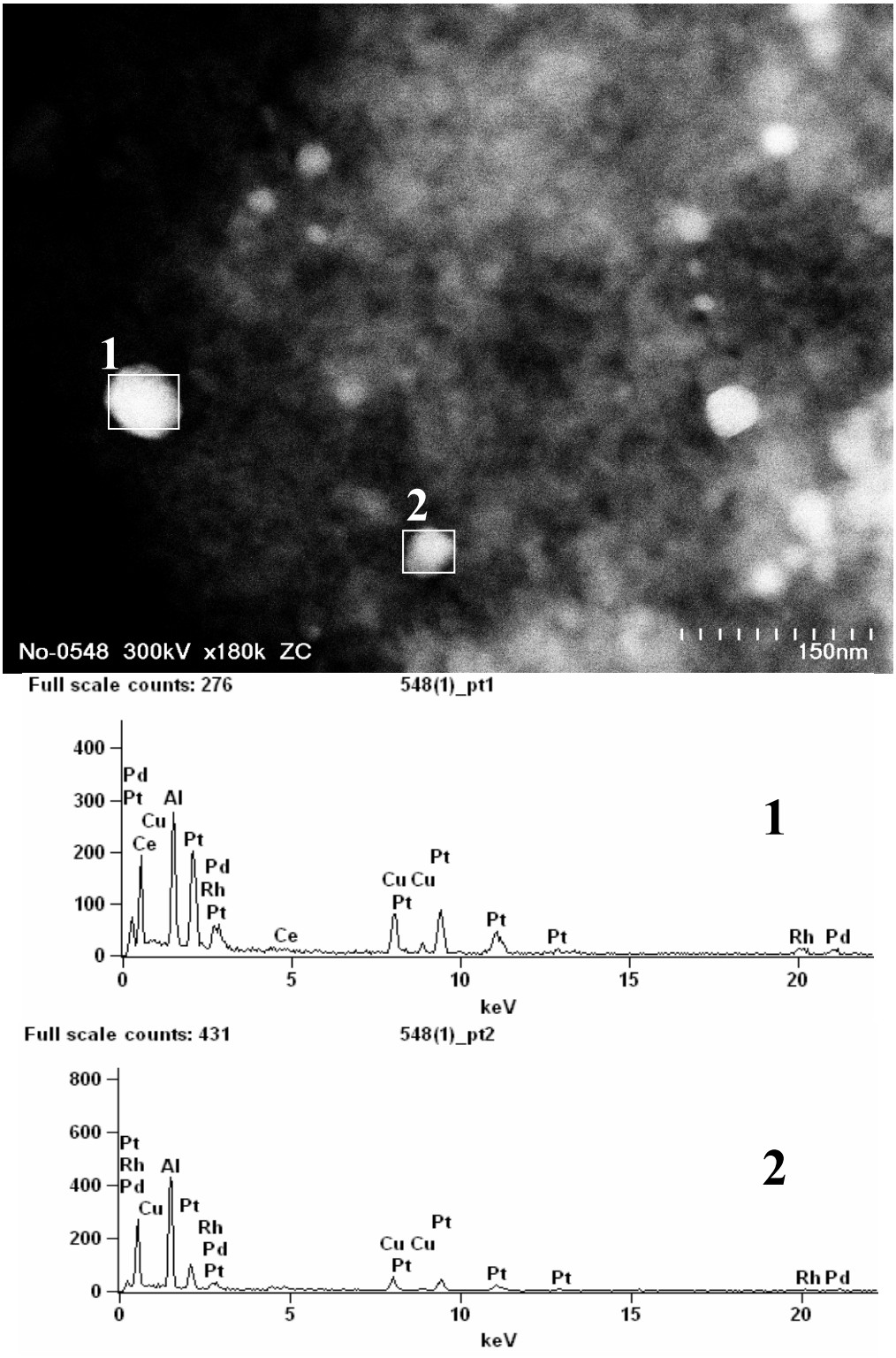

4.5.15 – TEM micrograph and EDS results of a LNT aged at 929°C for 100 cycles indicate that Pt, Pd, and Rh are all present in this LNT

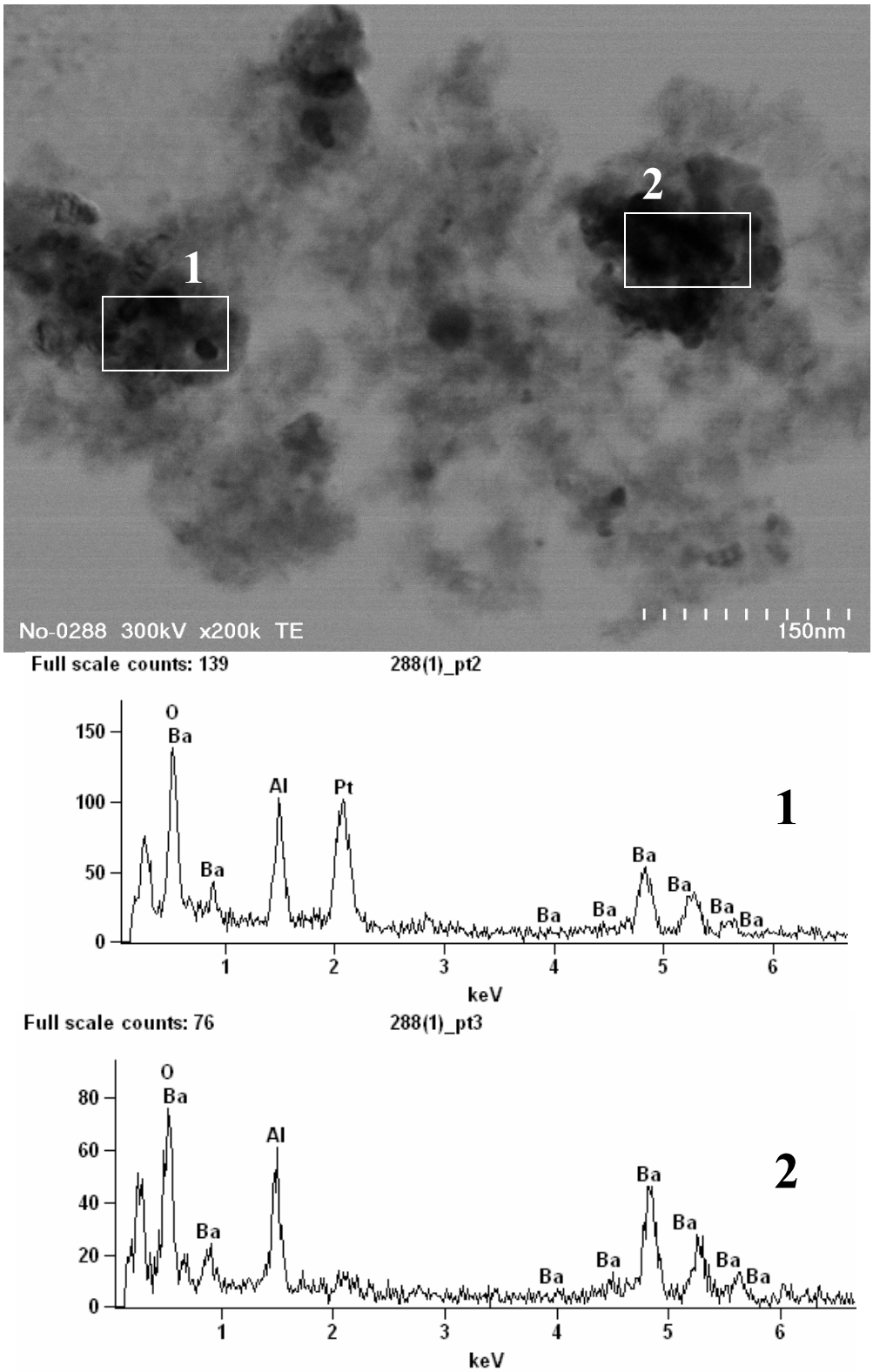

4.5.16 – TEM micrograph and EDS results of a LNT aged at 929°C for 300 cycles show the different morphologies of Ba. The small PGM particle in the bottom right corner of area 1 gives rise to the Pt peak.

Clearly, PGM particles can not be mistaken for Ba. Figure 4.5.17 is a dark Z-contrast image of a sample aged at 1070^{o}C for 350 cycles. The Ce and PGM identified with EDS both appear bright in the TEM micrograph because both have high atomic numbers. However, The PGM can be clearly identified because of its consistent circular shape in comparison to the irregular shape of Ce.

Figures 4.5.18 and 4.5.19 are PGM particle size distributions of a fresh LNT and a LNT aged at 1070^{o}C for 350 cycles, respectively. The particle size distribution of the fresh sample resembles a Gaussian distribution and has a standard deviation of only 0.7 nm. In contrast, the distribution for the aged sample has a standard deviation of 15 nm and is positively skewed, with some particles growing to diameters greater than 60 nm. The PGM particle sizes determined from the TEM micrographs are listed in Table 4.6 and shown in Figure 4.5.20, and it is clearly evident that Pt particle growth begins after aging at 700^{o}C for 100 cycles and continues to increase as the aging temperature and number of aging cycles increase.

The results obtained with TEM for the LNT samples aged at 900 and 1000^{o}C are compared to those obtained with XRD pattern analysis in Figure 4.5.21. The difference bars are calculated by subtracting the particle size determined with XRD from that determined with TEM. The results from the two techniques are shown to corroborate each other with larger differences in calculated PGM particles sizes at the lower aging temperature of 929^{o}C. For example, after aging at 929^{o}C for 300 cycles, average Pt particle sizes of 14.1 and 17.8 nm are calculated with XRD and TEM, respectively. On the other hand, after aging at 1070^{o}C for 350 cycles, average PGM particle sizes of 24.7 and 26 nm are calculated with XRD and TEM, respectively.

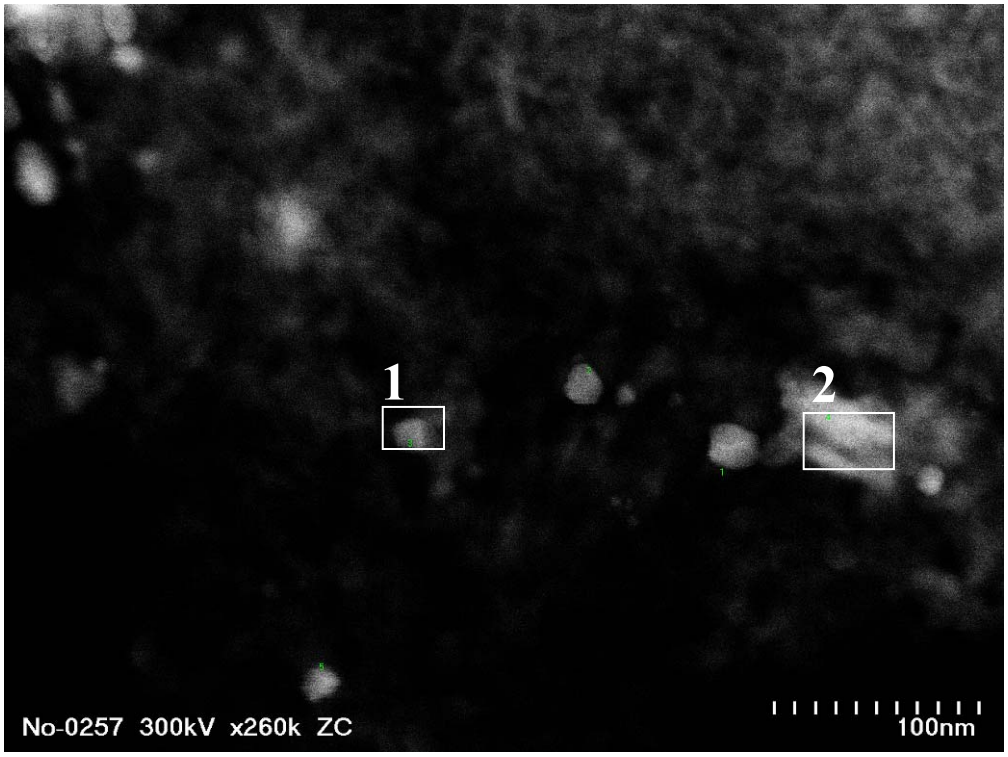

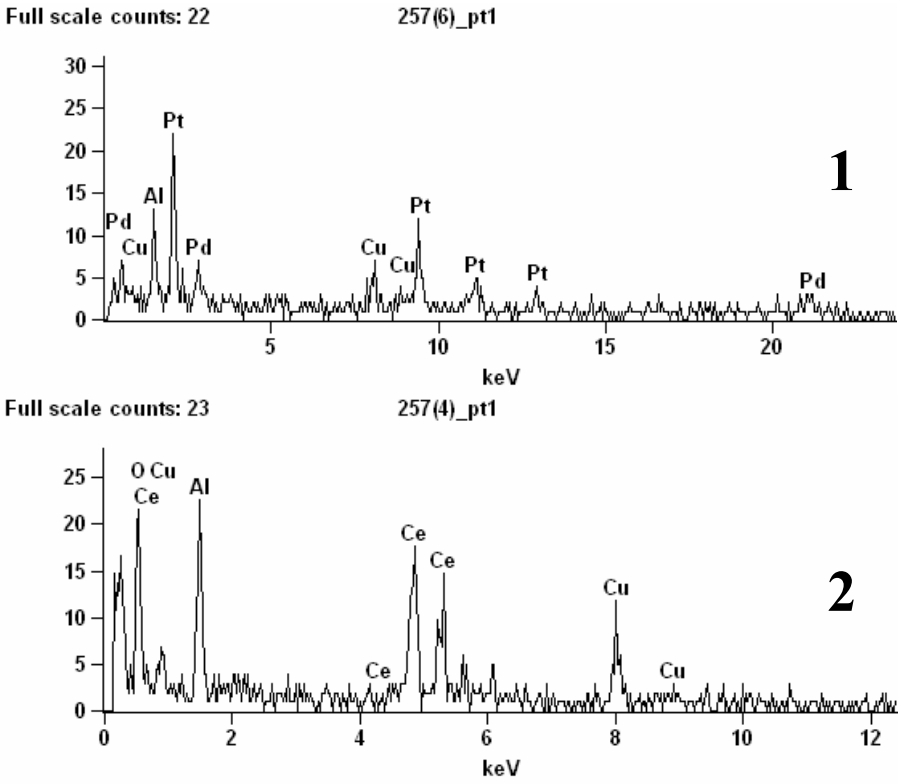

4.5.17 –TEM micrograph and EDS results of a LNT aged at 1070°C for 300 cycles indicate the different morphologies of Pt and Ce.

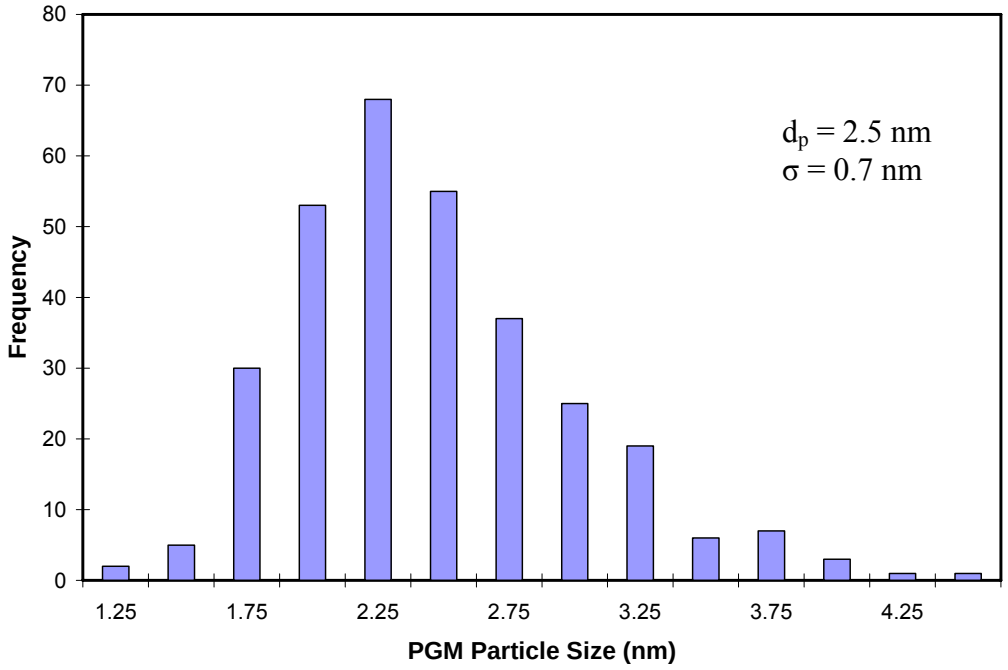

Figure 4.5.18 – PGM particle size distribution of fresh LNT

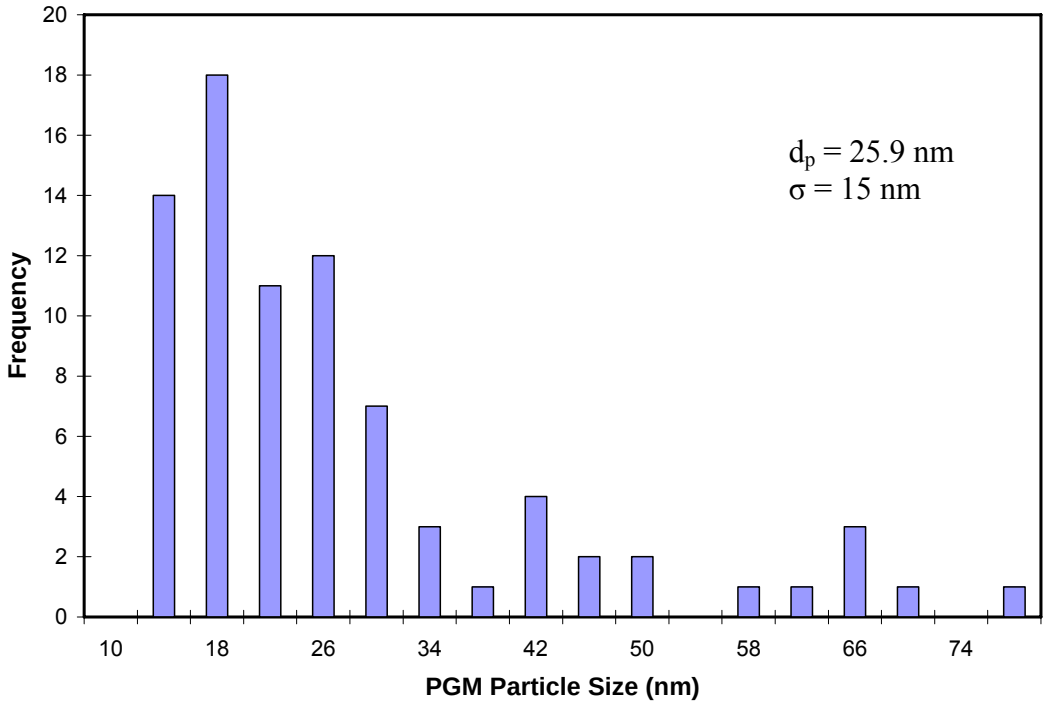

Figure 4.5.19 – PGM particle size distribution of LNT aged at 1070°C for 350 cycles

Table 4.6 – Average PGM particle size and statistics determined with TEM as a function of aging temperature and number of aging cycles

Aging Temperature (^{o}C)	Number of Aging Cycles	Average Particle Size (nm)	Standard Deviation (nm)	Skewness	Number of Particles Counted
Fresh	-	2.5	0.7	0.101	586
754	100	6.5	1.9	0.46	180
754	200	7.6	1.6	0.462	127
883	100	11.5	4.1	0.822	210
883	200	12.7	3	0.434	199
929	100	10.5	3.8	0.784	230
929	300	17.7	6.7	1.06	107
1070	100	23.1	11	0.763	191
1070	350	25.9	15	1.54	82

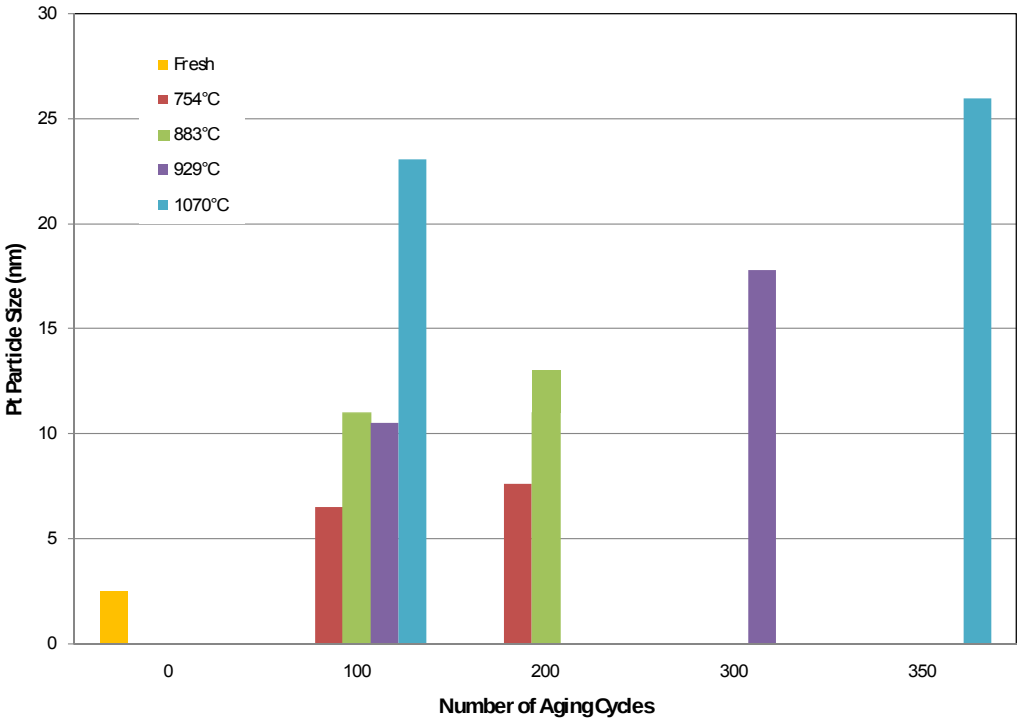

Figure 4.5.20 – TEM PGM particle size results

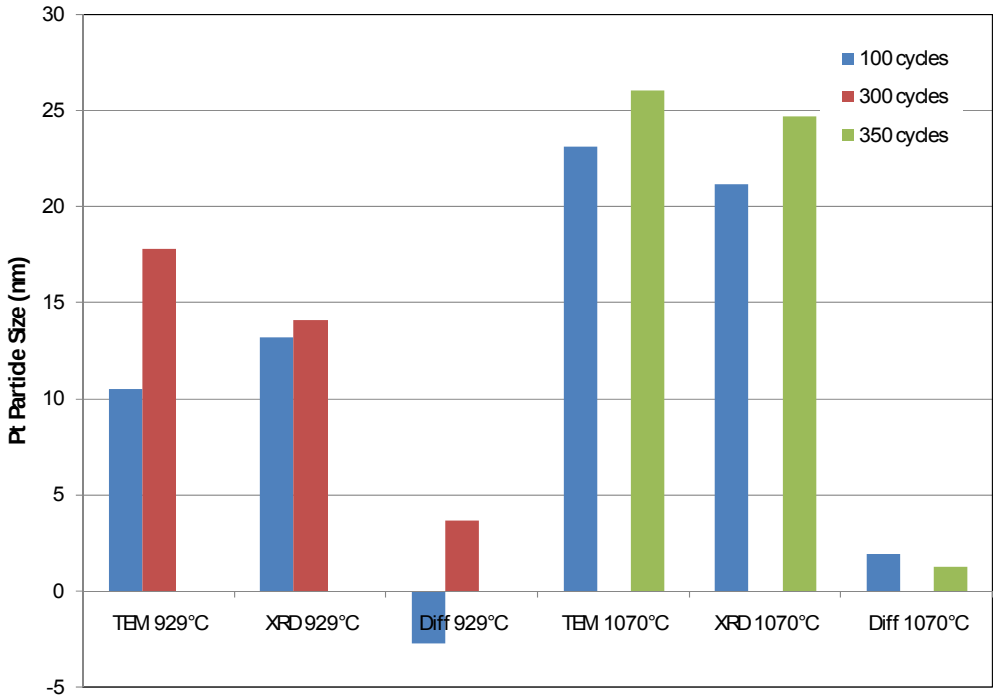

Figure 4.5.21 – Comparison of average PGM particle sizes obtained with XRD and TEM. Particle sizes from TEM micrograph analysis are slightly larger than those calculated from XRD patterns.

Taking the particle size determined with TEM to be the true value, there is a 20% and a 5% difference in particle sizes determined after aging at 929°C for 300 cycles and 1070°C for 350 cycles, respectively.

The XRD and TEM PGM particle growth results agree well with those previously reported in the literature by Kim and Nagai et al. [41, 43]. Kim et al. reported that Pt particles originally 2.5 nm in diameter in a fresh sample grew to diameters of 11, 17, and 34 nm after calcining for 17 hours in O_2 at 700, 800, and 900°C, respectively. These diameters are slightly higher than the ones obtained in this study, but the catalysts used by Kim et al. in their study were model catalysts without any additives and the calcination times were much longer. It is possible that calcinations at a given temperature result in more severe Pt particle size growth than cyclic aging at the same temperature. It

is also extremely likely that the cerium and cerium zirconium mixed oxide additives used in this fully-formulated LNT helped stabilize the PGM and reduced the amount of sintering.

The reported growth in PGM particle size has been shown to negatively impact the performance of LNTs [36-41]. As a result of PGM particle sintering, the precious metal surface area necessary for the oxidation of NO to NO_2 in the lean phase—a precursor for the formation of stored nitrites and nitrates—and the reduction of released NO_x in the rich phase, is reduced considerably, resulting in the degradation in NO_x performance of aged LNTs. However, it is no simple matter to quantify the effect that PGM particle growth has on NO_x conversion in the present study. However, the NO_x conversion figures presented in Section 4.4 apparently indicate that the growth of PGM particles to approximately 13 nm in diameter observed after aging at 700 and 800^oC has a minimal effect on the LNT's NO_x conversion, but it is difficult to determine the effect that further growth after aging at 900 and 1000^oC has on NO_x conversion without modeling. A statistical analysis performed using linear regression which will attempt to clarify the relationship between PGM particle size growth and reduction in NO_x conversion is presented in Section 4.6.

4.5.3 – XRD Analysis of Ba Phase Change

XRD patterns are used to determine the effect of high-temperature physicochemical changes of Ba—the NO_x storage medium. Despite the large number of studies which have reported the formation of $BaAl_2O_4$ at high temperatures in

Pt/Ba/Al_2O_3 or Ba/Al_2O_3 catalysts [40, 48-52], no evidence of $BaAl_2O_4$ formation as a result of aging has been found in the present study. Even after aging at 1070°C for 350 cycles, there is no growth of any of the characteristic $BaAl_2O_4$ XRD peaks located at 2θ = 19.60, 28.20, and 34.30°. Figure 4.5.22 is a set of high-intensity XRD scans of the 2θ = 19.60 peak, the most easily resolved of the $BaAl_2O_4$ peaks, of a fresh sample and four samples aged for 350 cycles at different aging temperatures. The enhanced resolution is attained by counting at each 2θ step for four times longer than the other XRD patterns presented up to this point. Clearly, in comparison to the full-scale $BaCO_3$ peak of the fresh sample and typical $BaAl_2O_4$ peak shapes found in the literature [40, 48-52], there is no growth of the $BaAl_2O_4$ peak. This is in direct contrast to a very similar study by Nguyen et al. in which the researchers saw $BaAl_2O_4$ formation after cyclic aginga model "Ba+K" LNT at a nominal aging temperature of 1000°C [40]. The formulation of the LNT used in this study is different than that used by Nguyen et al. and, thus it is assumed that the additives in this fully-formulated LNT stabilize the Ba. The presence of trace amounts of $BaAl_2O_4$ even in the fresh sample raises the possibility that the LNT is either initially loaded with a small amount of $BaAl_2O_4$, or that $BaAl_2O_4$ is formed during the calcination of the LNT—a necessary step in the catalyst production process.

The conclusion that the Ba does not change phase to $BaAl_2O_4$ necessarily raises the question of what is happening to the Ba. From Figure 4.5.23 it is clear that after aging at 884°C for 10 cycles the $BaCO_3$ phase has either disappeared or is no longer visible with XRD since there is no growth of any other Ba-containing phase such as BaO or BaOH.

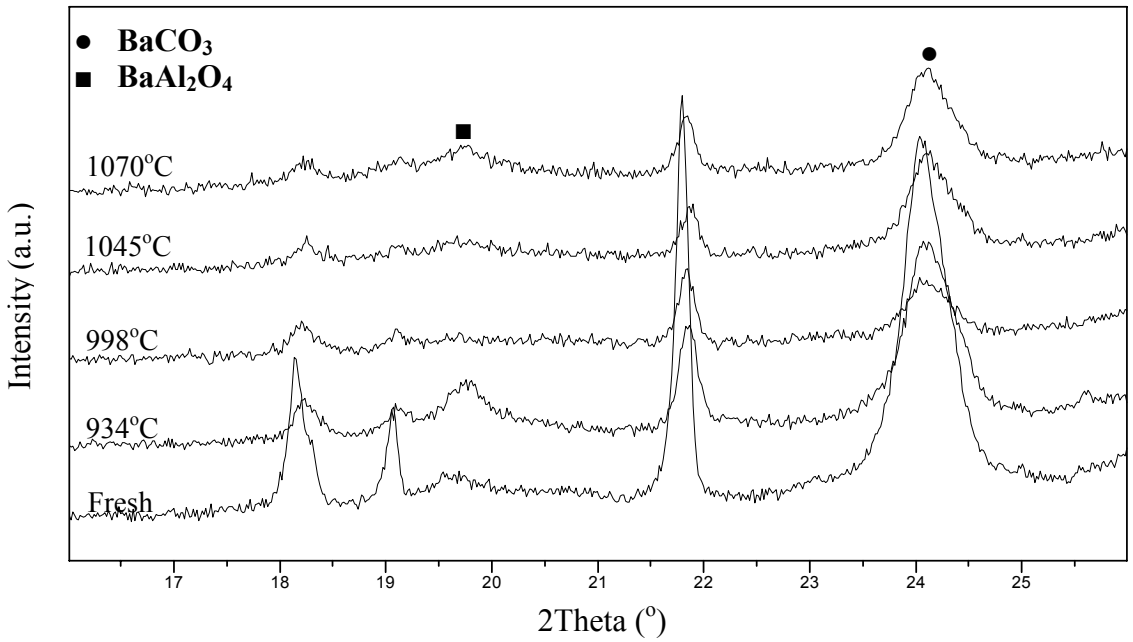

Figure 4.5.22 – High-intensity XRD patterns compare the $BaCO_3$ and $BaAl_2O_4$ peaks of fresh LNT to LNTs aged for 350 cycles at the indicated temperatures

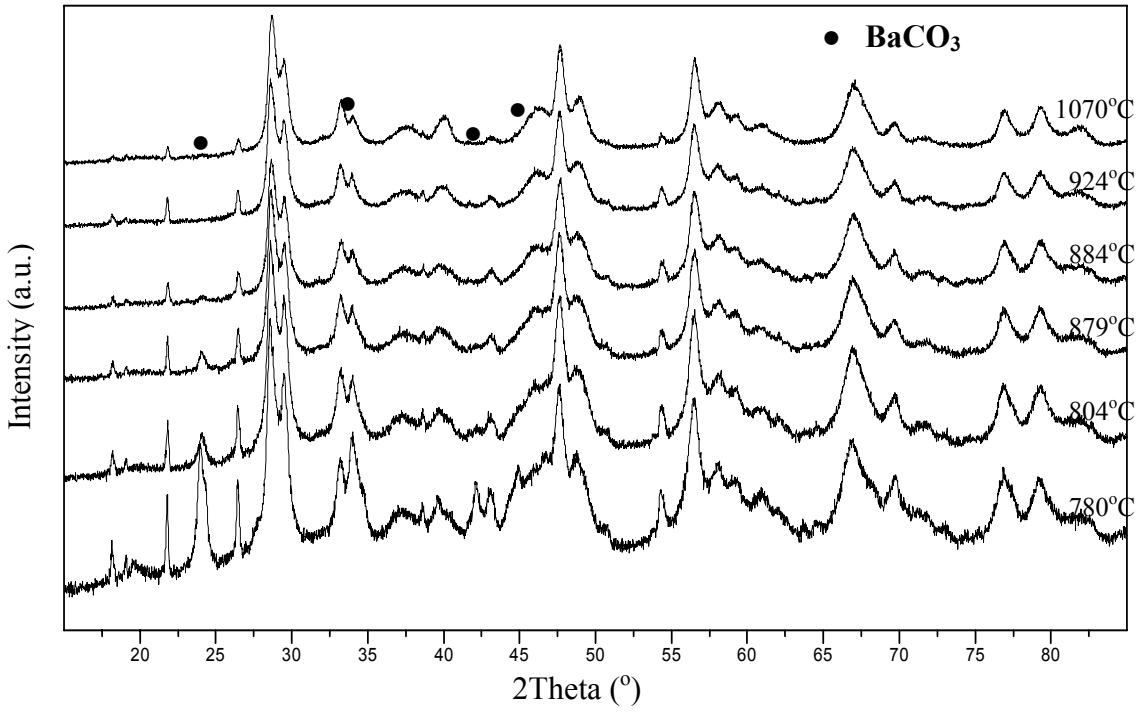

Figure 4.5.23 – Full-scale XRD patterns of samples aged for 10 cycles at the indicated temperatures indicate the disappearance of crystalline $BaCO_3$ after aging at temperatures above 884°C

Prior to every XRD experiment the catalysts are pretreated in 5% CO_2 and Ar overnight at 250^{o}C in order to drive all Ba to $BaCO_3$, so it is not expected that there would be any BaO or BaOH present on the samples. On the other hand, as seen in Figure 4.5.24, the $BaCO_3$ phase is still present in the rear section of the sample aged at a nominal aging temperature of 934^{o}C for 10cycles. This indicates that the disappearance of the $BaCO_3$ phase occurs over a range of temperatures, but it doesn't help to explain what's happening to the Ba. The possibility that the Ba is somehow disappearing is ruled out by EPMA Ba elemental maps and line scans previously presented that measured no change in the Ba concentration with high temperature aging. The most likely supposition is that $BaCO_3$ has transitioned from a crystalline structure to an amorphous structure through a process of vitrification. Though no publications have been found which propose that such a transformation occurs with thermal aging, vitrification, the process of converting a material with a crystalline structure to one with an amorphous structure, is usually achieved by heating to temperatures beyond the materials melting point; the melting point of $BaCO_3$ is 811^{o}C.

Even though no literature corroborates the proposed transition, there have been studies which have compared the NO_x storage behavior of crystalline and amorphous Ba phases [23, 24]. Piacentini et al. noticed that amorphous barium nitrates in intimate contact with the Al_2O_3 support are not as thermally stable as nitrates formed on crystalline Ba [23, 24]. They proposed that amorphous Ba is not suitable for NO_x storage at temperatures above 300-350^{o}C. However, because substantial NO_x storage is still observed while evaluating at 400^{o}C after the $BaCO_3$ phase has disappeared from XRD

patterns, the XRD amorphous Ba phase appears to still be a good storage media. Or, it could be that the quantity of remaining crystalline Ba sites in the rear-half of the LNT seen in Figure 4.5.24 are sufficient for NO_x storage, since it is generally accepted that only a portion of the Ba sites participate in NO_x storage [9, 22]. However, the temperature exotherms during evaluation do not increase in the rear-half of the LNT with increasing number of aging cycles as would be expected if NO_x reduction has shifted to the rear-half of the LNT.

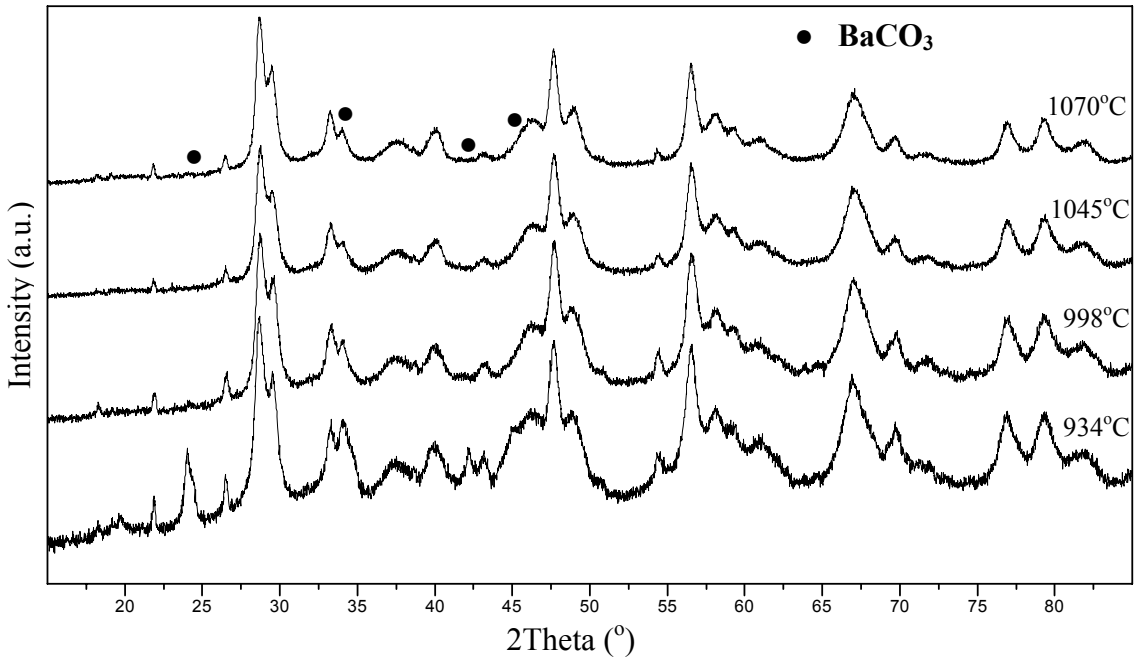

Figure 4.5.24 – Full-scale XRD patterns of samples aged for 10 cycles at the indicated temperatures indicate that crystalline $BaCO_3$ exists in the rear-half of LNTs aged at temperatures above 900°C

4.5.3 – BET Surface Area

The LNT washcoat's high surface area γ-Al_2O_3 support is critical because the rate of NO_x storage and reduction is dependent on the number of exposed Ba-storage and Pt sites, which in turn is a function of the surface area. However, high temperature aging is known to negatively impact the surface area of the γ-Al_2O_3 support [40, 47-50]. For this reason, BET surface area measurements are used to quantify the effect of aging on the LNT's surface area. The measurements reveal that surface area is a function of both aging temperature and number of aging cycles. Presented in Figure 4.5.25 and listed in Table 4.7, the results indicate that the fresh LNT sample has a BET calculated surface area of 36 m^2/g of catalyst (washcoat + cordierite), whereas the sample aged at 1070°C for 350 cycles has a surface area of only 19 m^2/g of catalyst. Other samples aged at temperatures below 1070°C or at 1070°C for fewer than 350 cycles have surface areas somewhere in between these two extremes.

Table 4.7 – BET surface area measurements of fresh and aged LNTs

Aging Temperature	**Number of Aging Cycles**					
	0	**10**	**100**	**200**	**300**	**350**
Fresh	36					
754ºC	36	35	37	31		
883ºC	36	37	34	29		
929ºC	36	25	25		20	
1070ºC	36	23	22			19

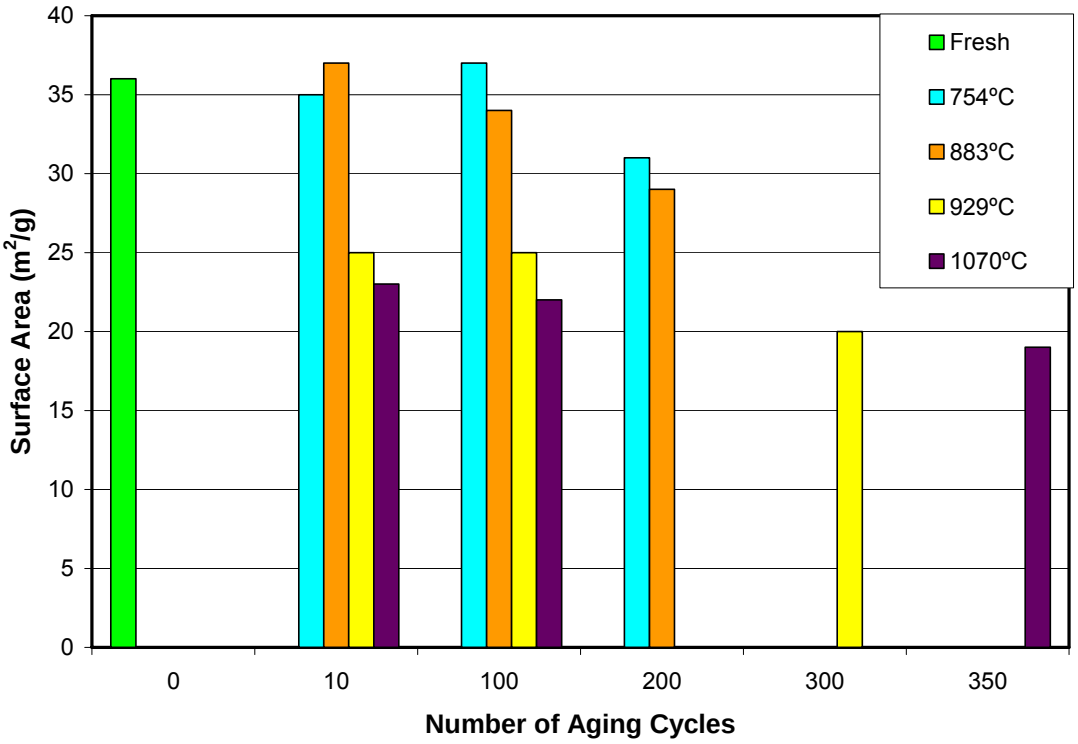

Figure 4.5.25 – BET surface area measurements of fresh and aged LNTs

The reductions in surface area as a result of high temperature aging determined in this study are not as severe as those reported in a previous study by Nguyen et al. The researchers in that study reported a reduction in total surface area (cordierite + washcoat) from 28 to 17 m^2/g after aging in an engine at 800°C for 48 cycles using long cycles consisting of a 120 s rich phase. In the present study, the reduction in surface area after aging at 800°C for 200 cycles (with a rich phase exotherm duration of only 85 s) was only 7 m^2/g. This may be because temperatures are much harder to control in engine experiments, and the engine aged LNTs may have actually experienced higher temperatures than the bench-flow reactor aged LNTs. However, the smaller surface area

loss in this study may also be a result of the γ-Al_2O_3 stabilizing additives such as Ce and La used in this LNT.

Though it is difficult without extensive modeling to accurately quantify the effect that any given deactivation mechanism has on the NO_x conversion, it is believed in this study that the reduction in surface area is a major cause of the reduction in NO_x conversion after aging at high temperatures, especially when evaluating at 400°C. Figures 4.5.26 to 4.5.28 are side-by-side comparisons of the decrease in surface area to the decrease in NO_x conversion at 200, 300, and 400°C, respectively. These comparisons will be further analyzed in the following section in which correlations between NO_x conversion, surface area, and PGM particle size are derived.

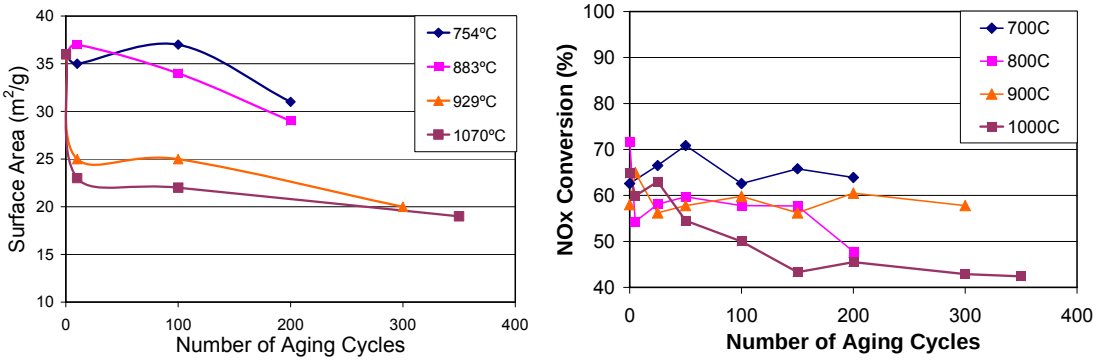

Figure 4.5.26 – Comparison of BET surface area measurements to NO_x conversion at 200°C after aging

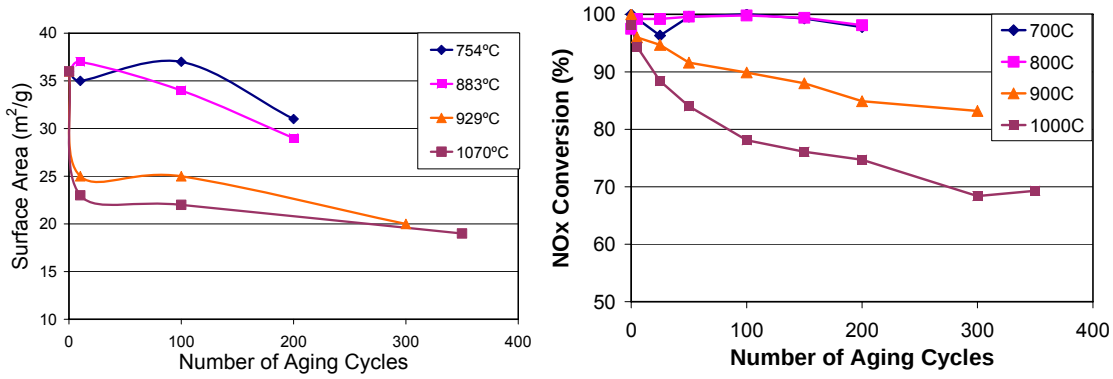

Figure 4.5.27 – Comparison of BET surface area measurements to NO_x conversion at 300°C after aging

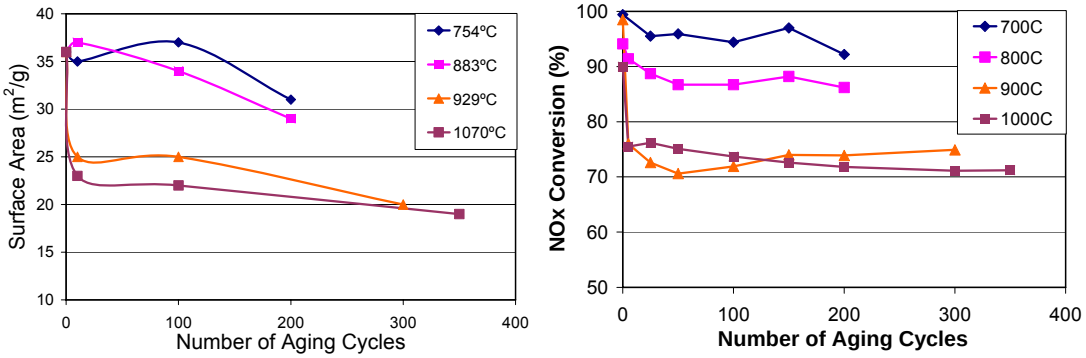

Figure 4.5.28 – Comparison of BET surface area measurements to NO_x conversion at 400°C after aging

4.6 – Correlations between Reduction in NO_x Conversion, PGM Particle Size Growth, and Surface Area Reduction

As previously mentioned, it is extremely difficult to precisely determine the cause of reductions in NO_x conversion without extensive modeling because of the simultaneous morphological changes just discussed. However, statistics can be used to correlate NO_x conversion and washcoat degradation in the form of PGM sintering and surface area reduction. Scatterplots of NO_x conversion verse both surface area and PGM size are presented below in Figures 4.6.1 to 4.6.12. The red density ellipses surrounding the data points are used to qualitatively show correlations. Thinner, diagonally oriented ellipses indicate a strong correlation, while circular ellipses indicate that the variables are uncorrelated.

Before analyzing the scatterplots or presenting any quantitative data, it is a good idea to outline what is expected. As seen in the NO_x conversion figures, there is little degradation at lower aging temperatures, with the exception being evaluations at 400^{o}C, where a slight decrease is observed with increasing number of aging cycles. Thus, any correlations when aging at 700 or 800^{o}C while evaluating at 200 or 300^{o}C simply indicate that neither the NO_x conversion nor the material properties are changing. However, at higher aging temperatures, and when evaluating at 400^{o}C after aging at 700 or 800^{o}C, strong correlations will be used to indicate that NO_x conversion and whatever material effect correlates well are strongly related. One last word of caution before beginning: correlation does not equal causation.

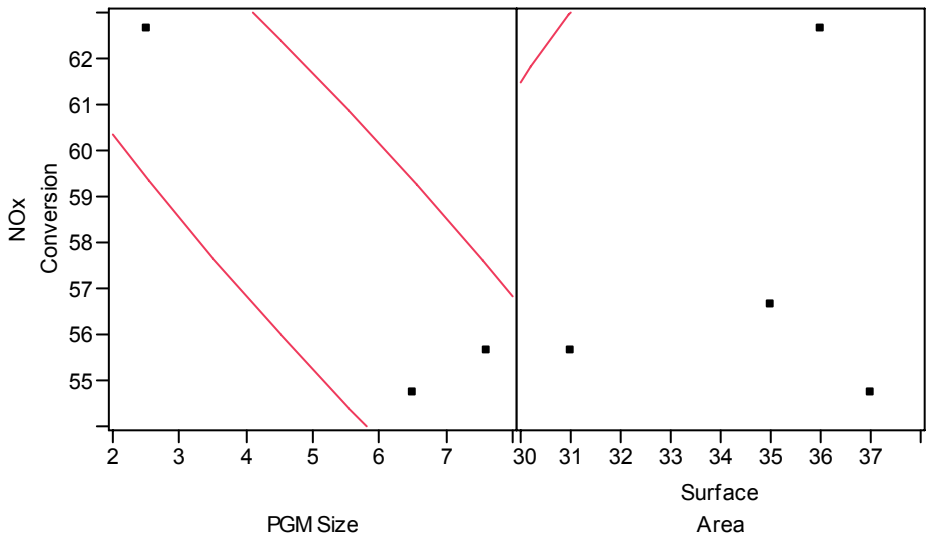

Figure 4.6.1 – Scatterplot matrix at an aging temperature of 700°C and an evaluation temperature of 200°C

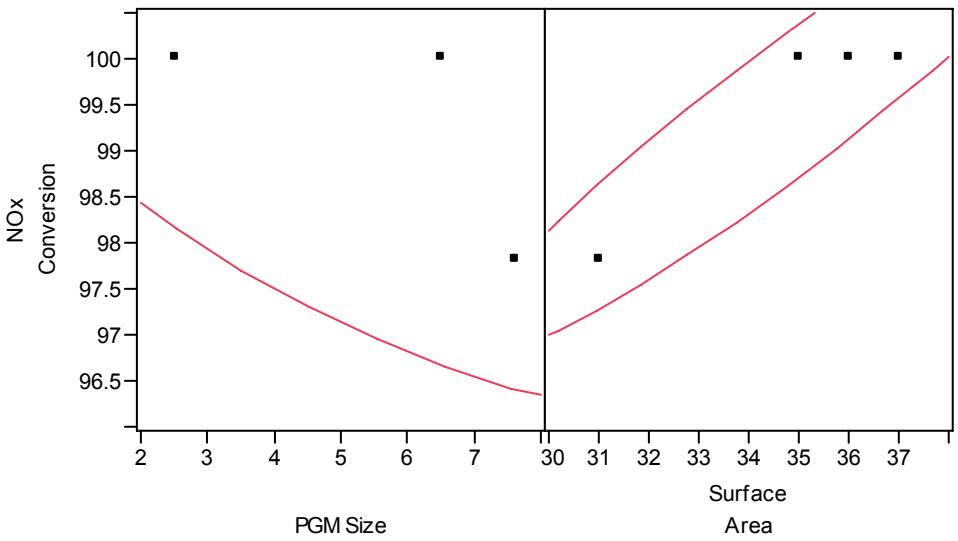

Figure 4.6.2 – Scatterplot matrix at an aging temperature of 700°C and an evaluation temperature of 300°C

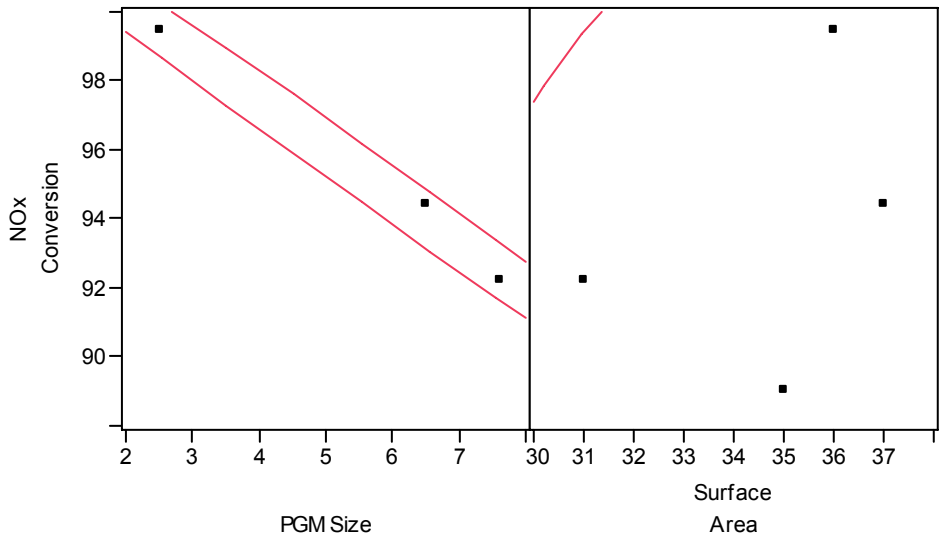

Figure 4.6.3 – Scatterplot matrix at an aging temperature of 700°C and an evaluation temperature of 400°C

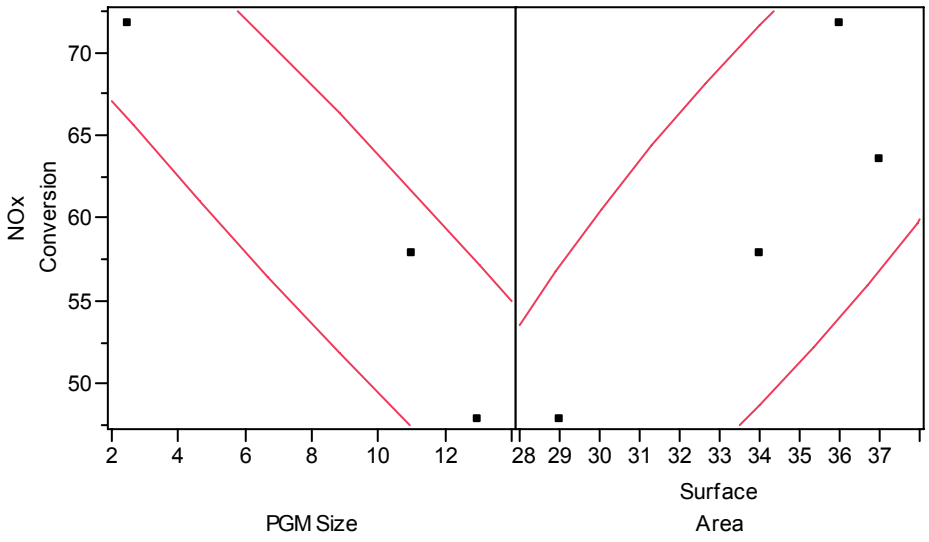

Figure 4.6.4 –Scatterplot matrix at an aging temperature of 800°C and an evaluation temperature of 200°C

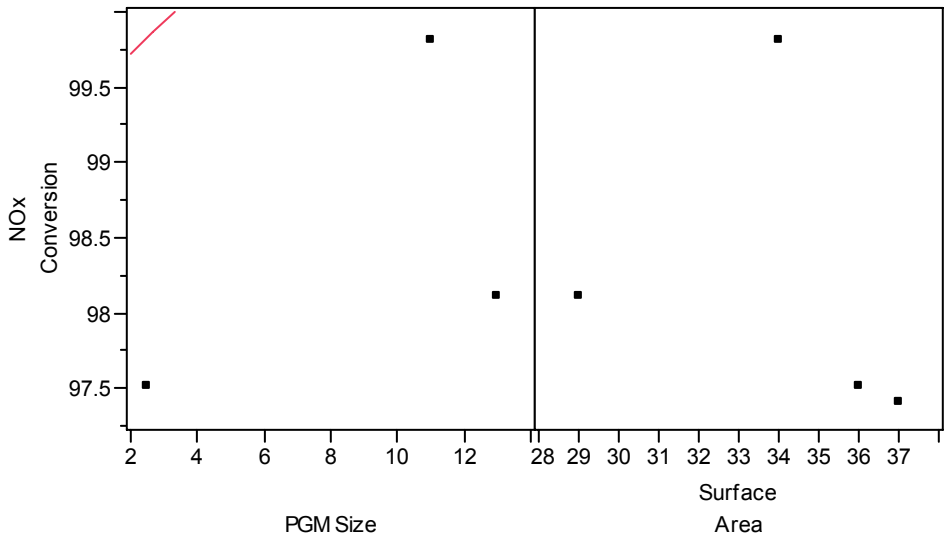

Figure 4.6.5 – Scatterplot matrix at an aging temperature of 800°C and an evaluation temperature of 300°C

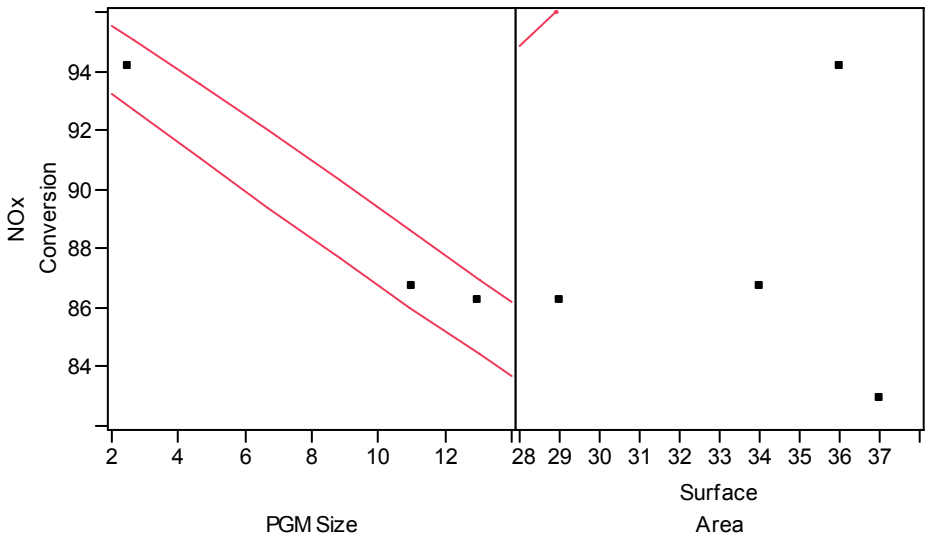

Figure 4.6.6 – Scatterplot matrix at an aging temperature of 800°C and an evaluation temperature of 400°C

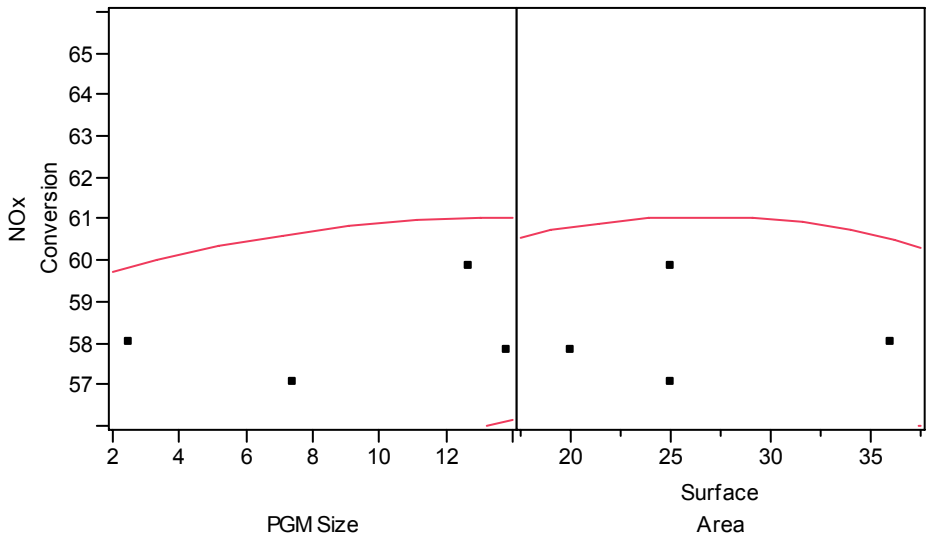

Figure 4.6.7 – Scatterplot matrix at an aging temperature of 900°C and an evaluation temperature of 200°C

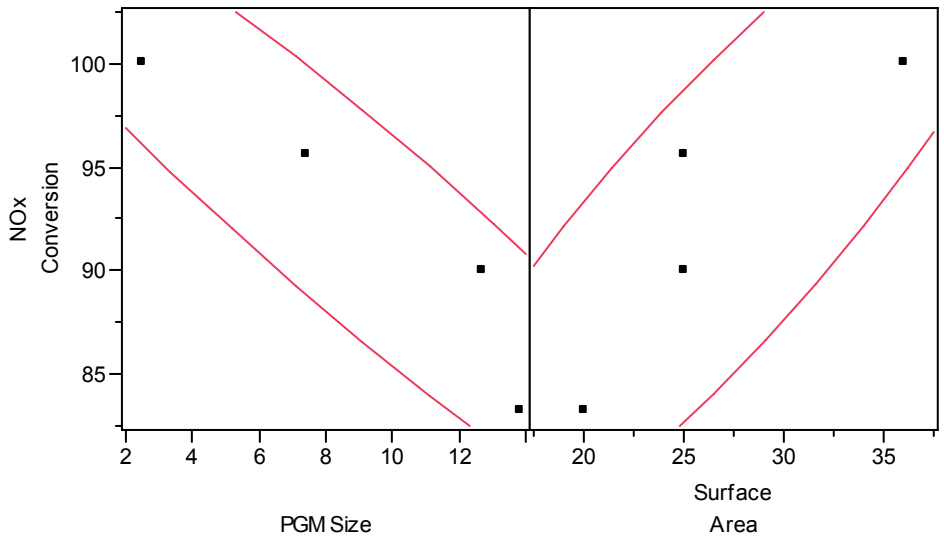

Figure 4.6.8 – Scatterplot matrix at an aging temperature of 900°C and an evaluation temperature of 300°C

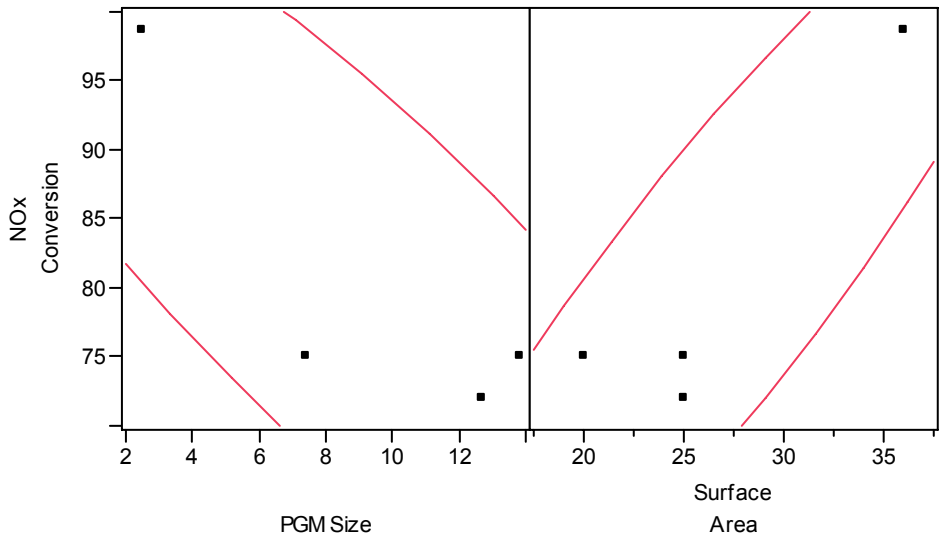

Figure 4.6.9 – Scatterplot matrix at an aging temperature of 900°C and an evaluation temperature of 400°C

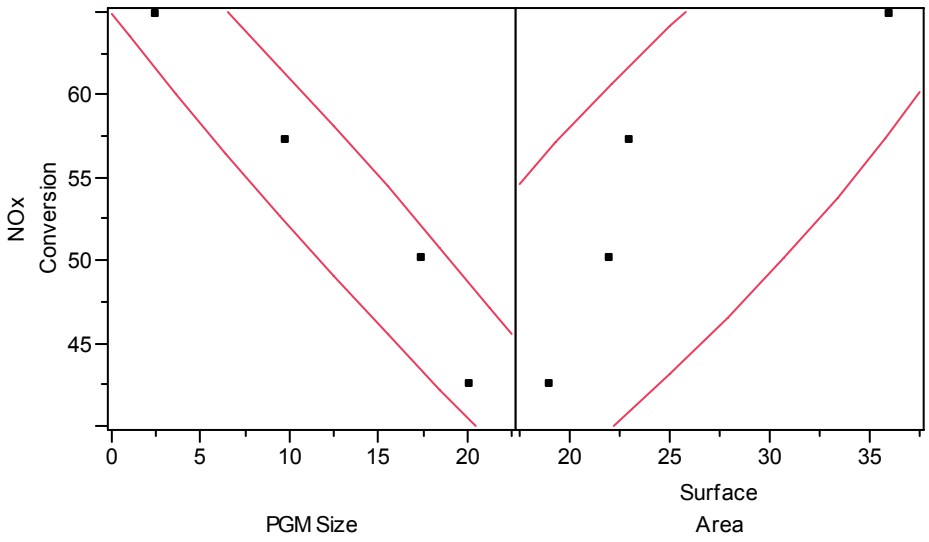

Figure 4.6.10 – Scatterplot matrix at an aging temperature of 1000°C and an evaluation temperature of 200°C

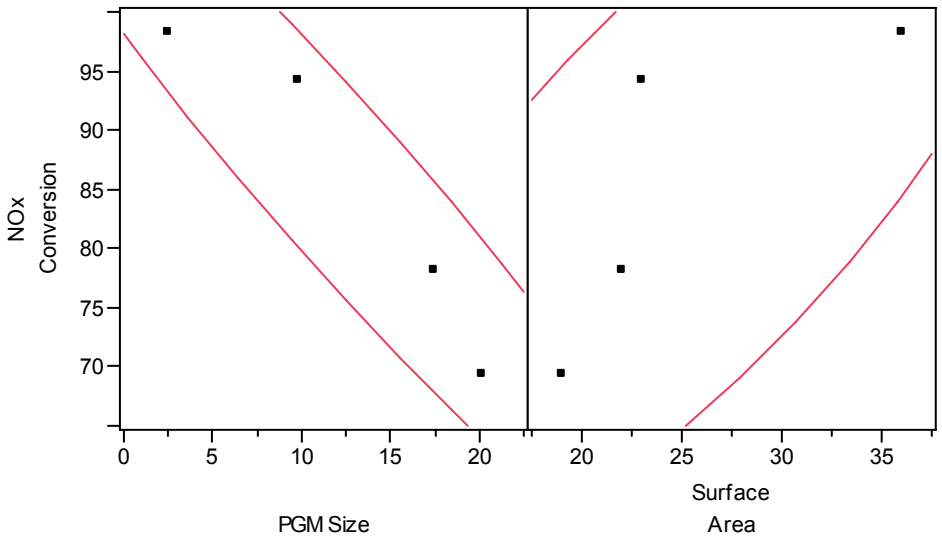

Figure 4.6.11 – Scatterplot matrix at an aging temperature of 1000°C and an evaluation temperature of 300°C

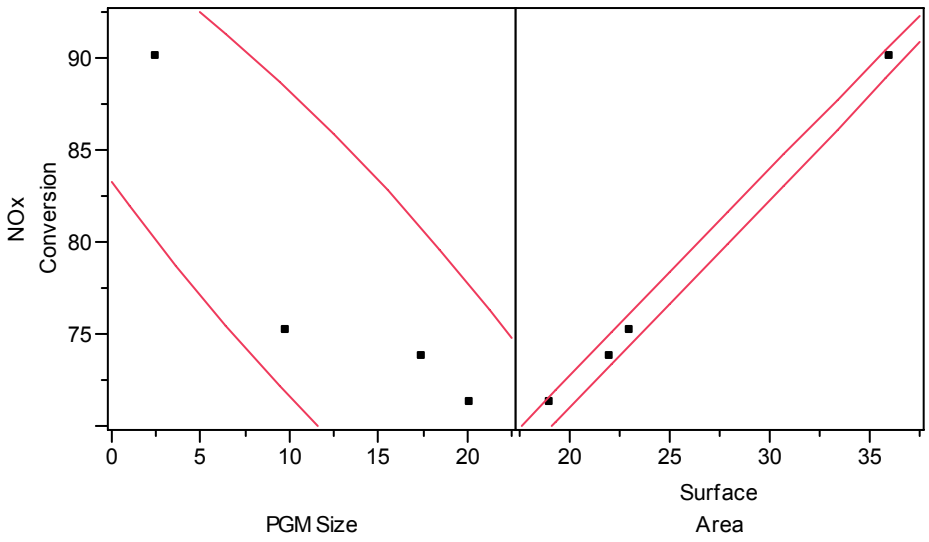

Figure 4.6.12 – Scatterplot matrix at an aging temperature of 1000°C and an evaluation temperature of 400°C

The scatterplots just presented show some very interesting correlations. Firstly, PGM sintering correlates well with reductions in NO_x conversion when evaluating at 400°C after aging at either 700 or 800°C. Since surface area has not really begun to decrease at this point (especially at 700°C), it follows that any reduction in NO_x conversion would primarily be a result of PGM sintering. Furthermore, PGM sintering appears to correlate well with reductions in NO_x conversion at 200 and 300°C after aging at 900 and 1000°C. On the other hand, reductions in surface area correlate better with reductions in NO_x conversion at 400°C after aging at 900 and 1000°C. Table 4.8, a table of sum of square residual (R^2) values from linear least squares bivariate regression models created for each of the datasets plotted in the scatterplots, provides quantitative evidence to corroborate the conclusions just drawn from the scatterplots. Notice that the R^2 values for PGM size and 400°C evaluations after aging at 700 and 800°C are .99 and 0.98, respectively. Also, note the R^2 values of 0.83 and 1.00 for surface area and 400°C evaluations after aging at 900 and 1000°C.

Table 4.8 – Correlation between surface area loss and reduction in NO_x conversion after aging at the indicated temperatures

Material Effect	**Aging Temperature**	**Evaluation Temperature**		
		200°C	**300°C**	**400°C**
PGM Size	**700°C**	0.91	0.45	0.99
	800°C	0.94	0.32	0.98
	900°C	0.01	0.90	0.74
	1000°C	0.96	0.92	0.84
Surface Area	**700°C**	0.06	0.90	0.15
	800°C	0.78	0.29	0.01
	900°C	0.03	0.79	0.83
	1000°C	0.80	0.63	1.00

Chapter 5

CONCLUSIONS

The effects of high-temperature, cyclic aging on the NO_x conversion and the surface morphology of the washcoat of a fully-formulated lean NO_x trap (LNT) are investigated in the present study. An understanding of the thermal deactivation mechanisms is central to designing LNTs capable of withstanding high-temperature, periodic desulfations. LNTs are aged in a bench-flow reactor (BFR) at nominal aging temperatures of 700, 800, 900, and 1000^oC using an aging cycle consisting of a 130s lean phase and a 50s rich phase. NO_x conversion of fresh and aged LNTs is evaluated at 200, 300, and 400^oC in the same BFR with simulated diesel exhaust gases using an evaluation cycle consisting of a 60s lean phase and a 5s rich phase.

The evaluation temperature has a large effect on the NO_x conversion of the LNTs used in this study. The maximum NO_x conversion occurs when evaluating at 300^oC, irrespective of whether the catalyst is fresh or aged. At all three evaluating temperatures the outlet concentration of NO_2 is much larger than that of NO indicating that NO_x conversion is limited by NO_x storage or release/reduction mechanisms and not by NO to NO_2 oxidation. At 200^oC the limiting mechanism is likely the combined release/reduction of NO_x because of high surface nitrate stability (ineffective release) and low NO_x reduction reaction rate, whereas at 400^oC the limiting mechanism is probably NO_x storage because of the instability of surface nitrates at this temperature. The effect of aging temperature and number of aging cycles on NO_x conversion depends on the

specific aging temperature. NO_x conversion is most affected at aging temperatures of 900 and 1000^oC, with minimal degradation in performance observed after aging at 700 and 800^oC. At aging temperatures of 900 and 1000^oC, the NO_x conversion decreases as the number of aging cycles increases until a steady value is reached.

The effects of aging temperature and number of aging cycles on the LNT's surface morphology are investigated with EPMA, XRD, TEM, and BET. Migration and agglomeration of Ba and Ce are investigated with EPMA line scans or elemental maps, and there is no evidence that either of these phenomena occurs as a result of thermal aging.

XRD and TEM are used to determine the growth in average PGM particle size as a function of aging temperature and number of aging cycles. Analyses of TEM micrographs of a fresh LNT sample indicate that Pt particles have an average diameter of 2.5 nm. After aging at 754 and 929^oC for 100 cycles, the average particle diameter grows to 6.5 and 10.5 nm, respectively. In general, particle growth is found to be a function of both aging temperature and number of aging cycles, with the largest average PGM particle diameter observed in this study of 26 nm occurring after aging at 1070^oC for 350 cycles. The effect of PGM particle growth on NO_x conversion is difficult to quantify, but linear regression models indicate strong correlations between PGM growth and reduction in NO_x conversion after when evaluating at 400^oC after aging at either 700 or 800^oC, and when evaluating at 200 or 300^oC after aging at 900 or 1000^oC.

The physicochemical changes of the Ba phase are elucidated with XRD and EPMA. The $BaCO_3$ peaks disappear from XRD patterns after aging at approximately 900^oC for 10 cycles, and, there is no growth of the expected $BaAl_2O_4$ peaks or peaks of

other Ba phases even after aging at 1070°C for 350 cycles. However, the disappearance of the Ba phase is not confirmed by EPMA line scans and elemental maps, in which the concentration of elemental Ba remains unchanged after aging. It is possible that Ba undergoes a process of vitrification leading to an amorphous Ba phase. If this is the case, the loss of crystalline $BaCO_3$ does not appear to affect NO_x storage performance, since the LNTs continue to store a substantial amount of NO_x at all evaluating temperatures even after the $BaCO_3$ has disappeared from XRD patterns. On the other hand, it is also possible that the storage and reduction of NO_x has migrated to the rear-half of the catalyst where $BaCO_3$ is still present after all aging experiments. However, the rich phase exotherms during evaluation experiments in the rear-half of the LNT do not increase in size with aging as would be expected if more NO_x conversion were occurring there.

BET surface area measurements reveal that surface area of γ-Al_2O_3 washcoat is a function of both aging temperature and number of aging cycles, with the most severe reductions in surface area occurring after aging at 900 and 1000°C and only minimal reductions after aging at 700 and 800°C. The surface area of LNTs (cordierite+washcoat) decreases from 36 m^2/g when fresh to 19 m^2/g after aging at 1070°C for 350 cycles. This reduction in surface area can be attributed to the washcoat because the surface area of the cordierite substrate of the LNTs used in this study is stable to much higher temperatures than 1070°C, the maximum aging temperature. Furthermore, large reductions in surface area when aging at 900 and 1000°C occur after only 10 aging cycles. Statistical analysis indicates that NO_x conversion and surface area are strongly correlated when evaluating at 400°C after aging at either 900 or 1000°C.

LIST OF REFERENCES

[1] Charles River Association. *Diesel Technology and the American Economy*, Report No. D02378-00. Washington, D.C.: October 2000.

[2] U.S. Department of Energy. *Progress Report for Advanced Combustion Engine Technology*, 2005.

[3] U.S. Environmental Protection Agency. *CO: How carbon monoxide affects the way we live and breathe*, Website: http://www.epa.gov/air/urbanair/co/index.html, November, 2000.

[4] Intergovernmental Panel on Climate Change (IPCC). *Fourth Assessment Report: Climate Change 2007,* 2007.

[5] U.S. Environmental Protection Agency. *NO_x: How nitrogen oxides affect the way we live and breathe*, Report No. EPA-465/F-98-005. September 1998.

[6 U.S. Environmental Protection Agency. *SO_x: How sulfur dioxide affects the way we live and breathe,* Website: http://www.epa.gov/air/urbanair/so2/index.html, November, 2000.

[7 U.S. Environmental Protection Agency. *Particle pollution and your health,* Report No. EPA-452/F-03-001. September, 2003.

[8] U.S. Environmental Protection Agency. *National Air Quality and Emissions Trends Report,* September 2003.

[9] W. S. Epling, L. E. Campbell, A. Yezerets, N. W. Currier and J. E. Parks, Catalysis Reviews 46 (2004) 163.

[10] J. Parks, J. Tassitano, J. Storey, 2nd Annual Advanced Stationary Reciprocating Engines Conference. *Lean NO_x Trap Catalysis: NO_x Reduction for Lean Natural Gas Applications*, March 15-16, 2005.

[11] N. W. Cant and M. J. Patterson, Catalysis Today 73 (2002) 271.

[12] I. Nova, L. Castoldi, L. Lietti, E. Tronconi, P. Forzatti, F. Prinetto, G. Ghiotti, Journal of Catalysis 222 (2004) 377.

[13] E. Fridell, H. Persson, B.Westerberg, L. Olsson, M. Skoglundh, Catalysis Letters, 66 (2000) 71.

[14] M. Twigg, Catalysis Today 117 (2006) 407.

[15] H. Ohtsuka, Applied Catalysis B 33 (2001) 325.

[16] L. Olsson, H. Persson, E. Fridell, M. Skoglundh and B. Andersson, J. Journal of Physical Chemistry B 105 (2001) 6895.

[17] L. Olsson, B. Westerberg, H. Persson, E. Fridell, M. Skoglundh and B. Andersson, Journal of Physical Chemistry B 103 (1999) 10433.

[18] V. Medhekar, V. Balakotaiah, M. Harold, Catalysis Today 114 (2006) 72.

[19] H. Mahzoul, J.F. Brilhac, P. Gilot, Applied Catalysis B 20 (1999) 47.

[20] F. Prinetto, G. Ghiotti, I. Nova, L. Lietti, E. Tronconi, P. Forzatti, Journal of Physical Chemistry B 105 (2001) 12732.

[21] P. Broqvist, H. Gronbeck, E. Fridell, I. Panas, Catalysis Today 96 (2004) 71.

[22] L. Castoldi, I. Nova, L. Lietti, P. Forzatti, Catalysis Today 96 (2004) 43.

[23] M. Piacentini, M. Maciejewski, A. Baiker, Applied Catalysis B 59 (2005) 187.

[24] M. Piacentini, M. Maciejewski, A. Baiker, Applied Catalysis B 66 (2006) 126.

[25] P. Forzatti, L. Castoldi, I. Nova, L. Lietti, E. Tronconi, Catalysis Today 117 (2006) 316.

[26] I. Nova, L. Castoldi, L. Lietti, E. Tronconi and P. Forzatti, Catalysis Today 75 (2002) 431.

[27] L. Lietti, P. Forzatti, I. Nova, E. Tronconi, Journal of Catalysis 204 (2001) 175.

[28] L. Xu, G. Graham, R. McCabe, Catalysis Letters 115 Nos. 3-4 108 (2007) 108.

[29] Z. Song, W. Liu, H. Nishiguchi, Catalysis Communications 8 (2007) 725.

[30] M. Ozawa, Journal of Alloys and Compounds 275-277 (1998) 886.

[31] B. Harrison, A. F. Diwell, C. Hallett, Platinum Metals Review 32 (1998) 73.

[32] Y. Ji, T. J. Toops, M. Crocker, Catalysis Letters 119 Nos. 3-4 (2007) 257.

[33] A. Amberntsson, H. Perrson, P. Engstrom, B. Kasemo, Applied Catalysis B 31 (2001) 27.

[34] W. Epling, G. Campbell, J. Parks, Catalysis Letters 90 Nos. 1-2 (2003) 45.

[35] S. Poulston, R. Rajaram, Catalysis Today 81 (2003) 603.

[36] D. James, E. Fourré, M. Ishii, M. Bowker, Applied Catalysis B 45 (2003) 147.

[37] I. Nova, L. Lietti, L. Castoldi, E. Tronconi, P. Forzatti, Journal of Catalysis 239 (2006) 244.

[38] M. Casapu, J. Grunwaldt, M. Maciejewski, A. Baiker, S. Eckhoff, U. Gobel, M. Wittrock, Journal of Catalysis 251 (2007) 28.

[39] Y. Chu, E. Ruckenstein, Journal of Catalysis 55 (1978) 281.

[40] K. Nguyen, H. Kim, B. Bunting, T. Toops, C. Yoon, SAE 2007 World Congress, 07-PFL-227 (2007).

[41] P. Flynn, S. Wanke, Journal of Catalysis 37 (1975) 432.

[42] G. Graham, H. Jen, W. Chun, H. Sun, X. Pan, R. McCabe, Catalysis Letters, 93, Nos. 3-4 (2004) 129.

[43] D. Kim, Y. Chin, G. Muntean, A. Yezeretz, N. Currier, W. Epling, H. Chen, H. Hess, C. Peden, Industrial and Engineering Chemistry 45 (2006) 8815.

[44] L. Olsson, E. Fridell, Journal of Catalysis 210 (2002) 340.

[45] Y. Nagai, T. Hirabayashi, K. Dohmae, N. Takagi, T. Minami, H. Shinjoh, S. Matsumoto, Journal of Catalysis 242 (2006) 103.

[47] H. Arai, M. Machida, Applied Catalysis A 138 (1996) 161.

[48] T. J. Toops, B. G. Bunting, K. Nguyen, A. Gopinath, Catalysis Today 123 (2007) 285.

[49] X. Wu, B. Yang, D. Weng, Journal of Alloys and Compounds 376 (2004) 241.

[50] M. Ozawa, Journal of Alloys and Compounds 408-412 (2006) 1090.

[51] D. Kim, Y. Chin, J. Kwak, J. Szanyi, C. Peden, Catalysis Letters 105 Nos. 3-4 (2005) 259.

[52] T. Szailer, J. Kwak, D. Kim, J. Szanyi, C. Wang, C. Peden, Catalysis Today 114 (2006) 86.

[53] D. Kim, J. Kwak, C. Peden, J. Szanyi, X. Wang, "Fundamental Studies of NO_x Adsorber Materials" CLEERS (2006) Presentation.

[54] B.-H. Jang, T.-H. Yeon, H.-S. Han, Y.-K. Park and J.-E. Yie, Catalysis Letters 77 (2001) 21.

[55] M. Casapu, J.D. Grunwaldt, M. Maciejewski, M. Wittrock, U. Go¨bel, A. Baiker, Applied Catalysis B 63 (2006) 232.

[56] S. Hodjati, P. Bernhardt, C. Petit, V. Pitchon, A. Kiennemann, Applied Catalysis B: Environmental 19 (1998) 209.

[57] S. Hodjati, P. Bernhardt, C. Petit, V. Pitchon, A. Kiennemann, Applied Catalysis B: Environmental 19 (1998) 221.

[58] http://www.cleers.org/

[59] S. Brunauer, P. H. Emmett and E. Teller, Journal of the American Chemical Society 60 (1938) 309.

[60] M. A. Vannice, *Kinetics of Catalytic Reactions,* Springer Science + Business Media, Inc. 2005.

VITA

Nathan Ottinger was born in Nashville, TN on January 27, 1984. He grew up in Lenoir City, TN where he attended Lenoir City High School and graduated in 2002, number nine in his class of approximately 200. During high school he worked on the family farm and quickly acquired an appreciation for a college degree. In the Fall of 2002, he enrolled in the University of Tennessee, Knoxville as a student in mechanical engineering. While at UTK he worked in Richmond, Va with Honeywell Inc. as a co-op engineer, at the Oak Ridge National Laboratory as a Science Undergraduate Laboratory Intern (SULI), at the Center for Musculoskeletal Research, at the math tutorial center, and with Dr. Nguyen on his current thesis. After his Junior year, he went to China and taught English for a year, an experience that opened his eyes to the world around him. His Senior year he did two senior design projects in which he designed an automatic box unloader for DENSO and a flexible mechanical tank seal for EASTMAN. In the fall of 2007, he began his Master's degree in mechanical engineering at the University of TN, Knoxville. He graduated in the Summer of 2008, and is currently planning a cross country bike touring trip before heading to Latin America and Southeast Asia for a while.